DESIGN AND ANALYSIS OF RF ENERGY HARVESTING COGNITIVE RELAY SYSTEMS

Ph.D. Thesis

by

ALOK KUMAR SHUKLA

DEPARTMENT OF ELECTRICAL ENGINEERING
INDIAN INSTITUTE OF TECHNOLOGY INDORE

JANUARY 2023

DESIGN AND ANALYSIS OF RF ENERGY HARVESTING COGNITIVE RELAY SYSTEMS

A THESIS

Submitted in partial fulfillment of the

requirements for the award of the degree

of

DOCTOR OF PHILOSOPHY

by

ALOK KUMAR SHUKLA

DEPARTMENT OF ELECTRICAL ENGINEERING

INDIAN INSTITUTE OF TECHNOLOGY INDORE

JANUARY 2023

INDIAN INSTITUTE OF TECHNOLOGY INDORE

CANDIDATE'S DECLARATION

I hereby certify that the work which is being presented in the thesis entitled "**DESIGN AND ANALYSIS OF RF ENERGY HARVESTING COGNITIVE RELAY SYSTEMS**" in the partial fulfillment of the requirements for the award of the degree of **DOCTOR OF PHILOSOPHY** and submitted in the **DEPARTMENT OF ELECTRICAL ENGINEERING**, **Indian Institute of Technology Indore**, is an authentic record of my own work carried out during the time period from June 2019 to January 2023 under the supervision of Prof. Prabhat Kumar Upadhyay, Professor, Department of Electrical Engineering, Indian Institute of Technology Indore, India.

The matter presented in this thesis has not been submitted by me for the award of any other degree of this or any other institute.

Shukla
11-01-23

Signature of the student with date
(ALOK KUMAR SHUKLA)

This is to certify that the above statement made by the candidate is correct to the best of my/our knowledge.

11-01-2023

Signature of Thesis Supervisor with date
(Prof. PRABHAT KUMAR UPADHYAY)

ALOK KUMAR SHUKLA has successfully given his Ph.D. Oral Examination held on March 28, 2023.

28-03-2023

Signature of Thesis Supervisor with date
(Prof. PRABHAT KUMAR UPADHYAY)

ACKNOWLEDGEMENTS

I take this opportunity to acknowledge my heartfelt gratitude to all those who have directly or indirectly helped me throughout my PhD. First and foremost, I thank Lord Hanuman Ji for giving me the strength, knowledge, and enlightenment to undertake this research work. Then, I would like to express my deep sense of respect and gratitude to my supervisor and mentor, Prof. Prabhat Kumar Upadhyay, for his invaluable guidance, sustained inspiration, and kind support towards my thesis work. He has given me all the freedom to pursue my research, and provided helpful career advice and suggestions, extending beyond academic boundaries, whenever needed. He has always been my source of inspiration during my stay at IIT Indore and will be, all my life.

Next, I would like to sincerely thank my comprehensive evaluation of research progress committee members Prof. I. A. Palani and Dr. Swaminathan R. for their interesting discussions and suggestions towards my research. I am thankful to all the faculty members and the staff at IIT Indore for their cooperation throughout my thesis work.

My appreciation also goes to all the members of the Wireless Communications (WiCom) Research Group for creating a friendly and conducive environment. It was my privilege to share the lab with Chandan Kumar Singh, Kajal Yadav, Ratnesh Kumar, Shivaji Cheepurupalli. I am immensely grateful to my seniors Dr Vinay Bankey and Dr Vibhum Singh for providing their help and valuable suggestions both technically and non-technically during my work. My appreciation also goes to Abhishek Ojha, Mayank Singh, Vivek Singh, and Narendra Dhakad for making a wonderful company and for sharing all the casual and valued moments during this study. Special thanks go to my great friends Anshu, Chandra Bhushan, Mansi, and Smriti for all the cheerful talks and encouragement.

I gratefully acknowledge the funding agency, Department of Science and Technology (DST), Government of India, for sponsoring my PhD work under the BRICS project DST/IMRCD/BRICS/PilotCall2/LargeWIN/2018(G). I will also thank the finance, administration, academic, and R&D sections of IIT Indore for all the necessary support.

Above all, I am indebted to my parents, Smt. Sandhya Devi and Shree Hari Narayan Shukla, for always encouraging and supporting me. Also I express my thanks to my sisters, Mansha, Aparna and Sharda, for their unbounded love, endless support, and faith in me, without which I would have not been able to achieve the greatest milestone of my life.

Lastly, I want to thank everyone who were part of this journey and has, in one way or another, helped me to successfully complete this research work.

Alok Kumar Shukla

Dedicated to
my family

ABSTRACT

The explosion of Internet of Things (IoT) applications and their integration in various aspects of everyday life necessitates the deployment of modern wireless network that can handle such exponentially rising data traffic. Massive device connectivity, higher energy- and spectrum- efficiency, low signal latency, long battery lifetime etc., are the most important requirements to be considered for deploying the next-generation communication networks. In this regard, cognitive radio (CR) and non-orthogonal multiple access (NOMA) have emerged as promising technologies for wireless networks owing to their capability of providing massive connectivity with higher spectrum efficiency (SE). By utilizing CR technology, secondary and primary users can coexist in the same spectrum bands by effectively discarding interference and collision, and thereby improve the SE measures. Out of the many contenders of fifth-generation (5G) communications, NOMA is considered as a promising technology that improves SE by manifolds. This makes NOMA a prominent candidate for IoT sensor networks. The basic idea of NOMA is to employ superposition coding to multiplex the multiple users' signals at the transmitter, and then to perform successive interference cancellation (SIC) at the receiver side to decode the signals in the power domain. The incorporation of NOMA into CR, referred to as cognitive NOMA (CNOMA), has demonstrated the capability to achieve higher SE while simultaneously reducing the complexity of the power allocation (PA) design. It can potentially fulfil the peculiarity of a 5G wireless network that provides a high throughput, broad connectivity, and low latency.

Besides SE improvement of wireless network, energy efficiency (EE) is another key parameter that should be considered while designing a futuristic 5G wireless network to enhance the lifespan. Recent studies indicate that the power requirement of IoT sensors and devices could be met by harvesting energy from radio frequency (RF) signals. In fact, RF signals carry both energy and information. The IoT sensors or nodes can recharge themselves by energy harvested from RF signals while simultaneously decoding the information data and relaying or transmitting the source node's information to its destination. Among the potential energy harvesting (EH) techniques, simultaneous wireless information and power transfer (SWIPT) has been contemplated as an energy efficient viable solution to self-sustainable communication in future wireless networks.

In this thesis, firstly, we investigate a spectral and energy-efficient wireless body area network (WBAN) for smart healthcare applications. Herein, we primarily focus on improving the spectrum utilization by intelligently sharing spectrum resources through CR technology, allowing various sensor nodes in the underlying network to co-exist without compromising on their quality-of-service (QoS). We prioritize the sensor nodes based on their applications (medical/non-medical) and thereby categorize them into primary and secondary users to implement an on-body CR-WBAN. Furthermore, two EH protocols namely time-switching cooperation (TSC) and power-splitting cooperation (PSC) are employed to facilitate the secondary node cooperation with the primary network in return for spectrum access. For both the primary and secondary networks, we derive useful expressions for the outage probability (OP). Consequently, it can be inferred that the PSC protocol notably outperforms the TSC protocol and thereby explores more spectrum sharing opportunities in the proposed CR-WBAN. Moreover, the impact of key parameters are highlighted to provide useful insights into the practical design of spectral and energy-efficient WBANs for smart healthcare applications.

Then, we analyze the performance of an EH-assisted overlay cognitive NOMA system. The underlying system consists of a primary transmitter-receiver pair accompanied by an energy-constrained secondary transmitter (ST) with its intended receiver. Accordingly, ST employs a time switching (TS) based receiver architecture to harvest energy from RF signals of the primary transmissions, and thereby uses this energy to relay the primary information and to transmit its own information simultaneously using the NOMA principle. For this, we propose two cooperative spectrum sharing (CSS) schemes based on incremental relaying (IR) protocol using amplify-and-forward (AF) and decode-and-forward (DF) strategies, viz., CSS-IAF and CSS-IDF, and compare their performance with the competitive fixed relaying based schemes. The proposed IR-based schemes adeptly avail the degrees-of-freedom to boost the system performance. Thereby, considering the realistic assumption of the NOMA-based imperfect successive interference cancellation, we derive the expressions of OP for the primary and secondary networks under both CSS-IAF and CSS-IDF schemes subject to the Nakagami-m fading. In addition, we quantify the throughput and energy efficiency for the considered system. The obtained theoretical findings are finally validated through numerous analytical and simulation results to reveal the advantages of the proposed CSS schemes over the baseline direct link transmission and orthogonal multiple access schemes.

Further, we investigate a SWIPT enabled IoT-based cognitive NOMA with coordinated direct and relay transmission (CDRT) system. It incorporates overlay CR and TS-based SWIPT technology to enhance spectrum utilization and energy efficiency. The proposed system comprises of a primary network having a primary transmitter and its intended NOMA receivers (*UE1*, *UE2*), accompanied by an energy-constrained secondary transmitter and its designated receiver ($IoT\text{-}U$). The primary transmitter communicates directly with its strong user *UE1* and exploits the secondary transmitter as an IoT-relay to communicate with a weak user *UE2*. The IoT-relay node employs TS-based receiver architecture and decode-and-forward protocol to convey the weak user's information along with its own information by following the NOMA principle. We evaluate the performance of the proposed system by considering both the perfect and imperfect successive interference cancellation at the legitimate users over Nakagami-m fading in terms of OP, system throughput, and energy efficiency. Moreover, we propose an iterative algorithm to minimize the OP by optimizing the TS factor. Further, the impact of key parameters is also highlighted, which lays the guidelines for the practical design of energy-efficient and spectrum-efficient futuristic wireless communication networks.

Lastly, we explore the deep learning framework for performance evaluation of an EH-assisted CDRT-NOMA system assuming perfect and imperfect successive interference cancellation. Specifically, we derive analytical expressions of the OP which include an infinite series, system throughput, and energy efficiency. Moreover, an asymptotic analysis of the OP in the high signal-to-noise ratio is carried out. Closed-form expressions of the exact OP and the ergodic sum capacity (ESC) are intractable owing to the complexity of the proposed scheme. To tackle this problem, we propose a deep learning framework to predict both the OP and ESC performances. The predicted results through the deep learning framework are shown to be consistent with the numerical results.

Above all, this thesis addresses various technical aspects for realization of RF EH cognitive relay systems and eventually provides useful insights into the practical system design. All the theoretical developments, proposed schemes, and strategies hereunder are primarily aimed at improving the EE, SE, and reliability for their possible applications in the future wireless networks.

CONTENTS

LIST OF FIGURES viii

LIST OF SYMBOLS x

LIST OF ABBREVIATIONS xii

1 Introduction 1
- 1.1 Cognitive Radio . . . 2
- 1.2 Cooperative Relaying . . . 4
  - 1.2.1 Fixed Relaying . . . 4
  - 1.2.2 Incremental Relaying . . . 5
- 1.3 Non-Orthogonal Multiple Access . . . 5
- 1.4 RF Energy Harvesting . . . 6
  - 1.4.1 PS-Based SWIPT . . . 6
  - 1.4.2 TS-Based SWIPT . . . 7
- 1.5 Motivation and Objectives . . . 8
  - 1.5.1 Motivation . . . 8
  - 1.5.2 Objectives . . . 10
- 1.6 Thesis Outline and Contributions . . . 10

2 Cognitive Relaying in Wireless Body Area Networks 16
- 2.1 System and Protocol Description . . . 19
  - 2.1.1 TSC Protocol . . . 21
  - 2.1.2 PSC Protocol . . . 23
- 2.2 Performance Analysis . . . 25
  - 2.2.1 Outage Probability of Primary Network . . . 26
  - 2.2.2 Outage Probability of Secondary Network . . . 28
  - 2.2.3 Constrained Power Allocation Policy for Spectrum Sharing . . . 29
  - 2.2.4 Network Throughput . . . 30
  - 2.2.5 Energy Efficiency . . . 30
- 2.3 Numerical and Simulation Results . . . 31
- 2.4 Summary . . . 37

3 Overlay Cognitive NOMA Systems with Incremental Relaying 39
- 3.1 System Model and Protocol Description . . . 42
  - 3.1.1 System Model . . . 42

3.1.2 EH Phase . . . 43
3.1.3 IT Phase . . . 44
3.1.4 Proposed IR Protocol . . . 47
3.2 Outage Performance of Primary Network . . . 48
3.2.1 DLT Scheme . . . 49
3.2.2 CSS Scheme . . . 50
3.2.3 NOMA-Based Power Allocation Parameter . . . 55
3.3 Outage Performance of Secondary Network . . . 56
3.3.1 CSS-IAF Scheme . . . 56
3.3.2 CSS-IDF Scheme . . . 58
3.4 Overall EH-OCNOMA System Performance . . . 61
3.4.1 System Throughput . . . 61
3.4.2 Energy Efficiency . . . 61
3.5 Results and Discussion . . . 62
3.6 Summary . . . 68

4 IoT-based Coordinated and Direct Relay Transmission Network with NOMA 71
4.1 System Descriptions . . . 73
4.1.1 EH Phase . . . 74
4.1.2 IT Phase . . . 75
4.2 Performance Analysis . . . 77
4.2.1 Outage Probability of the Primary Network . . . 77
4.2.2 Outage Probability of Secondary Network . . . 81
4.2.3 System Throughput . . . 83
4.2.4 Energy Efficiency . . . 83
4.2.5 Optimal Solution for TS Parameter . . . 84
4.3 Numerical Results . . . 85
4.4 Summary . . . 89

5 Deep Learning Analysis of CDRT Systems with Cognitive NOMA 91
5.1 System Model . . . 92
5.1.1 First Phase Transmission . . . 93
5.1.2 Second Phase Transmission . . . 94
5.2 Performance Analysis . . . 96
5.2.1 OP Analysis . . . 96
5.2.2 System Throughput . . . 100
5.2.3 Energy Efficiency . . . 101
5.3 Deep Learning Architecture . . . 101
5.3.1 Dataset Generation . . . 101
5.3.2 Description of DNN Model . . . 101
5.3.3 DNN learning model . . . 102
5.3.4 Real-time Prediction . . . 103
5.4 Numerical Results . . . 105
5.5 Summary . . . 108

6 Conclusions and Future Works 110
6.1 Conclusions . . . 110
6.2 Future Works . . . 112

Appendix A Derivation of (2.29) 115

Appendix B Derivation of (2.33) **116**

Appendix C Derivations of (3.28) **117**

Appendix D Derivations of (3.51) **118**

Appendix E Derivations of (3.53) **120**

Appendix F Derivations of (3.59) **121**

Appendix G Derivations of (4.18) **122**

Appendix H Derivations of (4.24) **124**

Appendix I Derivations of (4.36) **126**

Appendix J Derivation of (5.20) **128**

Appendix K Derivation of (5.25) **129**

REFERENCES **131**

LIST OF PUBLICATIONS **145**

LIST OF FIGURES

1.1 Interweave, Underlay, and Overlay Modes of Spectrum Sharing. . . . 3
1.2 PS-Based SWIPT Architecture. 7
1.3 TS-Based SWIPT Architecture. 7

2.1 Proposed design of a CR-WBAN. 19
2.2 Analytical model of the proposed CR-WBAN. 19
2.3 Transmission block structure for the TSC protocol. 21
2.4 Transmission block structure for the PSC protocol. 23
2.5 OP versus α of primary network with TSC protocol. 32
2.6 OP versus SNR of primary network with TSC protocol. 33
2.7 OP versus SNR of secondary network with TSC protocol. 33
2.8 OP versus ρ of primary network with PSC protocol. 34
2.9 OP versus SNR of primary network with PSC protocol. 35
2.10 OP versus SNR of secondary network with PSC protocol. 35
2.11 System throughput for the CR-WBAN. 36
2.12 Energy efficiency for the CR-WBAN. 36

3.1 System model. 43
3.2 Transmission Block Structure for EH and IT phase. 44
3.3 Flow chart for the proposed IR protocol. 47
3.4 OP versus SNR plots for the primary network with different target rates (R_p) (a) AF (b) DF. 63
3.5 OP versus γ_p plots for the primary network. 64
3.6 OP versus SNR plots for the secondary network (a) AF (b) DF. . . . 65
3.7 Impact of ipSIC on the OP performance of secondary network (a) AF (b) DF. 66
3.8 Throughput versus SNR plots for the EH-OCNOMA system (a) AF (b) DF. 66
3.9 Energy efficiency versus SNR plots for the EH-OCNOMA system (a) AF (b) DF. 67
3.10 Throughput versus α plots for the EH-OCNOMA system. 67

4.1 Proposed system model. 74
4.2 Transmission block structure for EH and IT phases. 74
4.3 Variation of convergence error for different L values. 81
4.4 OP versus SNR plots for the primary network with varying m parameter (a) IT phase 1 (b) IT phase 2. 86

4.5 OP versus SNR plot for the IoT user. 87
4.6 System throughput. 87
4.7 Energy efficiency for the CNOMA-CDRT system. 88
4.8 OP versus α plot the CNOMA-CDRT system. 88

5.1 System model. 93
5.2 Illustrations of deep model training and prediction phases. 102
5.3 Illustrations of the DNN architecture. 102
5.4 OP of D_1, D_2 and R versus SNR. 105
5.5 EC/ESC versus SNR. 106
5.6 System throughput versus SNR. 107
5.7 Energy efficiency versus SNR. 107

List of Symbols

- Basic arithmetic and calculus notations have standard definitions.

Elementary & Special Functions

Notation	Definition
$\Gamma(\cdot)$	Gamma function
$\Upsilon(\cdot,\cdot)$	lower incomplete Gamma function
$\Gamma(\cdot,\cdot)$	upper incomplete Gamma function
$\mathcal{K}_{\upsilon}(\cdot)$	modified Bessel function of the second kind of order υ
$\mathrm{erf}(\cdot)$	standard error function
$\log_i(\cdot)$	logarithm to base i

Probability & Statistics

Let X be a random variable, and $\mathcal{A}$ be an arbitrary event.

Notation	Definition
$\mathbb{E}(\cdot)$	expectation
$f_X(\cdot)$	probability density function (PDF) of X
$F_X(\cdot)$	cumulative distribution function (CDF) of X
$\Pr[\mathcal{A}]$	probability of $\mathcal{A}$
$X \sim \mathcal{CN}(\mu, \sigma^2)$	X is complex Gaussian distributed with mean μ and variance σ^2

Miscellaneous

Notation	Definition
$\triangleq$	equality by definition
$n!$	factorial of n
$\mathcal{C}_r^n = \binom{n}{r} = \frac{n!}{r!(n-r)!}$	binomial coefficient

List of Abbreviations

5G	Fifth-Generation
AF	Amplify-and-Forward
AWGN	Additive White Gaussian Noise
CDF	Cumulative Distribution Function
CDRT	Coordinated Direct and Relay Transmission
CNOMA	Cognitive NOMA
CR	Cognitive Radio
CSI	Channel State Information
CSS	Cooperative Spectrum Sharing
D2D	Device-to-Device
DF	Decode-and-Forward
DL	Direct Line
DLT	Direct Line Transmission
ECG	Electrocardiography
EE	Energy Efficiency
EEG	Electroencephalography
EEG	Electroencephalography
EH	Energy Harvesting
EMG	Electromyography
EVM	Error Vector Magnitude
ESC	Ergodic Sum Capacity
FD	Full-Duplex
FR	Fixed Relaying
HD	Half-Duplex
HI	Hardware Impairment
i.i.d.	Independent and Identically Distributed
ipSIC	Imperfect SIC
IoT	Internet of Things
IR	Incremental Relaying
IS	Interference Signal
IT	Information Transmission
LoS	Line-of-Sight
MRC	Maximal-Ratio Combining

NOMA	Non-Orthogonal Multiple Access
OMA	Orthogonal Multiple Access
OP	Outage Probability
PA	Power Allocation
PAF	Power Allocation Factor
PDF	Probability Density Function
PR	Primary Receiver
PSC	Power Splitting Cooperation
pSIC	Perfect SIC
PT	Primary Transmitter
PU	Primary User
QoS	Quality-of-Service
RF	Radio Frequency
RMSE	Root Mean Square Error
SE	Spectrum Efficiency
SIC	Successive Interference Cancellation
SINR	Signal-to-Interference-Plus-Noise Ratio
SNR	Signal-to-Noise Ratio
SR	Secondary Receiver
ST	Secondary Transmitter
SU	Secondary User
TSC	Time Switching Cooperation
WBAN	Wireless Body Area Network

CHAPTER 1

INTRODUCTION

In the last decade, the number of connected devices through wireless networks has grown tremendously, thanks to technologies such as the Internet of Things (IoT), which have resulted in the enormous growth of data associated with IoT applications [1]. There is a projection that by 2025, 80 billion IoT devices will be connected to the internet, leading to 175 trillion gigabytes of data traffic worldwide [2]. IoT is a network of physical objects, like sensors, that are further embedded with electronics, software, and network connectivity to enable data collection and exchange between them. It allows entities to be controlled remotely across existing infrastructure, and it is an intelligent technology that reduces human effort while facilitating the access to physical devices. It has numerous applications, including health monitoring, monitoring homes and cities, automation, routing, transportation management, target tracking, and environmental protection [3]. All of these IoT applications are made feasible through the sensor nodes which continuously monitor the surrounding environment and entities, gather and communicate sensed data based on IoT application requirements. Therefore, it can be anticipated that IoT technologies such as Machine-to-Machine (M2M) and Device-to-Device (D2D) communication, along with intelligent data analytic, will drastically alter the landscape of numerous industries, as a result, the implementation of automation is entirely feasible without human intervention. The massive connectivity requirement of IoT devices is expected to be fulfilled by the fifth-generation (5G) and the futuristic wireless networks [4]. However, with the rapid growth of the IoT applications, this system energy consumption is further growing rapidly. Therefore, it is consequential to use energy efficiently or to harness the sustainable energy sources to prolong the lifespan of IoT devices.

Meeting the capacity and energy demands of the IoT devices and networks is a challenge that needs to be resolved [5]. Thus, among the various challenging requirements of 5G and next-generation networks, spectral and energy efficiency are the two key requirements. Therefore, energy and spectral efficient protocols to ameliorate the capacity and energy demands of the massive IoT networks need to be designed. In this regard, cognitive radio (CR) and non-orthogonal multiple access (NOMA) [6] are promising technologies that can tackle the spectrum scarcity problem and provide massive device connectivity with higher spectrum efficiency (SE). In addition, energy harvesting (EH) has emerged as a promising solution to improve energy efficiency (EE) and to extend lifespan of energy-constrained IoT networks. Owing to the instability of harvesting energy from natural sources such as solar and wind, an alternative method has been explored to enable wireless devices scavenge energy from radio frequency (RF) signals [7]. Capitalizing on the fact that RF signals carry both information and energy, a simultaneous wireless information and power transfer (SWIPT) technique [8] can be utilized to address the aforementioned concerns in wireless networks.

To realize the energy- and spectral-efficient system, we primarily focus on four key-enabling technologies which are briefly described as follows:

1.1 Cognitive Radio

CR is one of the key enabling technology that can tackle the spectrum scarcity problem and provide massive device connectivity with higher SE. In CR, unlicensed secondary user (SU) is allowed to use the spectrum licensed to the primary user (PU) provided that such spectrum sharing does not deteriorate the quality-of-service (QoS) of the primary network [9]. CR enables efficient and effective use of the available spectrum by performing four main functions: spectrum sensing, spectrum management, spectrum mobility, and spectrum sharing. These functions work together in a cognitive radio cycle, as follows:

- Spectrum Sensing: This is the first and most important function of a cognitive radio. It involves detecting unused portions of the spectrum to be used opportunistically.

- Spectrum Management: Once the spectrum holes are detected, the cognitive radio must have the ability to choose the channel that suits its communication requirements.

- Spectrum Mobility: Since cognitive radios are given lower priority than licensed users, they should be able to suspend their communication in case a licensed user comes back and seamlessly move onto another vacant channel.

- Spectrum Sharing: In a network, a scheduling algorithm is involved to ensure that all the cognitive radios get a fair chance to use the spectrum.

These functions are performed in a cycle, enabling CRs to determine which portions of the spectrum are available, select the best available channel, coordinate access to this channel with other users, and vacate the channel when a licensed user is detected. By efficiently utilizing the available spectrum, CR can improve the capacity and reliability of wireless communication systems. There are three main paradigms for spectrum sharing, namely, interweave, underlay, and overlay as shown in Fig1.1.

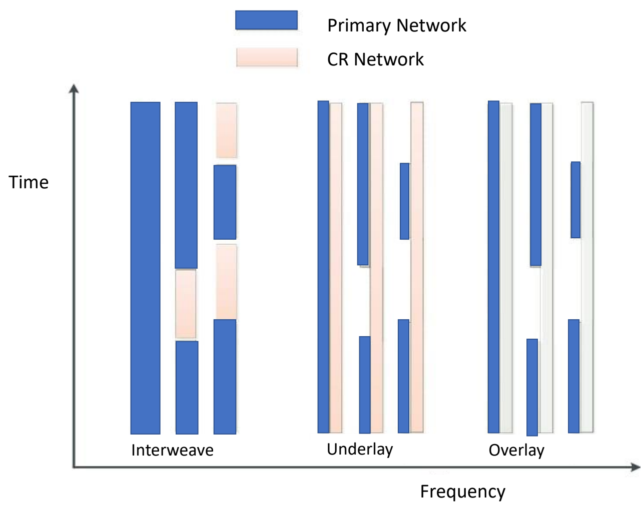

Figure 1.1: Interweave, Underlay, and Overlay Modes of Spectrum Sharing.

Interweave Approach: By utilizing interweave approach of CR, the SUs access the PUs' unoccupied spectrum (also referred to as white spaces) of PUs without interfering with the primary transmission. The major disadvantage of this approach is that the SUs are required to sense the spectrum hole before transmission, and therefore, is highly sensitive to the primary traffic behavior and spectrum sensing errors. This approach may not be suitable for dense networks due to the lack of availability of spectrum holes.

Underlay Approach: In the underlay approach, the SUs are allowed to utilize the licensed spectrum concurrently with the PUs, on condition that the interference caused by the SUs is below a predefined threshold to satisfy the QoS of the PUs [10]. In contrast to the interweave model, the underlay model has the advantage that the SUs can directly occupy licensed spectrum without considering the behavior of the PUs' traffic patterns. However, the SUs need to obtain the channel state information (CSI) of the pertaining links towards PUs for controlling their transmission power. Owing to the constrained power at SUs, in this paradigm, improving the performance of SUs is critical and challenging.

Overlay Approach: In the overlay paradigm, both the PUs and SUs share the same licensed spectrum for their signal transmission. In exchange, the SUs must provide relay cooperation to the PUs on a priority basis. Unlike the underlay model, the overlay paradigm does not impose strict transmit power restrictions on the SUs, allowing for concurrent PU and SU transmissions. However, there is a key difference between the overlay and underlay models in that SU devices must have knowledge of the PU's transmitted data sequence encoding methods (code book). This information can be utilized in two ways: first, it can be used to cancel PU interference on SU receivers using techniques such as dirty paper coding, which precodes transmitted data to negate interference effects; second, SU nodes can use this information to cooperate with the primary network by relaying PU messages.

1.2 Cooperative Relaying

Cooperative relaying is one of the key enabling technologies for mitigating the impact of multipath fading in wireless communication. It can be widely classified into two categories viz., fixed relaying (FR) and incremental relaying (IR).

1.2.1 Fixed Relaying

In this relaying, the distribution of the channel resources between source and relay is performed in a fixed manner. Although such protocols are easy to implement, they have the disadvantage of low bandwidth efficiency. FR includes commonly adopted amplify-and-forward (AF) and decode-and-forward (DF) protocols.

Amplify-and-Forward Relaying: In the AF relaying protocol, the relay simply amplifies the signal received from its source and transmits it further to the destination. Here, amplification is done essentially to combat the effect of the fading between the source and relay channel. This protocol has the main drawback of noise amplification by the relay. However, the reduced hardware complexity of AF relaying makes it more robust and less prone to errors, as it does not introduce decoding errors or information loss in the signal compared to its DF counterpart.

Decode-and-Forward Relaying: DF relaying is also known as regenerative relaying. In the DF relaying protocol, the relay decodes the signal received from its source, then re-encodes and transmits it to the destination. While doing this, there is a chance of an error propagation owing to the decoding and forwarding of the the incorrect signal by the relay, making the decoding process meaningless. To mitigate this risk, various techniques can be used in DF relaying, such as error-correcting codes, interleaving, and diversity schemes. Using error correction codes with IR is also one possible way to mitigate the errors.

1.2.2 Incremental Relaying

Incremental relaying mainly relies upon the limited feedback from the destination. In this, cooperative node adaptively performs the relaying operation based on the decoding of the signal through DL. Specifically, depending on the success/failure of the signal via direct transmission, the relaying cooperation is invoked. And, once the cooperation is triggered, its operation becomes similar to the FR. Hereby, firstly, the source node transmits its information to the destination as well as to the relay node. Then, if destination node is able to successfully decode the information signal from the source node, it sends an error-free one-bit feedback to the cooperative node indicating that the relaying cooperation is not needed. But if, it is not, then the feedback requests that the relay forwards the received signal from the source. IR is found to be more spectral-efficient compared to FR.

1.3 Non-Orthogonal Multiple Access

Out of the many contenders of 5G communications, NOMA has been envisioned as a promising technology to attain higher spectral efficiency and massive connectivity for the future wireless networks. One of the pivotal advantages of NOMA over traditional orthogonal multiple access (OMA) is the ability to transmit multiple users' signals simultaneously in the same resource block (i.e., time/frequency/code domain) by exploiting the power domain multiplexing at the transmitter [12]. Thereby, the successive interference cancellation (SIC) is employed at the receiver to separate the multiplexed signals [13]. In the mean time, the cooperative relaying technique has been introduced into the original NOMA scheme to obtain a spatial diversity gain for the far-away NOMA user with worse link quality, referred to as cooperative NOMA. Herein, the nearby NOMA user with better link quality detects the information of far-away NOMA user and further acts as a relay to forward that information during the cooperation phase. In such a way, the far-away user receives two copies of its desired signals, i.e., one from the base station (BS) and the other from the signal forwarded by the nearby user. By merging these two copies and grasping the advantages of spatial diversity gains, one can realize the improvement in reliability of the far-away NOMA user.

1.4 RF Energy Harvesting

The RF EH has emerged as a promising candidate to fulfil the energy requirements of the massive IoT sensor and devices of futuristic wireless networks [7]. Since RF signal carries both energy and information simultaneously, the wireless nodes can recharge themselves through RF EH and at the same time decode the information data and then relay or transmits the information of the source node to its destination [8]. Therefore, SWIPT is being considered as an energy-efficient viable approach for self-sustainable communication in wireless networks [14], [15]. Due to the practical considerations of the EH circuit of the receivers, SWIPT cannot be directly applied for the EH and information decoding at the same time. Therefore, power splitting (PS)- and time switching (TS)-based SWIPT are two popular EH architectures widely considered for receivers [16].

1.4.1 PS-Based SWIPT

In PS-based SWIPT, the block transmission time T is divided into two sub-blocks owing to the half-duplex operation, where one half is used for EH and information processing and the other half is used for information relaying. The receiver node splits the power between EH and information processing phases as shown in Fig. 1.2. In this scheme, a energy constrained node first harvests the energy from the signal of source node using τP_S where τ is the power splitting factor, and P_S is the transit power of the source node. The energy constrained node uses the remaining power $(1-\tau)P_S$ for the information decoding. The harvested energy at the node can be given by

$$E_h^{PS} = \Theta \tau P_s |h|^2 \frac{T}{2}, \tag{1.1}$$

where $\Theta(\ 0 < \Theta < 1)$ denotes the EH efficiency and it depends on the rectifier and EH circuitry deployed at the node, $|h|^2$ represents the channel gain between the EH node and the source node.

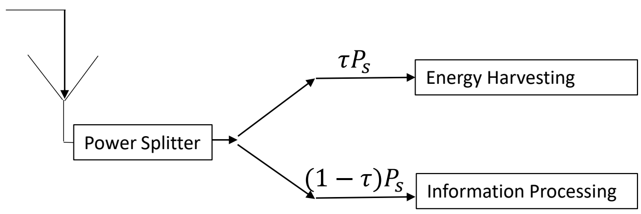

Figure 1.2: PS-Based SWIPT Architecture.

1.4.2 TS-Based SWIPT

In TS-based SWIPT, time is switched between EH and information processing phases as shown in Fig. 1.3. In this scheme, a energy constrained node first harvests the energy from the source node signal for a duration of αT, where α is the time switching factor, and T is total time duration. The energy constrained node uses the remaining time $(1-\alpha)T$ for the information decoding. The harvested energy at the node can be given by

$$E_h^{TS} = \Theta \alpha P_s |h|^2 T. \tag{1.2}$$

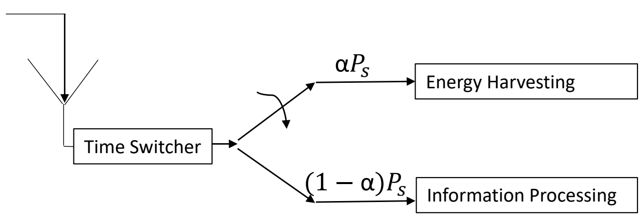

Figure 1.3: TS-Based SWIPT Architecture.

1.5 Motivation and Objectives

In this section, we present the motivation and objectives behind the research work in this thesis.

1.5.1 Motivation

With the rapid development in the area of RF EH, it is essential to investigate models that integrates the basic notion of SWIPT within several existing wireless communication systems. In the thesis work, we consider different types of wireless communications based system models, where the concerned devices are capable of handling SWIPT mechanism. In this regard, firstly we consider a wireless body area networks (WBAN), where the idea of RF-based EH can be explored for perpetual energy supply as the traditional charging process of sensors or battery replacement of sensors is not viable. There are several sensor nodes in WBANs which have equal rights to co-exist in the same spectrum band. However, this is unrealistic in situations where certain sensor nodes need more access to spectrum than other sensors in the network depending on their applications. Here, we intend on utilizing the concepts of CR technology [17] to prioritize sensors used for medical applications. Specifically, we propose a CR-WBAN configuration whereby we prioritize sensors as primary and secondary users based on their applications, e.g., medical or non-medical. On another front, future wireless networks have to meet the demands of energy, high data rate and a huge number of users effectively. In this respect, the conventional OMA with EH scheme can not accomplish such requirements owing to its limitation of serving one user at a time, and thus, the available spectrum and energy resource are still under-utilized. By incorporating SWIPT into cognitive NOMA (CNOMA), a more spectral and energy efficient wireless network is expected to be framed with a sustainable environment. There have been diverse research works done by considering SWIPT into CNOMA [18], [22]. Authors in [18] have investigated a cooperative multiple-input-single-output SWIPT NOMA protocol, where a strong NOMA user serves as an EH relay and assists a weak NOMA user by using the PS protocol. The outage performance of cooperative CNOMA networks with SWIPT using DF relaying has been investigated in [22], where cognitive relay harvests the transmission power from the secondary transmitter (ST) by exploiting the PS scheme using the fixed power allocation based NOMA protocol. The aforementioned works on SWIPT-enabled CNOMA networks follow the conventional FR strategy which impels the ST to incorporate the relaying operation even when the PR is able to decode its signal through the primary DL, which is not at all an efficient way of utilizing the spectrum. Moreover, they have assumed the ideal case of perfect SIC (pSIC) for the performance investigation. However, the pSIC is difficult to realize in practice, owing to the many implementation issues, such as complexity scaling and error propagation [24]. Consequently, these critical factors will lead to an error in decoding, causing residual interference signal (IS). Thereby, the effects of imperfect SIC (ipSIC) [25] may pose limitations on the capacity of the SWIPT-based CNOMA network. While few recent works have considered the impact of ipSIC [26], [27], [28] on the performance evaluation of CNOMA networks, they have not explored the potential features of SWIPT. Thus, we consider a overlay CNOMA network, where the existing literature overlooked the more spectrum-efficient scheme viz., IR with SWIPT-enable network.

Another strategy that can maximize SE of 5G wireless networks is utilizing NOMA in coordinated direct and relay transmission (CDRT). Authors in [29] have studied the NOMA with CDRT and demonstrated that the proposed scheme outperforms the NOMA without CDRT in terms of ergodic sum capacity (ESC). Based on [29], authors in [18] proposed a dynamic transmission scheme for NOMA-based CDRT system. However, it was apparent from the literature survey that employing EH with overlay CNOMA-CDRT network still stands unexplored. Inspired by these studies, we propose a SWIPT enabled IoT based overlay CNOMA-CDRT system considering both pSIC and ipSIC.

Due to the enormous complexity and variability of future wireless network service requirements, it is probable that standard model-based approaches, i.e., using closed-form expressions, are no longer sufficient for deployment, network resource management, and operation. In recent years, data-driven approaches for system performance evaluation have been developed, such as deep learning modeling, which make performance analysis efficient and accurate without having to make mathematical derivations. Thus, we pursue a deep learning approach along with model-based approach for the evaluation of performance analysis of EH-based CDRT system with CNOMA.

1.5.2 Objectives

The aforementioned research voids have motivated us to achieve the following objectives towards the design of future wireless networks:

- To assess the performance of cognitive relaying in WBAN with EH.
- To investigate the performance of overlay CNOMA with IR protocol.
- To analyze the performance of SWIPT enabled CNOMA-CDRT system.
- To explore the deep learning approach in performance evaluation of CNOMA-CDRT system with EH capability.

With the above-stated objectives, this thesis presents a comprehensive performance analysis of RF energy harvesting cognitive relay systems over generalized fading channels. We address the various technical aspects through exhaustive mathematical analysis and highlight important guidelines towards the design of futuristic wireless networks.

1.6 Thesis Outline and Contributions

In this thesis, we comprehensively analyze the performance of RF energy harvesting cognitive relay systems under the appropriately modelled fading channels. In general, the log-normal fading model observes the statistical characterizations of the WBAN communication which is best suited to model small-scale fading [30]. Whereas, Nakagami-m fading is a generalized model, which captures a variety of fading scenarios of terrestrial wireless channels and incorporates the well-known Rayleigh fading as a unique case. The current chapter introduces the reader to the background of the work, outlines the research objectives and their motivation, and discusses various technologies involved in this thesis work. The main contributions from the other chapters are summarized as follows:

- In Chapter 2[1], we investigate a spectral and energy-efficient WBAN for smart

[1]The contributions of this chapter are presented in the following papers:

1. A. K. Shukla, P. K. Upadhyay, A. Srivastava, and J. M. Moualeu, "Enabling co-existence of cognitive sensor nodes with energy harvesting in body area networks," *IEEE Sensors J.*, vol. 21, no. 9, pp. 11213-11223, May 2021.
2. A. K. Shukla, P. K. Upadhyay, A. Srivastava, and J. M. Moualeu, "Energy harvesting-assisted cognitive sensor nodes in wireless body area networks," in *2021 IEEE 7th World Forum on Internet of Things (WF-IoT)*, 2021, New Orleans, LA, USA, pp. 488-493.

healthcare applications. Herein, we primarily focus on improving the spectrum utilization by intelligently sharing spectrum resources through CR technology, allowing various sensor nodes in the underlying network to co-exist without compromising on their QoS. We prioritize the sensor nodes based on their applications (medical/non-medical) and thereby categorize them into primary and secondary users to implement an on-body CR- WBAN. Furthermore, two EH protocols namely time-switching cooperation (TSC) and power-splitting cooperation (PSC) are employed to facilitate the secondary node cooperation with the primary network in return for spectrum access. For both the primary and secondary networks, we derive useful expressions for the outage probability (OP). To provide more insights into the proposed CR-WBAN, the throughput and energy efficiency performances assuming a delay-limited scenario are investigated. The impact of key parameters are demonstrated to provide guidelines for the practical design of spectral and energy-efficient WBANs. The accuracy of our proposed analytical framework is verified through Monte Carlo simulations.

- In Chapter 3[2], we analyze the performance of an EH-assisted overlay cognitive NOMA system. The underlying system consists of a primary transmitter-receiver pair accompanied by an energy-constrained ST with its intended receiver. Accordingly, ST employs a TS based receiver architecture to harvest energy from radio-frequency signals of the primary transmissions, and thereby uses this energy to relay the primary information and to transmit its own information simultaneously using the NOMA principle. For this, we propose two cooperative spectrum sharing (CSS) schemes based on IR protocol using AF and DF strategies, viz., CSS-IAF and CSS-IDF, and compare their performance with the competitive fixed relaying based schemes. The proposed IR-based schemes adeptly avail the degrees-of-freedom to boost the system performance. Thereby, considering the realistic assumption of the NOMA-based ipSIC, we derive the expressions of OP for the primary and secondary networks under both CSS-IAF and CSS-IDF schemes subject to the Nakagami-

[2]The contributions of this chapter are presented in the following paper:

1. A. K. Shukla, V. Singh, P. K. Upadhyay, Abhinav Kumar, and J. M. Moualeu, "Performance analysis of energy harvesting-assisted overlay cognitive NOMA systems with incremental relaying," *IEEE Open J. Commun. Society*, vol. 2, pp. 1558-1576, 2021.

m fading. In addition, we quantify the throughput and energy efficiency for the considered system. The obtained theoretical findings are finally validated through numerous analytical and simulation results to reveal the advantages of the proposed CSS schemes over the baseline DL transmission (DLT) and orthogonal multiple access schemes.

- In Chapter 4[3], we propose a SWIPT enabled IoT-based CNOMA-CDRT system. It incorporates overlay CR and TS-based SWIPT technology to enhance spectrum utilization and energy efficiency. The proposed system comprises of a primary network having a primary transmitter (PT) and its intended NOMA receivers (*UE1*, *UE2*), accompanied by an energy-constrained secondary transmitter and its designated receiver (IoT-U). The PT communicates directly with its strong user *UE1* and exploits the secondary transmitter as an IoT-relay to communicate with a weak user *UE2*. The IoT-relay node employs TS-based receiver architecture and decode-and-forward protocol to convey the weak user's information along with its own information by following the NOMA principle. We evaluate the performance of the proposed system by considering both the perfect and imperfect successive interference cancellation at the legitimate users over Nakagami-m fading in terms of OP, system throughput, and energy efficiency. Moreover, we propose an iterative algorithm to minimize the OP by optimizing the TS factor. Further, the impact of key parameters is also highlighted, which lays the guidelines for the practical design of energy-efficient and spectrum-efficient futuristic wireless communication networks.

- In Chapter 5[4], we investigate an EH-assisted CDRT in an overlay CNOMA system assuming perfect and imperfect successive interference cancellation. Specifically, we derive analytical expressions of the OP which include an in-

[3]The contributions of this chapter are presented in the following paper:

1. A. K. Shukla, J. Sharanya, K. Yadav and P. K. Upadhyay, "Exploiting SWIPT enabled IoT-based cognitive non-orthogonal multiple access with coordinated direct and relay transmission," *IEEE Sensors J.*, vol. 22, no. 19, pp. 18988-18999, Oct. 2022.

[4]The contributions of this chapter are presented in the following paper:

1. A. K. Shukla, K. Yadav, P. K. Upadhyay, and J. M. Moualeu "Exploiting deep learning in the performance evaluation of EH-based coordinated direct and relay transmission system with cognitive NOMA," *IEEE Commun. Lett.*, Mar. 2023, doi:10.1109/LCOMM.2023.325866.

finite series, system throughput, and energy efficiency. Moreover, an asymptotic analysis of the OP in the high signal-to-noise ratio (SNR) is carried out. Closed-form expressions of the exact OP and the ESC are intractable owing to the complexity of the proposed scheme. To tackle this problem, we propose a deep learning framework to predict both the OP and ESC performances. The predicted results through the deep learning framework are shown to be consistent with the numerical results.

Finally, in Chapter 6, we draw the conclusions from the work in this thesis and provide the possible future directions. Besides, the proofs of useful theorems/lemmas are relegated into the appendices.

CHAPTER 2

COGNITIVE RELAYING IN WIRELESS BODY AREA NETWORKS

The rapid evolution of wireless technologies in recent years has led to the development of smart projects such as IoT-based smart healthcare systems [31]. To this end, WBANs have attracted a great deal of attention in the research community as a potential solution in the implementation of such projects [32]. A WBAN consists of low-power sensor nodes (placed on, around, or implanted in the human body) that constantly monitor the physiological signals and health status of the human body without affecting its normal routine activities [33]. These physiological signals include and are not limited to Electrocardiography (ECG) signals, Electroencephalography (EEG) signals, Electromyography (EMG) signals, blood pressure, and body temperature. The physiological data collected by sensor nodes is delivered to a nearby central unit/gateway node (e.g., a smartphone) and then forwarded over the Internet to a remote medical server or an off-site medical expert for effective diagnoses. In addition to medical applications, WBAN has several non-medical applications viz., interactive gaming, sports training, data file transfer and social networking applications [34]. The WBANs are limited by the degradation of the link reliability and network performance due to low-power requirements and high attenuation levels [35]. Some recent research studies [36–38] have integrated cooperative communication into WBANs in an effort to address the above limitations, by exploiting spatial diversity. These studies reveal that relay-based cooperative networks improve the energy efficiency of WBANs. However, the energy-constrained nature of sensor nodes in WBANs often requires periodical replacement of the batteries which may not be practical in certain situations such as in-body implantable devices. Various energy scavenging interface circuits for WBANs with different efficiencies are discussed in [39].

In general, several sensor nodes in WBANs have equal rights to co-exist in the same spectrum band. However, this is unrealistic in situations where certain sensor nodes need more access to spectrum than other sensors in the network depending on their applications. While the concept of channel hopping has good potential for interference-avoiding communications in wireless sensor networks, it suffers from convergence and time–frequency slot utilization problems. For this, a decentralized time-synchronized channel swapping protocol is proposed to achieve higher bandwidth utilization and connectivity [40]. In [41], the authors addressed the self-coexistence problem in CR-based IEEE 802.22 wireless regional area networks (WRANs). Here, we intend on utilizing the concepts of CR technology [17] to prioritize sensors used for medical applications. Specifically, we propose a CR-WBAN configuration whereby we prioritize sensors as primary and secondary users based on their applications, e.g., medical or non-medical. Sensors dedicated to medical applications are treated as the PUs. Therefore, we aim to ensure their QoS by enabling cooperation of the secondary sensor nodes (sensors used for non-medical purposes such as interactive gaming). This, in turn, also improves spectrum utilization efficiency as a large number of sensors can be accommodated over the same spectrum band. Furthermore, the idea of RF-based EH can be explored for perpetual energy supply as the traditional charging process of sensors or battery replacement of sensors is not viable.

The proposed design to implement a CR-WBAN is demonstrated in Fig. 2.1. Herein, we categorize the users based on the priority of the applications. Since the sensors used for medical diagnosis (e.g., EEG, ECG, EMG sensors) are crucial, they are called PUs. The other sensors (motion sensors), used for non-medical applications, are called SUs. To avoid interference among co-located nodes, spectrum sensing algorithms for CR-based WBANs were investigated in [42]-[47]. However, the implementation of spectrum sensing paradigms in CR-based WBANs can be challenging in real scenarios: (a) delays due to spectrum detection; (b) a spectrum sensing mechanism is power-intensive and could be impractical for low-power nodes in WBANs. To circumvent this issue, we exploit an overlay paradigm of CR technology to allow SU cooperation and limit the interference at the PUs. In addition, the SU is provided with EH capability, thereby, it can be enabled to harvest energy from the primary transmissions and can utilize this energy for its own communication in conjunction with cooperation with the PU on a priority basis. We present two protocols for EH-based cooperative spectrum sharing, namely TSC and PSC protocols. To the best of the authors' knowledge, there is no reported work in literature that has considered an overlay CR technique in EH-based WBAN, and this chapter aims to partly bridge this gap. The main contributions of this chapter are highlighted in the following points:

- We propose to implement an EH-based overlay CR-WBAN by employing two spectrum sharing cooperation (i.e., TSC and PSC) protocols to facilitate both primary (medical sensors) and secondary (non-medical sensors) communications simultaneously.

- Specifically, for the primary network, we derive the OP expressions with and without spectrum sharing in the presence of DL communication. We then derive the OP expression for the secondary network.

- Further, to provide more insights into the proposed CR-WBAN, we investigate the throughput and energy efficiency performances under both TSC and PSC protocols assuming a delay-limited scenario.

- Our results demonstrate the impact of spectrum sharing factor, TSC and PSC parameters on the overall performance of the proposed EH-based CR-WBAN. This provides useful guidelines for the design of practical WBANs to achieve high spectral and energy efficiency.

In Section 2.1, the analytical model of the proposed CR-WBAN is framed while deriving the end-to-end SNRs under TSC and PSC protocols. In Section 2.2, the performance of the EH-based CR-WBAN is analyzed in terms of OP, throughput, and energy efficiency under both protocols. We also investigate the power allocation policy for an effective spectrum sharing. Numerical and simulation results are presented in Section 2.3, and lastly, summary of the chapter are drawn in Section 2.4.

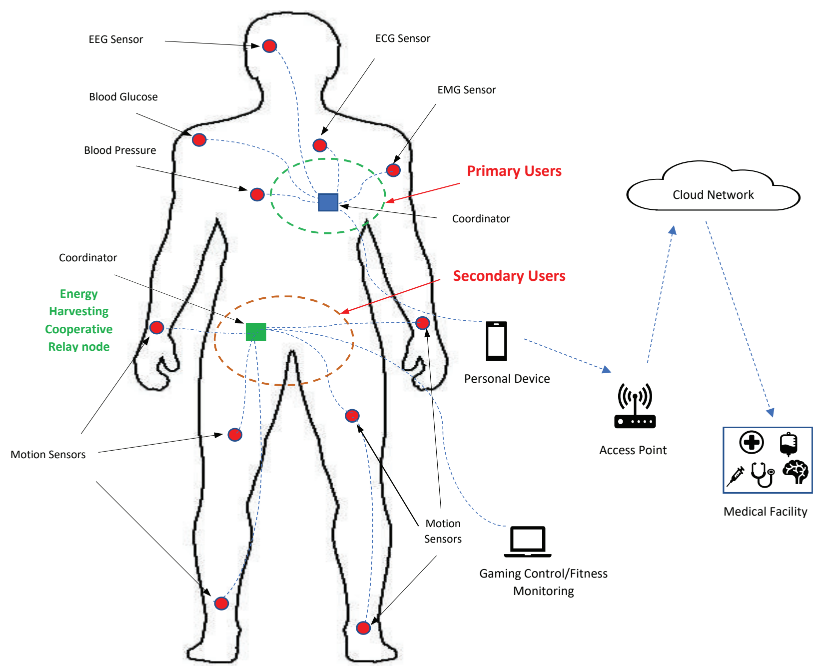

Figure 2.1: Proposed design of a CR-WBAN.

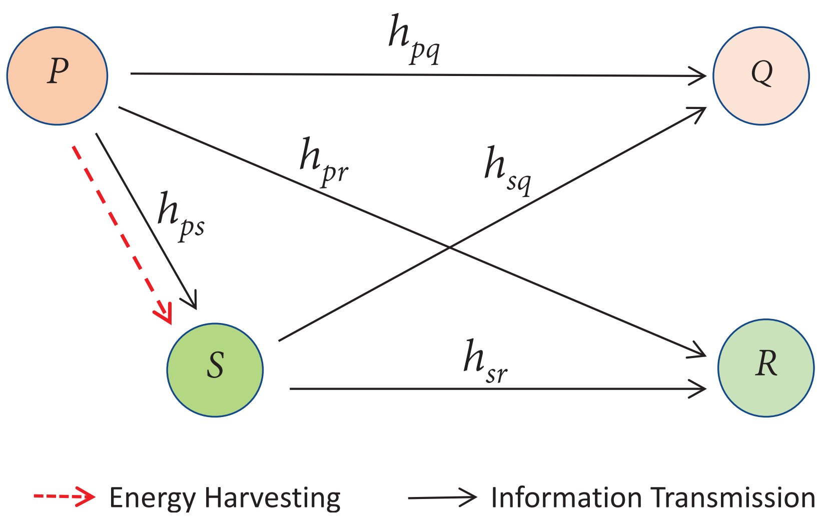

Figure 2.2: Analytical model of the proposed CR-WBAN.

2.1 System and Protocol Description

Fig. 2.2 illustrates an analytical model for the proposed EH-based CR-WBAN in which a primary sensor network coexists with a secondary sensor network[1]. On one hand, the primary network includes a transmitter node P and a receiver node Q, and on the other hand, the secondary network consists of an energy-constrained transmitter node S and the corresponding receiver node R. Hereby, node P intends to establish a direct communication with node Q as well as through the relay cooperation of the secondary node S. However, it is assumed that S is an energy-constrained

[1]The different transmission phases corresponding to the proposed model as shown in Fig. 2.2 are discussed in the subsequent subsections for the sake of clarity.

node and thus, it has to first harvest energy from primary transmissions and then use this energy to relay the primary signal as well as transmit its own signal. In addition, the following assumptions and notations are adopted in the transmission protocol.

- The underlying WBAN is fixed/static (a resting body for example) as in [48] and is located far away from other nodes/wireless devices so as to avoid the impact of any interference caused by the former. Such a scenario can be found in practice. One similar assumption is made in [49], wherein the authors present a novel ultra wideband (UWB) channel model for body-centric wireless communications in an indoor anechoic chamber environment (to avoid interference).

- All sensor nodes are equipped with a single antenna due to their limited size and operate in half-duplex mode (which implies that they cannot transmit and receive simultaneously).

- The secondary node S has an RF-based EH capability and acts as an AF relay for primary communications while accessing the primary spectrum for its own communication.

- Thermal noise at each receiver is modeled as additive white Gaussian noise (AWGN) with zero mean and variance N_o.

- All links are subject to log-normal fading and the channel gain from node i to node j is represented by h_{ij}, where $i \in \{p, s\}$ and $j \in \{q, s, r\}$ with $i \neq j$. Note that a log-normal distribution is best suited to model small-scale fading in WBAN communications [30].

- The transmission block time is denoted as T.

- The primary node P has a fixed power supply of P_p, whereas P_s represents the transmit powers at node S.

In this paper, we assume that source node S and destination node D have fixed power supply, while relay nodes are RF-based energy harvesting nodes, each relay is equipped with an energy-harvesting circuit that can convert the received RF power to direct current (DC). With RF-based EH capability, the secondary node S can be

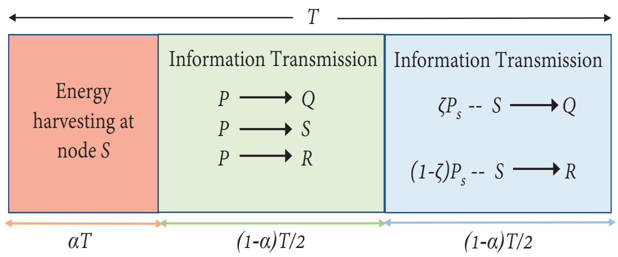

Figure 2.3: Transmission block structure for the TSC protocol.

enabled to share the spectrum with the PUs in exchange for cooperation with the primary transmission on a priority basis. For this, we study two EH-based spectrum sharing cooperation protocols (viz., TSC and PSC protocols) for the proposed CR-WBAN as described in the following subsections.

2.1.1 TSC Protocol

In the TSC protocol, the transmission block time is divided into three sub-blocks as depicted in Fig. 2.3. With $\alpha \in (0, 1)$ defined as the TSC parameter, a duration of αT is used by S to harvest energy from the primary signal and the remaining time $(1-\alpha)T$ is utilized for transmitting information. Since the nodes operate in half-duplex fashion, $(1-\alpha)T/2$ time is used for receiving information at nodes S, Q, and R from node P, while the other $(1-\alpha)T/2$ time is used for transmitting network-coded message from S to nodes Q and R. Thus, during the harvesting time αT, the harvested energy at S is given by

$$E_s = \Theta P_p |h_{ps}|^2 \alpha T, \tag{2.1}$$

where Θ is the energy conversion efficiency that varies from 0 to 1 relying on the rectification process and the EH circuitry [50]. Hence, the transmit power of node S over the time $(1-\alpha)T/2$ can be obtained as

$$P_s = \frac{E_s}{(1-\alpha)T/2} = \frac{2\alpha\Theta P_p |h_{ps}|^2}{1-\alpha}. \tag{2.2}$$

In the second sub-block transmission phase, P transmits an information signal x_p (having unit energy) to Q, which is also received by the secondary nodes S and R. Therefore, the received signals y_{pq}, y_{ps}, and y_{pr} at nodes Q, S, and R can be expressed, respectively, by

$$y_{pj} = \sqrt{P_p} h_{pj} x_p + n_{pj}, \tag{2.3}$$

where $j \in \{q, s, r\}$ and n_{pj} is the AWGN variable[2].

Now, during the third sub-block transmission phase, node S facilitates an AF relaying cooperation to the primary data communication, and in addition, communicates concurrently with its own receiver R. For this, S splits its harvested power P_s to constitute the AF relay transmission of the primary signal component x_p with power ζP_s to node Q, and the transmission of secondary signal component x_s with $(1-\zeta)P_s$ to node R, where $\zeta \in (0, 1)$ denotes the power allocation factor (PAF) for spectrum sharing in the proposed CR-WBAN. As such, S broadcasts a superimposed signal given by

$$x_c = \sqrt{\zeta P_s} \frac{y_{ps}}{\sqrt{|y_{ps}|^2}} + \sqrt{(1-\zeta)P_s} x_s. \tag{2.4}$$

Thus, the received signals at nodes Q and R from S in the third sub-block are denoted by y_{sq} and y_{sr}, respectively, and are given as

$$y_{sj} = h_{sj} x_c + n_{sj}, \tag{2.5}$$

where $j \in \{q, r\}$ and n_{sj} is the AWGN.

Consequently, for the primary communication, the instantaneous SNR at Q, via direct link, can be expressed from (2.3) as

$$\gamma_{pq} = \eta_p |h_{pq}|^2, \tag{2.6}$$

where $\eta_p = \frac{P_p}{N_o}$ is the transmit SNR, while the end-to-end SNR at Q via the relay link under TSC protocol can be expressed using (2.2)-(2.5) as

$$\gamma_{psq} = \frac{\zeta \gamma_{ps} \beta |h_{sq}|^2}{(1-\zeta)\gamma_{ps}\beta|h_{sq}|^2 + \zeta\beta|h_{sq}|^2 + 1}, \tag{2.7}$$

[2]Our proposed work assumes a static body in WBAN, and therefore, the only noise involved here is the thermal noise. Many studies involving a static body in WBAN have been reported in the existing literature (see [48] and [51] and the references therein), and such a scenario can be found in many practical setups such as a resting body in WBAN. Other sources of noise derived from body motion will be considered in future studies wherein this work can be used as benchmark.

where $\gamma_{ps} = \eta_p |h_{ps}|^2$ and $\beta = \frac{2\alpha\Theta}{1-\alpha}$.

For the secondary network, we can observe from (2.5) that the received signal at R contains a primary signal component x_p as interference which can be eliminated [52] by utilizing the primary signal received before in the second sub-block transmission phase. Thereby, the resultant SNR at node R can be represented as

$$\gamma_{psr} = \frac{(1-\zeta)\beta\gamma_{ps}|h_{sr}|^2}{\zeta\beta|h_{sr}|^2 + 1}. \tag{2.8}$$

Note that the SNR expressions in (2.7) and (2.8) are derived by ignoring the noise statistic at the relay [53] for simplicity.

2.1.2 PSC Protocol

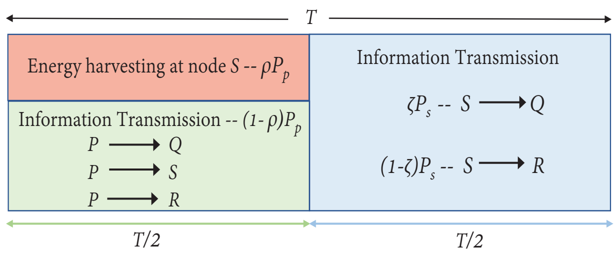

Figure 2.4: Transmission block structure for the PSC protocol.

In the PSC protocol, the block transmission time T is divided into two sub-blocks owing to the half-duplex operation, where one half is used for primary transmissions and the other half is used for secondary transmissions, as shown in Fig. 2.4. During the first transmission phase, node P transmits a unit energy signal x_p and thus, the signals received at nodes Q, S, and R can be given by y_{pq}, y_{ps}, and y_{pr}, respectively, and expressed as

$$y_{pj} = \sqrt{P_p} h_{pj} x_p + n_{pj}, \tag{2.9}$$

where $j \in \{q, s, r\}$ and n_{pj} represents the AWGN.

Herein, S splits the received signal y_{ps} into two parts through a PSC parameter ρ $(0 \leq \rho \leq 1)$. Particularly, $\sqrt{\rho} y_{ps}$ is used for harvesting energy to replenish its battery and $\sqrt{(1-\rho)} y_{ps}$ is used for information processing. Therefore, the received signal at the input of the energy harvester is given by

$$\sqrt{\rho} y_{ps} = \sqrt{\rho P_p} h_{ps} x_p + \sqrt{\rho} n_{ps}. \tag{2.10}$$

From (2.10), the harvested energy at S can be expressed as

$$E_s = \frac{\Theta \rho P_p |h_{ps}|^2 T}{2}, \tag{2.11}$$

where $0 \leq \Theta \leq 1$ is the energy conversion efficiency for the inverter circuitry at S, and the noise statistic is ignored [16] as we aimed at harvested energy with $P_s \ll P_p$.

The power will be dispensed for the remaining $T/2$ time and hence, given by

$$P_s = \frac{E_s}{T/2}, \tag{2.12}$$

which can be further represented using (2.11) as

$$P_s = \Theta \rho P_p |h_{ps}|^2. \tag{2.13}$$

On the other hand, the base-band signal received by information receiver (IR) at S is given by

$$\begin{aligned} Y_{PS} &= \sqrt{(1-\rho)} y_{ps} \\ &= \sqrt{(1-\rho) P_p} h_{ps} x_p + \sqrt{(1-\rho)} n_{ps} + n_{\mathrm{RF}}, \end{aligned} \tag{2.14}$$

where n_{RF} is the sampled AWGN due to RF to base-band signal conversion. Therefore, the total AWGN noise at IR is $n_{PS} = \sqrt{(1-\rho)} n_{ps} + n_{\mathrm{RF}}$.

In the second transmission phase, node S serves as an AF relay for primary communication, while at the same time, communicates with its own receiver R. As such, S amplifies and forwards the signal received at IR in the first phase to node Q while simultaneously transmitting its own information signal x_s to node R. For this concurrent transmission, S employs sophisticated signal processing techniques to split its harvested power P_s through the spectrum sharing factor $\zeta \in (0,1)$ to superimpose its signal x_s with Y_{ps} to generate a combined signal given by

$$x_c = \sqrt{\zeta P_s} \frac{Y_{PS}}{\sqrt{|Y_{PS}|^2}} + \sqrt{(1-\zeta) P_s} x_s. \tag{2.15}$$

Thus, the received signals at nodes Q and R from S can be represented by y_{sq} and

y_{sr}, respectively, given as

$$y_{sj} = h_{sj}x_c + n_{sj}, \tag{2.16}$$

where $j \in \{q, r\}$ and n_{sj} is the AWGN.

Hereby, for primary communications, the SNR at Q via the direct link can be written using (2.9) as

$$\gamma_{pq} = \eta_p|h_{pq}|^2, \tag{2.17}$$

and the SNR at Q, via relay link, can be formulated using (2.13)-(2.16) as

$$\gamma_{psq} = \frac{\zeta\gamma_{ps}\delta|h_{sq}|^2}{(1-\zeta)\gamma_{ps}\delta|h_{sq}|^2 + \zeta\varrho|h_{sq}|^2 + 1}, \tag{2.18}$$

where $\gamma_{ps} = \eta_p|h_{ps}|^2$, $\delta = \Theta\rho$, and $\varrho = \frac{\Theta\rho}{1-\rho}$.

For the secondary communication, it can be observed from (2.16) that the received signal at R involves a primary signal component in x_c as interference which can be successfully removed [52] using the primary signal decoded in the first transmission phase. Thus, the instantaneous SNR at R can be expressed as

$$\gamma_{psr} = \frac{(1-\zeta)\delta\gamma_{ps}|h_{sr}|^2}{\zeta\varrho|h_{sr}|^2 + 1}. \tag{2.19}$$

As done previously, the SNR expressions in (2.18) and (2.19) are deduced by neglecting the noise statistic at the relay [53].

2.2 Performance Analysis

In this section, we conduct a comprehensive performance analysis of the CR-WBAN using the TSC and PSC protocols as described previously. Specifically, we derive the OP expressions for both primary and secondary communications. In addition, to gain more insights into the overall system performance, we provide expressions for the throughput and energy efficiency. Moreover, we examine the impact of the power splitting factor ζ, TSC parameter α, and PSC parameter ρ on the overall performance of the CR-WBAN.

To proceed with the analysis, we first present the statistics of the pertinent fading channels. Considering the log-normal fading model for WBAN, the probability density function (PDF) and cumulative distribution function (CDF) of $|h_{ij}|^2$, for $i \in \{p, s\}$ and $j \in \{q, s, r\}$ with $i \neq j$, can be given, respectively, by [50], [54]

$$f_{|h_{ij}|^2}(x) = \frac{1}{2\sqrt{2\pi}\sigma_{ij}x} \exp\left(-\left(\frac{\ln(x) - 2\mu_{ij}}{2\sqrt{2}\sigma_{ij}}\right)^2\right), \tag{2.20}$$

and

$$F_{|h_{ij}|^2}(x) = \frac{1}{2}\left(1 + \operatorname{erf}\left(\frac{\ln(x) - 2\mu_{ij}}{2\sqrt{2}\sigma_{ij}}\right)\right), \tag{2.21}$$

where the parameters μ_{ij} and σ_{ij} represent the mean and standard deviation, respectively, and $\operatorname{erf}(\cdot)$ is the standard error function.

2.2.1 Outage Probability of Primary Network

For the primary network, we examine the OP with and without spectrum sharing in the presence of the direct ($P \to Q$) link communication. In what follows, we conduct the OP analysis of the primary network for both the TSC and PSC protocols in a unified manner. For this, we can express their respective SNRs from (2.7) and (2.18) in a common form as

$$\gamma_{psq} = \frac{\zeta\gamma_{ps}\beta_1|h_{sq}|^2}{(1-\zeta)\gamma_{ps}\beta_1|h_{sq}|^2 + \zeta\beta_2|h_{sq}|^2 + 1}, \tag{2.22}$$

with $\beta_1 = \beta_2 = \frac{2\alpha\Theta}{1-\alpha}$ for TSC protocol, whereas $\beta_1 = \Theta\rho$ and $\beta_2 = \frac{\Theta\rho}{1-\rho}$ for PSC protocol.

Direct Link (DL) Transmission Solely

For a target rate R_p, the OP of the primary network using DL transmission solely (i.e., with no spectrum sharing) is given by

$$P_{out}^{\mathrm{DL}}(R_p) = \Pr\left[\log_2\left(1 + \gamma_{pq}\right) < R_p\right]. \tag{2.23}$$

It should be noted that the DL transmission solely scheme requires only a single phase of transmission from node P to node Q. We can further express (2.23) as

$$P_{out}^{\mathrm{DL}}(R_p) = F_{\gamma_{pq}}(\gamma_p'), \tag{2.24}$$

where $\gamma'_p = 2^{R_p} - 1$. We can obtain the expression of the CDF $F_{\gamma_{pq}}(x)$ from (2.21) by applying a transformation of random variable as

$$F_{\gamma_{pq}}(x) = \frac{1}{2}\left(1 + \operatorname{erf}\left(\frac{\ln(x) - \ln(\eta_p) - 2\mu_{pq}}{2\sqrt{2}\sigma_{pq}}\right)\right). \tag{2.25}$$

Thus, by evaluating the CDF $F_{\gamma_{pq}}(x)$ in (2.25) at $x = \gamma'_p$, one can compute the required OP of DL transmission solely.

Spectrum Sharing Cooperation with DL Transmission

For a target rate R_p, the OP of the PU for the considered CR-WBAN using the TSC/PSC protocol can be expressed with the application of MRC by making use of (2.6) or (2.17) and (2.22) as

$$\begin{aligned} P_{out}^{\mathrm{Pri}}(R_p) &= \Pr\left[\frac{1}{\varpi}\log_2(1 + \gamma_{pq} + \gamma_{psq}) < R_p\right] \\ &= \Pr\big[\Lambda_p < \gamma_p\big] = F_{\Lambda_p}(\gamma_p), \end{aligned} \tag{2.26}$$

with $\Lambda_p = \gamma_{pq} + \gamma_{psq}$ and $\gamma_p = 2^{\varpi R_p} - 1$, where $\varpi = 2$ for the PSC protocol and $\varpi = \frac{2}{1-\alpha}$ for the TSC protocol. Hereby, (2.26) can be re-expressed as

$$\begin{aligned} F_{\Lambda_p}(\gamma_p) &= \Pr\big[(\gamma_{pq} + \gamma_{psq}) < \gamma_p\big] \\ &= \int_0^{\gamma_p}\int_0^{\gamma_p - y} f_{\gamma_{psq}}(x) f_{\gamma_{pq}}(y)\,dx\,dy. \end{aligned} \tag{2.27}$$

Now, to evaluate (2.27), we first compute the CDF $F_{\gamma_{psq}}(x)$ in the following theorem.

Theorem 1. *The CDF $F_{\gamma_{psq}}(x)$ of the CR-WBAN with the TSC/PSC protocol under log-normally distributed links is given by*

$$F_{\gamma_{psq}}(x) = \begin{cases} 1, & \text{if } x \geq \frac{\zeta}{1-\zeta}; \\ \phi(x), & \text{if } x < \frac{\zeta}{1-\zeta}, \end{cases} \tag{2.28}$$

where $\phi(x)$ is given by

$$\phi(x) = \int_0^\infty \frac{1}{2}\left(1+\operatorname{erf}\left(\frac{\ln\left(\frac{x(1+\zeta\beta_2 y)}{\beta_1(\zeta-(1-\zeta)x)y}\right)-2\mu_{ps}}{2\sqrt{2}\sigma_{ps}}\right)\right)$$
$$\times \frac{1}{2\sqrt{2\pi}\sigma_{sq}y}\exp\left(-\left(\frac{\ln(y)-2\mu_{sq}}{2\sqrt{2}\sigma_{sq}}\right)^2\right)dy. \tag{2.29}$$

Proof. It is provided in Appendix A. ■

From (2.28), we can realize that the condition $x < \frac{\zeta}{1-\zeta}$ allows the secondary node (relay) cooperation to be effective, otherwise the unity CDF is obtained as a result and implies outage of the secondary communication in the proposed CR-WBAN. Hence, by exploiting the CDF expression from (2.28) into (2.27), one can proceed with the analysis under the condition $\left(\gamma_p < \frac{\zeta}{1-\zeta}\right)$ for an effective secondary cooperation. However, as such, it seems to be mathematically intractable to obtain a useful solution. Therefore, with the aid of an M-step staircase approximation approach [76] for the involved triangular integral region in (2.27), the OP can be expressed as

$$P_{out}^{\mathrm{Pri}}(R_p) \approx \sum_{i=0}^{M-1}\left\{F_{\gamma_{pq}}\left(\frac{i+1}{M}\gamma_p\right) - F_{\gamma_{pq}}\left(\frac{i}{M}\gamma_p\right)\right\} F_{\gamma_{psq}}\left(\frac{M-i}{M}\gamma_p\right). \tag{2.30}$$

Thus, after substituting the CDF $F_{\gamma_{pq}}(x)$ from (2.25) and the CDF $F_{\gamma_{psq}}(x)$ from (2.28) into (2.30), one can get the desired OP expression.

2.2.2 Outage Probability of Secondary Network

To carry out a unified performance analysis of the secondary communication network, we represent the SNRs at node R for the TSC and PSC protocols from (2.8) and (2.19) in a generalized form as

$$\gamma_{psr} = \frac{(1-\zeta)\beta_1\gamma_{ps}|h_{sr}|^2}{\zeta\beta_2|h_{sr}|^2+1}, \tag{2.31}$$

with $\beta_1 = \beta_2 = \frac{2\alpha\Theta}{1-\alpha}$ for the TSC protocol, whereas $\beta_1 = \Theta\rho$ and $\beta_2 = \frac{\Theta\rho}{1-\rho}$ for the PSC protocol. For a given target rate R_s, the OP of the secondary communication can be given by

$$P_{out}^{\text{Sec}}(R_s) = \Pr\left[\frac{1}{\varpi}\log_2(1+\gamma_{psr}) < R_s\right]$$
$$= \Pr\left[\gamma_{psr} < \gamma_s\right] = F_{\gamma_{psr}}(\gamma_s), \tag{2.32}$$

where $\gamma_s = 2^{\varpi R_s} - 1$ with $\varpi = 2$ for the PSC protocol and $\varpi = \frac{2}{1-\alpha}$ for the TSC protocol. Further, $P_{out}^{\text{Sec}}(R_s)$ can be evaluated through the computation of the CDF $F_{\gamma_{psr}}(x)$ as given in Theorem 2.

Theorem 2. *The CDF $F_{\gamma_{psr}}(x)$ of the CR-WBAN using the TSC/PSC protocol under log-normal fading channels is given by*

$$F_{\gamma_{psr}}(x) = \int_0^\infty \frac{1}{2}\left(1 + \text{erf}\left(\frac{\ln\left(\frac{x(1+\zeta\beta_2 y)}{\beta_1(1-\zeta)y}\right) - 2\mu_{ps}}{2\sqrt{2}\sigma_{ps}}\right)\right)$$
$$\times \frac{1}{2\sqrt{2\pi}\sigma_{sr}y}\exp\left(-\left(\frac{\ln(y) - 2\mu_{sr}}{2\sqrt{2}\sigma_{sr}}\right)^2\right)dy. \tag{2.33}$$

Proof. It is relegated to Appendix B. ■

Thus, for a target rate R_s, one can determine $P_{out}^{\text{Sec}}(R_s)$ using (2.33) at $x = \gamma_s$, and thereby, obtain the OP of the secondary communication.

2.2.3 Constrained Power Allocation Policy for Spectrum Sharing

Aiming at the power allocation policy for spectrum sharing at the secondary node S, we can deduce an appropriate value of ζ while satisfying the QoS criterion of the primary network. Hereby, from (2.28), recalling the condition $\gamma_p < \frac{\zeta}{1-\zeta}$, the permissible range of power allocation factor for a predetermined threshold γ_p of the primary network can be calculated as

$$\frac{\gamma_p}{1+\gamma_p} < \zeta < 1. \tag{2.34}$$

However, from (2.26), it is clear that γ_p depends on R_p as well as on ϖ. As such, using the aforesaid spectrum sharing condition for the TSC protocol, we first compute the critical value of TSC parameter α to attain a minimum OP as elaborated in Sec. 2.3. Then, using this value of α, we calculate the effective value of ζ to realize spectrum sharing cooperation. Moreover, it is worth noting that a smaller value of ζ can provide more spectrum sharing opportunities towards the secondary network access.

2.2.4 Network Throughput

Here, we compute the delay-limited throughput which is a key performance measure to characterize spectrum utilization for the CR-WBAN. For the cooperative communication based wireless systems, it can also be referred to as mean spectral efficiency. It is defined as the transmission rate that can be guaranteed in all fading states under finite delay constraints without resorting to the long-term asymptotic behavior [53], [86]. For the proposed CR-WBAN, it can be quantified as the sum of individual target rates for both the primary and secondary communications that can be achieved successfully over the log-normal fading channels. Based on the derived OP expressions, we can formulate the network throughput as

$$\mathcal{S}_{\mathcal{T}} = \frac{1}{\varpi}\left[(1 - P_{out}^{\mathrm{Pri}}(R_p))R_p + (1 - P_{out}^{\mathrm{Sec}}(R_s))R_s\right], \tag{2.35}$$

where $P_{out}^{\mathrm{Pri}}(R_p)$ and $P_{out}^{\mathrm{Sec}}(R_s)$ represent the OP measures for the primary and secondary communications, respectively, as obtained in previous subsections. In (2.35), by setting $R_p = R_s = \mathfrak{R}$, the maximum system throughput achievable is $\mathcal{S}_{\mathcal{T}} = \frac{2\mathfrak{R}}{\varpi}$. Thus, based on ϖ, we can readily find that the maximum system throughput for the PSC protocol equals to $\mathfrak{R}$, whereas it amounts to $\mathfrak{R}(1-\alpha)$ for the TSC protocol.

2.2.5 Energy Efficiency

Relying on the throughput expression in (2.35), we analyze the energy efficiency of the EH-based CR-WBAN under study. An implication of such analysis is that it can help to design an EH-aware CR-WBAN to prolong the network lifetime. Fundamentally, the energy efficiency for the system can be defined as the total amount of data delivered to the total amount of consumed energy [86], [78]. The total amount of data delivered can be quantified by the system throughput defined in (2.35). While the total energy consumed in the network, for the TSC protocol, is the sum of energy consumed by the primary source P in the first sub-block EH phase (of duration αT) and the energy consumed by it in the second sub-block transmission phase (of duration $(1-\alpha)T/2$). Note that the energy consumed in the

Table 2.1: Log-normal distribution parameters for CR-WBAN.

μ_{ij}, σ_{ij}	Right arm (Q)	Center waist (S)	Left leg (R)
Chest (P)	$-2.17, 4.92$	$-0.77, 2.89$	$-1.32, 3.76$
Center waist (S)	$-0.15, 1.18$	- -	$-0.83, 2.84$

third sub-block transmission phase is the energy harvested by the secondary node S in the first sub-block EH phase, and hence, does not contribute to the total energy consumed in the network. On the contrary, for the PSC protocol, the total energy consumed is simply the energy consumed by the primary source P in the first half of the block transmission (i.e., of duration $T/2$). Consequently, the expression of energy efficiency for the considered CR-WBAN, under a delay-limited scenario, can be given as

$$\Xi_{\mathcal{E}} = \begin{cases} \frac{\mathcal{S}_{\mathcal{T}}}{\frac{P_p}{2}(1+\alpha)}, & \text{for TSC protocol;} \\ \\ \frac{\mathcal{S}_{\mathcal{T}}}{\frac{P_p}{2}}, & \text{for PSC protocol,} \end{cases} \tag{2.36}$$

where $\mathcal{S}_{\mathcal{T}}$ represents the achievable throughput of the CR-WBAN as expressed in (2.35).

2.3 Numerical and Simulation Results

In this section, we aim to demonstrate the performance of the proposed CR-WBAN using the TSC and PSC protocols through numerical investigations along with Monte Carlo simulations. Based on the characteristics of the CR-WBAN, the following parameters are adopted throughout this section: the transmit power of primary source $P_p = 1$ mW and the energy conversion efficiency $\Theta = 0.7$. The parameters of the log-normal fading distribution are shown in Table 2.1. This is taken according to [55] by considering the CR-WBAN configuration with node locations as follows: P is located on the chest, Q is placed on the right arm, S is positioned on the center waist, and R is placed on the left leg.

In subsequent investigations, we obtain the analytical OP curves for the primary network using (2.30) with $M = 50$ to achieve sufficient accuracy, and that for the secondary network using (2.33), through the aid of MATHEMATICA software. Meanwhile, Monte Carlo simulations results are obtained using the popular comput-

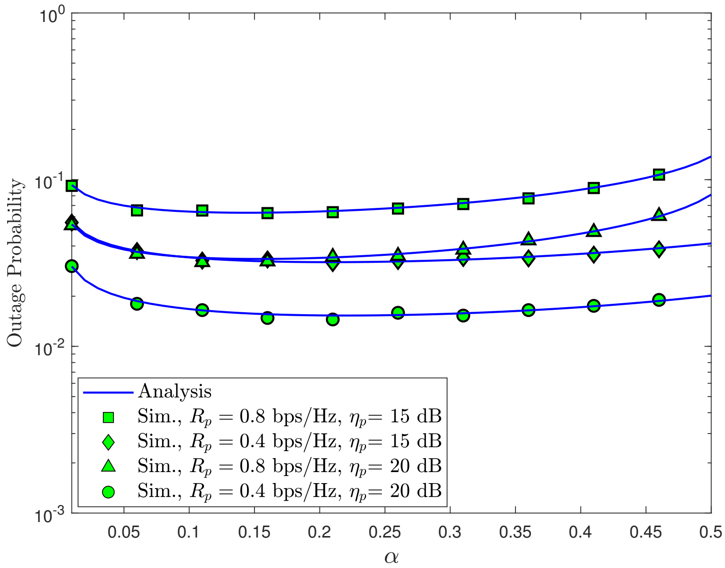

Figure 2.5: OP versus α of primary network with TSC protocol.

ing software MATLAB. We find that in all the forthcoming figures, the analytical curves are in good agreement with the Monte Carlo simulations results. Fig. 2.5 illustrates the impact of the TSC parameter α on the OP performance of the primary network in the proposed CR-WBAN under different sets of values of target rate R_p and SNR η_p. Hereby, we appropriately choose the values of α and ζ while satisfying the spectrum sharing condition $\frac{\gamma_p}{1+\gamma_p} < \zeta < 1$, as disclosed in Sec. 2.2.3. From various curves in this figure, we obtain the critical value of α as 0.2 to achieve the minimum OP, while the effective value of ζ is fetched as 0.8 to facilitate spectrum sharing cooperation.

Fig. 2.6 depicts the OP versus SNR curves with varying target rates ($R_p = 0.4, 0.6, 0.8$ bps/Hz) for the primary communication network using the TSC protocol. Herein, we set $\alpha = 0.2$ and $\zeta = 0.8$. For comparison purposes, the OP curves for the DL transmission solely are also plotted using (2.25) in Fig. 2.6. We can see that the proposed CR-WBAN with the TSC protocol significantly outperforms the DL transmission solely scheme, especially in the medium to high SNR region. This is owing to the additional diversity gain acquired through the cooperative relaying link under the TSC protocol. Further, it is apparent that the OP performance of the proposed CR-WBAN degrades as R_p increases from 0.4 to 0.8 bps/Hz. This is because increasing the data rate requires higher SNR and more complex modulation schemes, which can increase susceptibility to interference, noise, and channel impairments, leading to degradation in the outage performance of the system.

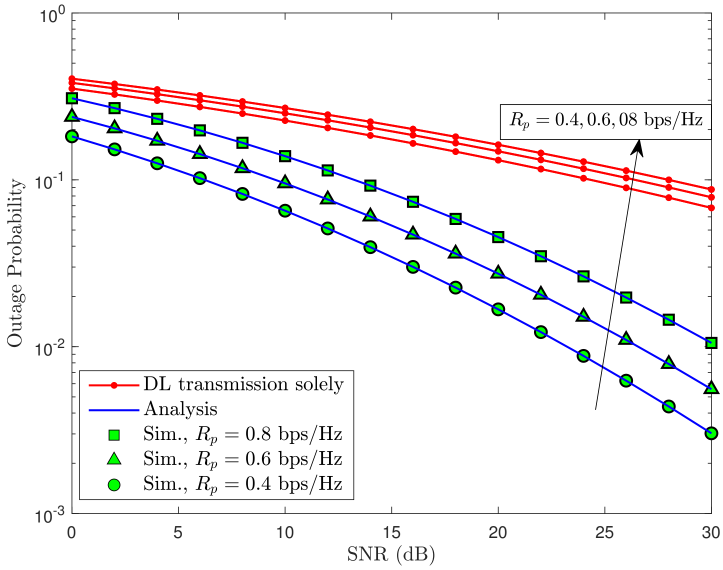

Figure 2.6: OP versus SNR of primary network with TSC protocol.

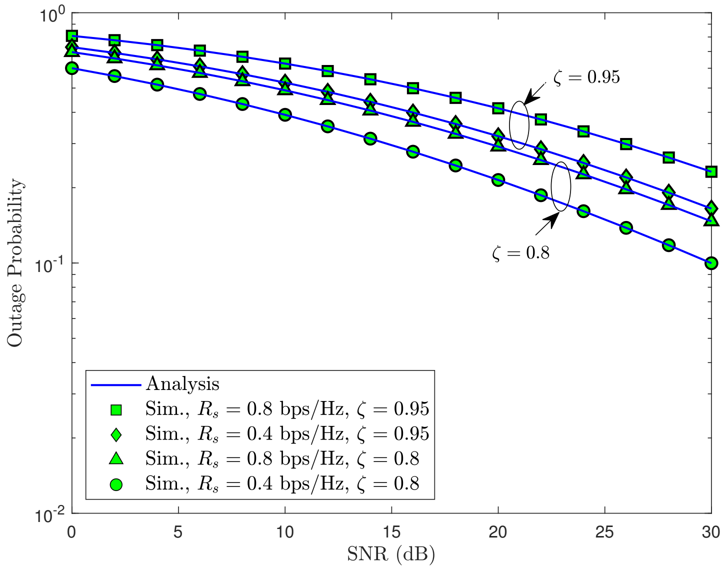

Figure 2.7: OP versus SNR of secondary network with TSC protocol.

Fig. 2.7 shows the OP performance curves for the secondary communication of the proposed CR-WBAN using TSC protocol (by setting $\alpha = 0.2$). Here, we plot the curves for various sets of values of R_s and ζ. As can be seen from this figure, the OP performance of the secondary network degrades with an increase in R_s and/or ζ. This is expected because, with an increase in ζ, more power is allocated for primary signal cooperation and correspondingly less power is utilized for the secondary communication. Thereby, a lower value of ζ is desirable for improving the performance of secondary network.

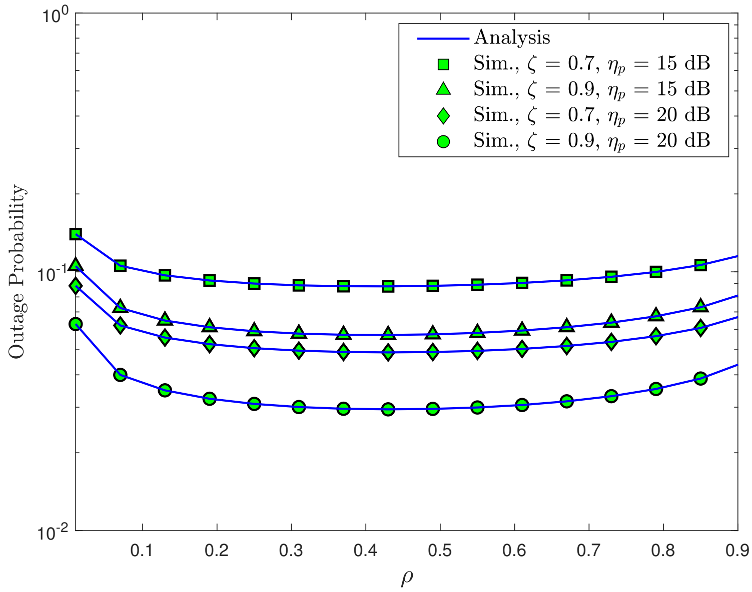

Figure 2.8: OP versus ρ of primary network with PSC protocol.

Fig. 2.8 demonstrates the impact of the PSC parameter ρ on the outage performance of the primary network under various settings of ζ and η_p. Here, we fix the target rate as $R_p = 0.8$ bps/Hz so that the allowable range of ζ comes out to be $0.67 < \zeta < 1$. From this figure, we can see that there exists a critical value of ρ at which the OP of primary communication is minimum. We fetch the critical value of ρ as 0.43, while the effective value of ζ is taken as 0.7 to facilitate spectrum sharing cooperation. Note that this effective value of ζ is relatively low for the PSC protocol than that for the TSC protocol.

In Fig. 2.9, we present the OP versus SNR curves for the primary communication network using the PSC protocol at various target rates ($R_p = 0.4, 0.6, 0.8$ bps/Hz) with a setting of $\rho = 0.43$ and $\zeta = 0.8$. It is easily realized that the OP performance of the primary network with the PSC protocol significantly improves, as compared to that of the DL transmission solely scheme, in the mid-to-high SNR region. By comparing with the OP performance of the primary network using the TSC protocol in Fig. 2.6, we infer that the PSC protocol performs slightly better than the TSC protocol, under the same set of system parameters. This is more noticeable in the low SNR region.

Fig. 2.10 illustrates the OP versus SNR curves for the secondary communication network using the PSC protocol (with setting $\rho = 0.43$) at various sets of values of R_s and ζ. We can observe that the OP performance of the secondary network deteriorates while increasing the value of R_s and/or ζ (thereby allocating less power

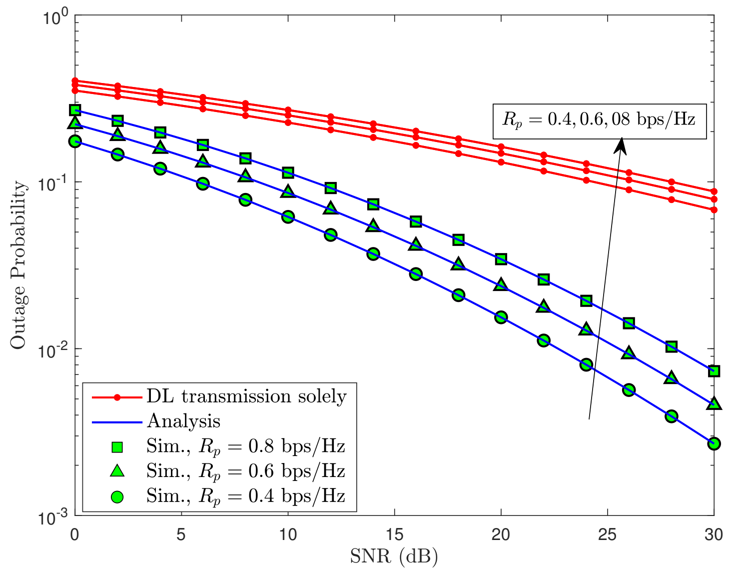

Figure 2.9: OP versus SNR of primary network with PSC protocol.

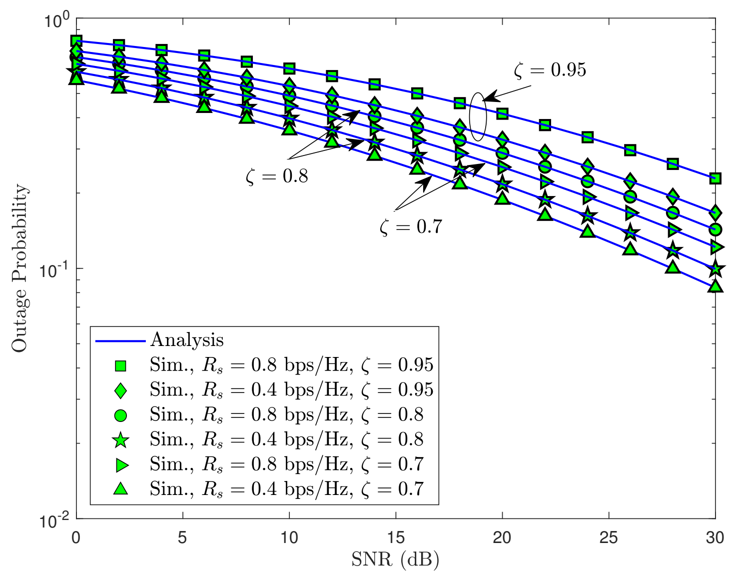

Figure 2.10: OP versus SNR of secondary network with PSC protocol.

to the secondary communication). However, we can see that the performance of the secondary network can be improved for the PSC protocol as compared to that of the TSC protocol in Fig. 2.7. This is attributed to the lower effective value of the spectrum sharing factor ζ. As such, we can conclude that the PSC protocol offers more flexibility to secondary spectrum access.

In Fig. 2.11, we evaluate the system throughput performance of the proposed CR-WBAN using the TSC and PSC protocols under the setting $R_p = R_s = 0.4, 0.8$ bps/Hz. For the TSC protocol, we consider the critical value of $\alpha = 0.2$ and accord-

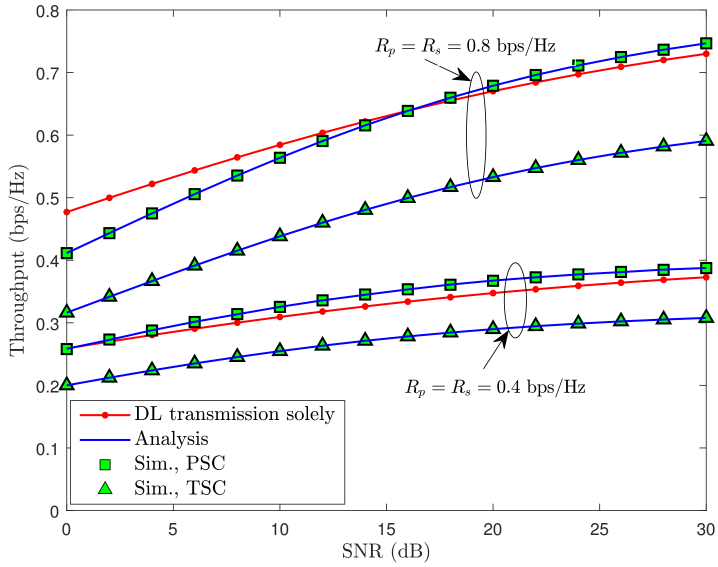

Figure 2.11: System throughput for the CR-WBAN.

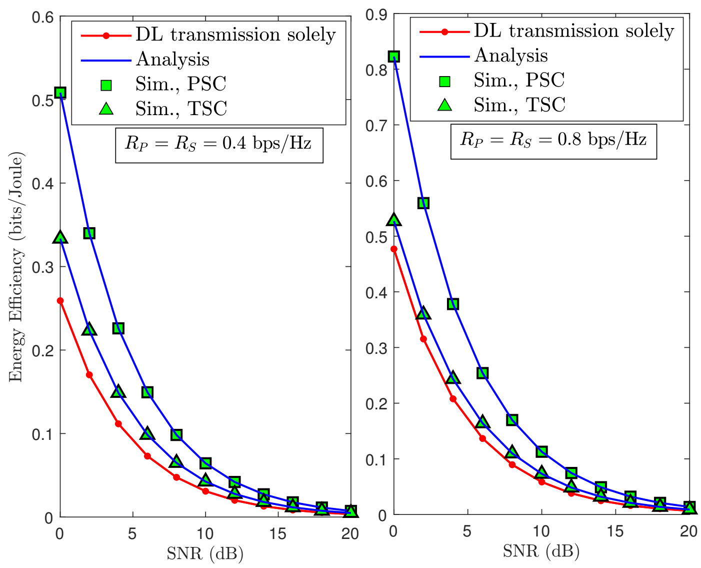

Figure 2.12: Energy efficiency for the CR-WBAN.

ingly the effective value of $\zeta = 0.53$ for $R_p = 0.4$ bps/Hz and $\zeta = 0.78$ for $R_p = 0.8$ bps/Hz. Likewise, for the PSC protocol, we set the critical value of $\rho = 0.43$ and accordingly the effective value of $\zeta = 0.45$ for $R_p = 0.4$ bps/Hz and $\zeta = 0.7$ for $R_p = 0.8$ bps/Hz. First, we can see that the throughput tends to attain its maximum value as the SNR becomes large. Moreover, the throughput performance of the PSC protocol is much better than the TSC protocol over the entire SNR region and it exceeds that of the DL transmission solely scheme at high SNR regime.

Fig. 2.12 plots the curves for energy efficiency against SNR of the proposed CR-WBAN with the TSC and PSC protocols at two different sets of target rates (i.e.,

$R_p = R_s = 0.4, 0.8$ bps/Hz). Also, we fix the same set of values for α, ρ and ζ as used in Fig. 2.11. From this figure, we can see that both the TSC and PSC protocols achieve higher energy efficiency than the DL transmission solely scheme, while the PSC protocol has higher energy efficiency than the TSC protocol for the considered CR-WBAN. It can also be noticed that the energy efficiency of the considered network reduces significantly as the SNR increases. This is intuitive because for higher SNR values, the achieved throughput is much lesser than the consumed power.

2.4 Summary

An EH-based overlay CR-WBAN is studied in this chapter, whereby both the primary (medical sensors) and secondary (motion sensors) communications are realized on the human body through a cooperative spectrum sharing technique. We employed two EH-based spectrum sharing cooperation protocols, called TSC and PSC protocols for the considered network, and analyzed their performance in terms of OP, throughput and energy efficiency over the pertinent log-normally distributed fading channels. Our results reveal that the PSC protocol notably outperforms the TSC protocol and thereby explores more spectrum sharing opportunities in the proposed CR-WBAN. Furthermore, the impact of key parameters are highlighted to provide useful insights into the practical design of spectral and energy-efficient WBANs for smart healthcare applications.

CHAPTER 3

OVERLAY COGNITIVE NOMA SYSTEMS WITH INCREMENTAL RELAYING

In the previous chapter, we proposed and examined an energy- and spectrum-efficient CR-WBAN with EH capability. However, with the rapid evaluation of wireless networks to provide universal coverage and communication, it is essential to integrate SWIPT with different spectrum-efficient technologies to accommodate more users and prolong the lifespan of these networks. Among the existing techniques, NOMA has been envisioned as a promising technology to attain higher spectral efficiency and massive connectivity for the future wireless networks [56]-[58]. Recently, the NOMA technique has been commonly debated in the context of CR, which is another potential technique for improving the spectrum efficiency [9]. The incorporation of NOMA into CR, referred to as CNOMA, has demonstrated a potential attribute of fulfilling the criteria of 5G wireless networks such as maximum throughput, broad connectivity, and low latency [59]. With the applicability of CNOMA, several research studies have been coordinated using the underlay [60]-[64] and overlay [23]-[27] approaches. It needs to be acknowledged that the interference from the ST towards PR is counteracted in the overlay CNOMA model in contrast to the underlay CNOMA. Moreover, the interference from PUs and stringent transmit power restrictions on SUs in underlay approach may limit the overall system performance and coverage. On the contrary, due to an increased diversity gain from the ST relaying cooperation, the outage performance of PU can be greatly improved in overlay CNOMA system. Furthermore, an overlay CNOMA model is of vital importance since it can bring network coverage even when the primary direct link is disrupted due to shadowing and obstacles.

By incorporating SWIPT into CNOMA, a more spectral and energy efficient wireless network is expected to be framed with a sustainable environment. There have been diverse research works done by considering SWIPT into CNOMA [18]-[22]. Authors in [18] have investigated a cooperative multiple-input-single-output SWIPT NOMA protocol, where a strong NOMA user serves as an EH relay and assists a weak NOMA user by using the PS protocol. The work in [19] has studied an underlay non-linear EH-assisted CNOMA system to improve the spectral efficiency and secrecy energy efficiency. A SWIPT-enhanced overlay CNOMA system has been studied in [20] to achieve the maximal throughput for the secondary network. Authors in [21] have studied the energy efficiency optimization problem for both the underlay and overlay CNOMA with EH. The outage performance of cooperative CNOMA networks with SWIPT using DF relaying has been investigated in [22], where cognitive relay harvests the transmission power from the ST by exploiting the PS scheme using the fixed power allocation based NOMA protocol. The aforementioned works on SWIPT-enabled CNOMA networks follow the conventional FR strategy which impels the ST to incorporate the relaying operation even when the PR is able to decode its signal through the primary DL, which is not at all an efficient way of utilizing the spectrum. Moreover, they have assumed the ideal case of pSIC for the performance investigation. However, the pSIC is difficult to realize in practice, owing to the many implementation issues, such as complexity scaling and error propagation [24]. Consequently, these critical factors will lead to an error in decoding, causing residual interference signal. Thereby, the effects of ipSIC [25] may pose limitations on the capacity of the SWIPT-based CNOMA network.

Motivated by the prior research studies, in this chapter, we analyze the performance of an EH-assisted overlay CNOMA (EH-OCNOMA) system[1] by adopting an IR protocol under the impacts of ipSIC/pSIC situations. Specifically, we consider a downlink communication scenario wherein a PT communicates to a PR in cooperation with an energy-constrained ST accessing spectrum for its own communication to an SR. The ST employs a TS-based receiver architecture[2] to harvest energy from RF signals of the primary transmissions. Further, it can act as an AF/DF relay and uses the harvested energy to forward the primary signal and to transmit its

[1]The considered EH-OCNOMA system comprises of the power-constrained low-cost SU nodes, capturing the application scenarios of device-to-device (D2D) networks, small cell (picocell and femtocell) networks, and wireless sensor networks, which generally do not have a dedicated spectrum for their communication.

[2]In contrast to PS-based receiver, the TS-based receiver is simpler to implement (using hardware with simple switching circuits) and more suitable for low-cost devices [66].

own signal simultaneously using the NOMA principle. Importantly, the proposed IR protocol invokes secondary relay cooperation adaptively, depending on the limited feedback mechanism from the PU. It can thus proficiently utilize the available degrees-of-freedom to improve the system performance of EH-OCNOMA. The major contributions of this chapter are emphasized as follows:

- We propose two EH-based CSS schemes based on the IR protocol using the AF and DF relaying strategies, namely CSS-IAF and CSS-IDF, and compare their performance with the competitive FR-based schemes. We also discuss the DLT scheme as a baseline to compare with the performance of CSS schemes for the considered EH-OCNOMA system. Further, we portray the relative performance advantages of CSS with NOMA over its OMA counterpart.

- Based on the received SNRs and SINRs, we extensively analyze the outage performance of CSS-IAF and CSS-IDF schemes by deriving the OP expressions of the primary and secondary networks under the ipSIC/pSIC situations over a Nakagami-m fading[3] environment.

- To garner further insight, we also deduce the expressions of system throughput and energy efficiency for the considered EH-OCNOMA system.

- Finally, for the effective design of the proposed EH-OCNOMA system, we provide an insight into the NOMA PAF to explore the spectrum sharing opportunities.

The rest of the chapter is organized as follows. Section 3.1 illustrates the system model and the proposed IR protocol for the EH-OCNOMA system, while deriving the end-to-end SNRs/SINRs for the primary and secondary networks. Section 3.2 investigates the performance of the primary network by evaluating the analytical expressions of the OP for the DLT, CSS-IAF, and CSS-IDF schemes. The OP expressions of the secondary network, while considering both the ipSIC and pSIC situations, have been evaluated in Section 3.3. The system throughput and the energy efficiency expressions for the proposed EH-OCNOMA system are presented in Section 3.4. Section 3.5 portrays the results and discussions, followed by some

[3]The Nakagami-m fading model represents a general distribution wherein various fading environments, i.e., severe, light or no fading, can be modeled [67]. Moreover, it gives the best fit of the statistical characteristics of a land mobile system, complex environments and ionospheric radio links.

concluding remarks in Section 3.6. Moreover, the proofs of theorems/lemmas used in this chapter are included in the appendices.

3.1 System Model and Protocol Description

This section first provides a detailed description of the EH-OCNOMA system model and thereafter presents the end-to-end SINR/SNR expressions for the AF/DF relaying strategies, followed by elaborating the proposed IR protocol for the considered system.

3.1.1 System Model

As depicted in Fig. 3.1, we consider an EH-OCNOMA system where a primary network coexists with a secondary network. The primary network comprises of a transmitter node P with its corresponding receiver node Q, whereas the secondary network includes an energy-constrained ST node S and SR node R. Herewith, node P establishes a communication directly with node Q. Although a primary DL between node P and node Q is supposed to exist, node P may still seek the ST's cooperation to exploit the diversity benefits. As an incentive for the cooperation with the primary network, the secondary network accesses the licensed spectrum of the primary network. Since S is an energy-constrained node, it first harvests energy from the received RF signal and then splits the corresponding harvested power to relay the primary signal and to transmit its own signal simultaneously using the NOMA principle. For this, it employs a TS-based receiver architecture, as shown in Fig. 3.2. Herein, the transmission block duration is divided into two phases of durations αT and $(1-\alpha)T$, with $\alpha \in (0,1)$ being the TS parameter. The first phase of duration αT corresponds to an EH phase, wherein the ST node S harvests the energy using the received RF signal from node P, and utilizes this energy further to broadcast the amalgamated signal in the second phase of duration, i.e., information transmission (IT) phase. The duration $(1-\alpha)T$ is further subdivided into two IT phases to establish the overall communication. It is assumed that all the nodes are equipped with single antenna and operate in half-duplex mode. All the channels are assumed to follow block fading, which means they remain unchanged for a particular block and may change for the subsequent block transmissions independently. Further, all the links are subject to independent Nakagami-m fading and the channel gain from node i to node j is represented by h_{ij}, where $i \in \{p, s\}$ and $j \in \{q, s, r\}$ with $i \neq j$. All the receiving nodes are assumed to be inflicted by the AWGN, i.e., modelled as $\mathcal{CN}(0, N_o)$.

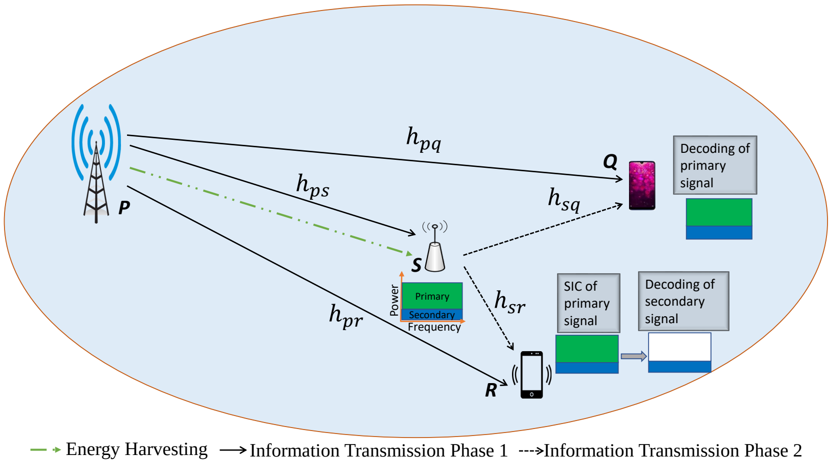

Figure 3.1: System model.

3.1.2 EH Phase

During αT duration, node S harvests energy[4] from the transmitted RF signal through node P, which can be given by

$$E_s = \Theta P_p |h_{ps}|^2 \alpha T, \tag{3.1}$$

where P_p is the transmit power at node P and Θ $(0 < \Theta \leq 1)$ is the energy conversion efficiency that relies on the rectification process and the associated EH circuitry [16]. Consequently, the transmit power at node S over the time $(1-\alpha)T/2$ can be obtained as

$$P_s = \frac{E_s}{(1-\alpha)T/2} = \frac{2\alpha\Theta P_p |h_{ps}|^2}{1-\alpha} = \beta P_p |h_{ps}|^2, \tag{3.2}$$

where $\beta = \frac{2\alpha\Theta}{1-\alpha}$. Hereby, the overall communication takes place in two IT phases, as discussed in the following subsection.

[4]Herein, we consider a linear EH model for analytical tractability, as followed in many previous works [18]-[22]. A non-linear EH model [68] would however be more practical and may be tackled in the future work. Nevertheless, our present results can be treated as a benchmark for the futuristic design.

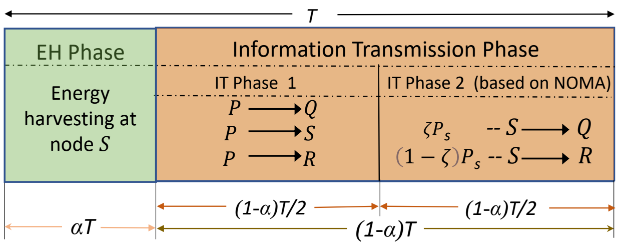

Figure 3.2: Transmission Block Structure for EH and IT phase.

3.1.3 IT Phase

During the first IT phase, node P transmits a primary signal x_p towards node Q, complying with $\mathbb{E}[|x_p|^2] = 1$, which is also received by the secondary nodes S and R. Thus, the received signal at node i, with $i \in \{q, s, r\}$, can be expressed as

$$y_{pi} = \sqrt{P_p} h_{pi} x_p + n_{pi}, \tag{3.3}$$

where n_{pi} is the AWGN term. Accordingly, the resulting SNR at node i through the DL can be written as

$$\gamma_{pi}^{\mathrm{DL}} = \eta_p |h_{pi}|^2, \tag{3.4}$$

with $\eta_p = \frac{P_p}{N_o}$ represents the transmit SNR at node P.

In what follows, we discuss the AF and DF based relaying strategies and thereby obtain the associated SINR expressions.

AF Relaying

During the second IT phase, node S amplifies the received primary signal y_{ps} and superimposes with its own information signal x_s to generate a combined signal x_s^{AF} by exploiting the NOMA principle. This superimposed signal x_s^{AF} is further broadcasted towards nodes Q and R. For this, the harvested power P_s is divided such that ζP_s power is utilized to forward the signal y_{ps} and remaining power $(1 - \zeta)P_s$ is used in transmitting the signal x_s, where $\zeta \in$ (0,1) signifies the NOMA-based power allocation parameter. Due to the higher priority of the primary network, more power is allocated to node Q, resulting in $\zeta \in$ (0.5,1). As such, the transmitted signal by the node S is given by

$$x_s^{\mathrm{AF}} = \sqrt{\zeta P_s} \mathcal{G} y_{ps} + \sqrt{(1 - \zeta) P_s} x_s, \tag{3.5}$$

where the variable gain relaying amplification factor $\mathcal{G}$ at the AF-based relay can be expressed [69] as $\mathcal{G} = \sqrt{\frac{1}{P_p|h_{ps}|^2+N_o}}$, which can be further approximated as $\mathcal{G} \approx \sqrt{\frac{1}{P_p|h_{ps}|^2}}$ for analytical simplicity [65], [70]. Such approximation yields very accurate results over the entire region of operating SNR. Hereafter, the received signal at node j, where $j \in \{q, r\}$, can be expressed as

$$y_{sj}^{\mathrm{AF}} = h_{sj} x_s^{\mathrm{AF}} + n_{sj}, \tag{3.6}$$

with n_{sj} as the AWGN term. Consequently, the end-to-end SINR at node Q via the relay link can be obtained as

$$\gamma_{psq}^{\mathrm{AF}} = \frac{\zeta\gamma_{ps}\beta|h_{sq}|^2}{(1-\zeta)\gamma_{ps}\beta|h_{sq}|^2 + \zeta\beta|h_{sq}|^2 + 1}, \tag{3.7}$$

where $\gamma_{ps} = \eta_p|h_{ps}|^2$ which is same as $\gamma_{ps}^{\mathrm{DL}}$ in (3.4) and used invariably in the subsequent analysis. With the MRC method, node Q can thus combine the two copies of the primary signal, one from the first IT phase (through DLT) and other from the second IT phase (through relay cooperation).

On the other hand, after receiving the superposed NOMA signal at node R, the SR decodes its own signal x_s and discards the primary signal component x_p through SIC operation, while considering the primary component as an interference to the secondary node. For this, SR first decodes the primary signal x_p while treating the secondary signal x_s as noise. Accordingly, the SINR at node R can be given by

$$\gamma_{psr\to x_p}^{\mathrm{AF}} = \frac{\zeta\gamma_{ps}\beta|h_{sr}|^2}{(1-\zeta)\gamma_{ps}\beta|h_{sr}|^2 + \zeta\beta|h_{sr}|^2 + 1}. \tag{3.8}$$

Note that in the first phase of IT, the primary signal x_p has also been received at node R from node P directly. So, the MRC method is employed at node R to combine the received primary signal components in the first and second phases of IT. Thereafter, SR decodes its own signal x_s by eliminating x_p from y_{sr}^{AF}. However, in practice, there may be some decoding errors owing to the imperfection in executing the SIC operation. Accordingly, a residual interference is assumed to exist, leading to an ipSIC term. Thus, after the ipSIC, the end-to-end SINR at node R can be provided as

$$\gamma_{psr}^{\mathrm{AF}} = \frac{(1-\zeta)\gamma_{ps}\beta|h_{sr}|^2}{\zeta\beta|h_{sr}|^2 + \varsigma\zeta\beta\gamma_{ps}|h_R|^2 + 1}, \tag{3.9}$$

where $\varsigma = 0$ and $\varsigma = 1$ imply the respective cases of pSIC and ipSIC, h_R is the residual IS channel coefficient at node R and is subject to Nakagami-m fading [71] with its corresponding fading severity parameter m_R and average channel power gain Ω_R.

DF Relaying

In this relaying strategy, during the second IT phase, node S facilitates the DF-based relaying and makes an effort to decode the primary signal x_p. On successful decoding of the primary signal x_p at node S, it combines x_p with its own signal x_s to generate a superimposed signal x_s^{DF} as per the NOMA principle. Hence, the signal transmitted by node S is given by

$$x_s^{\mathrm{DF}} = \sqrt{\zeta P_s}x_p + \sqrt{(1-\zeta)P_s}x_s. \tag{3.10}$$

Hereafter, the received signal at node j, where $j \in \{q, r\}$, can be expressed as

$$y_{sj} = h_{sj}x_s^{\mathrm{DF}} + n_{sj}. \tag{3.11}$$

Consequently, the resultant SINR expression at node Q, based on (3.10) and (3.11), can be represented as

$$\gamma_{sq}^{\mathrm{DF}} = \frac{\zeta\beta\gamma_{ps}|h_{sq}|^2}{(1-\zeta)\gamma_{ps}\beta|h_{sq}|^2 + 1}. \tag{3.12}$$

Further, based on (3.10) and (3.11), the equivalent SINR at node R to decode the primary signal x_p can be obtained as

$$\gamma_{sr\to x_p}^{\mathrm{DF}} = \frac{\zeta\beta\gamma_{ps}|h_{sr}|^2}{(1-\zeta)\beta\gamma_{ps}|h_{sr}|^2 + 1}. \tag{3.13}$$

Whereas, the resultant SINR at R to decode its own signal x_s can be provided as

$$\gamma_{sr}^{\mathrm{DF}} = \frac{(1-\zeta)\beta\gamma_{ps}|h_{sr}|^2}{\varsigma\beta\zeta\gamma_{ps}|h_R|^2 + 1}. \tag{3.14}$$

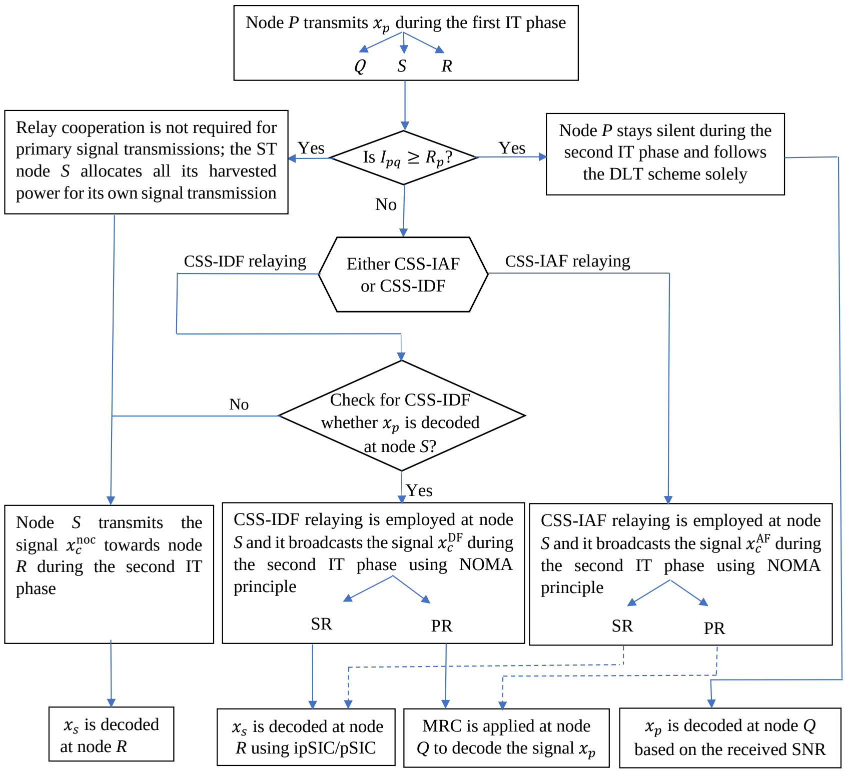

Figure 3.3: Flow chart for the proposed IR protocol.

On the other hand, if node S fails to decode the primary signal x_p in the first IT phase, it will proceed with non-cooperation mode and transmit its own signal only to node R during the second IT phase, whereas, the PR node Q follows only the transmission through DL in the first IT phase.

3.1.4 Proposed IR Protocol

In this protocol, the relaying cooperation is adeptly executed by the ST node S based on the successful or unsuccessful decoding of the primary signal x_p at node Q in the first IT phase. Importantly, the relaying cooperation is invoked depending on the success/failure of the DL ($P \rightarrow Q$) transmission. Consequently, the mutual information of the DLT can be written as

$$\mathcal{I}_{pq} = \log_2 \left(1 + \gamma_{pq}^{\text{DL}}\right). \tag{3.15}$$

If node Q can successfully decode the information signal from node P, i.e., $\mathcal{I}_{pq} \geq R_p$, where R_p is a target threshold rate, it acknowledges the cooperative node S by sending an error-free one-bit feedback[5] that the relaying cooperation is not required.

[5]The feedback/acknowledge time is considered to be small in contrast to the information processing time [72], [73]. It is worth noting that such feedback is transmitted over a separate low-

Accordingly, all the harvested power at node S can be utilized for its own information transmission towards the node R. Therefore, the secondary network's performance can be improved.

For the non-cooperation case (i.e., no relaying required), the signal transmitted by node S can be given as

$$x_s^{\mathrm{noc}} = \sqrt{P_s} x_s. \tag{3.16}$$

Thus, the signal received at node R from S can be expressed as

$$y_{sr}^{\mathrm{noc}} = h_{sr} x_s^{\mathrm{noc}} + n_{sr}. \tag{3.17}$$

Hereby, using (3.16) and (3.17), the resultant SNR expression at node R is given as

$$\gamma_{sr}^{\mathrm{noc}} = \beta \gamma_{ps} |h_{sr}|^2. \tag{3.18}$$

On the contrary, if node Q is unable to decode the information signal from node P in the first IT phase, i.e., if $\mathcal{I}_{pq} < R_p$, it sends a negative feedback to S. Thus, the relaying cooperation from ST is evoked and further IT operation follows either the AF or the DF relaying protocol. However, in the case of DF relaying, if the primary signal x_p could not be decoded at node S after the first IT phase, node S can utilize all its harvested power in transmitting its own information. Hence, the equivalent SNR expression at node R can be given by (3.18).

For the subsequent analysis, we refer the CSS schemes based on IR protocol using AF and DF relaying as CSS-IAF and CSS-IDF, respectively. The proposed IR protocol is depicted as a flowchart in Fig. 3.3.

3.2 Outage Performance of Primary Network

In this section, the expressions for the OP of the primary network are derived under two transmission schemes i.e., DLT and CSS (with IAF and IDF relaying strategies).

To proceed with the analysis, we first present the statistics of the underlying fading channels. As the pertinent links are subject to Nakagami-m fading, the PDF

bandwidth error-free channel, resulting in minimal delay.

and CDF of $|h_{ij}|^2$, for $i \in \{p, s\}$ and $j \in \{q, s, r\}$ with $i \neq j$, can be, respectively, given by

$$f_{|h_{ij}|^2}(x) = \left(\frac{m_{ij}}{\Omega_{ij}}\right)^{m_{ij}} \frac{x^{m_{ij}-1}}{\Gamma(m_{ij})} \mathrm{e}^{-\frac{m_{ij}}{\Omega_{ij}}x} \tag{3.19}$$

and

$$F_{|h_{ij}|^2}(x) = \frac{1}{\Gamma(m_{ij})} \Upsilon\left(m_{ij}, \frac{m_{ij}}{\Omega_{ij}}x\right), \tag{3.20}$$

where Ω_{ij} is the average power and m_{ij} is the fading severity parameter. Hereafter, we consider Nakagami-m channels with integer-valued fading parameters for analytical simplicity. Note that an integer-valued Nakagami-m fading model is widely adopted in literature since, in practice, the measurement accuracy of the underlying channel is typically of integer order [74]. However, the performance analysis can also be taken up for the non-integer case as followed in [75].

3.2.1 DLT Scheme

We consider a DLT scheme which provides communication solely through the DL, i.e., without cooperation of the relay link. Basically, this scheme is examined as a benchmark to compare its performance with the proposed CSS scheme. As such, for a pre-defined target rate R_p, the OP of the primary network using the DLT scheme can be expressed as

$$P_{\text{out}}^{\text{DL}}(R_p) = \Pr\left[\log_2\left(1 + \gamma_{pq}^{\text{DL}}\right) < R_p\right], \tag{3.21}$$

which can be re-expressed as

$$P_{\text{out}}^{\text{DL}}(R_p) = \Pr\left[\gamma_{pq}^{\text{DL}} < \gamma_p'\right] = F_{\gamma_{pq}^{\text{DL}}}(\gamma_p'), \tag{3.22}$$

where $\gamma_p' = 2^{R_p} - 1$. Now, (3.22) requires the evaluation of the CDF $F_{\gamma_{pq}^{\text{DL}}}(\gamma_p')$, which can be obtained using (3.20) as

$$F_{\gamma_{pq}^{\text{DL}}}(\gamma_p') = \frac{1}{\Gamma(m_{pq})} \Upsilon\left(m_{pq}, \frac{m_{pq}}{\Omega_{pq}\eta_p}\gamma_p'\right). \tag{3.23}$$

3.2.2 CSS Scheme

Herein, we appraise the outage performance of the primary network for the considered EH-OCNOMA with the CSS-IAF and CSS-IDF schemes as described in Section 3.1.

CSS with IAF Relaying (CSS-IAF)

For a given target rate R_p, the OP of the primary network for CSS-IAF scheme can be formulated as

$$P_{\text{out}}^{\text{AF}}(R_p) = \Pr\left[\gamma_{pq}^{\text{DL}} < \gamma'_p, \gamma_{pq}^{\text{DL}} + \gamma_{psq}^{\text{AF}} < \gamma_p\right], \tag{3.24}$$

where $\gamma_p = 2^{\frac{2R_p}{1-\alpha}} - 1$. Further, $P_{\text{out}}^{\text{AF}}(R_p)$ in (3.24) can be expressed as

$$\begin{aligned} P_{\text{out}}^{\text{AF}}(R_p) &= \Pr\left[\gamma_{pq}^{\text{DL}} < \min(\gamma_p - \gamma_{psq}^{\text{AF}}, \ \gamma'_p)\right] \\ &= \underbrace{\Pr\left[\gamma_{pq}^{\text{DL}} < \gamma'_p, \ \gamma'_p < \gamma_p - \gamma_{psq}^{\text{AF}}\right]}_{I_1} + \underbrace{\Pr\left[\gamma_{pq}^{\text{DL}} < \gamma_p - \gamma_{psq}^{\text{AF}}, \ \gamma'_p \geq \gamma_p - \gamma_{psq}^{\text{AF}}\right]}_{I_2}. \end{aligned} \tag{3.25}$$

To derive the OP expression in (3.25), we have to evaluate the two probability terms I_1 and I_2. Hereby, we first evaluate the probability term I_1 as

$$\begin{aligned} I_1 &= \Pr\left[\gamma_{pq}^{\text{DL}} < \gamma'_p, \ \gamma_{psq}^{\text{AF}} < \gamma_p - \gamma'_p\right] \\ &= F_{\gamma_{pq}^{\text{DL}}}(\gamma'_p)\, F_{\gamma_{psq}^{\text{AF}}}(\gamma_p - \gamma'_p), \end{aligned} \tag{3.26}$$

where the multiplication of individual CDF terms results from the statistical independence between the two events. Now, (3.26) requires the evaluation of $F_{\gamma_{psq}^{\text{AF}}}(\gamma_p - \gamma'_p)$, which can be derived as follows in Theorem 1.

Theorem 1. *The CDF $F_{\gamma_{psq}^{AF}}(x)$ under Nakagami-m fading can be given by*

$$F_{\gamma_{psq}^{AF}}(x) = \begin{cases} 1, & \text{if } x \geq \frac{\zeta}{1-\zeta}, \\ \phi_1(x), & \text{if } x < \frac{\zeta}{1-\zeta}, \end{cases} \tag{3.27}$$

where $\phi_1(x)$ is given as

$$\phi_1(x)=1-\sum_{\mathrm{k}=0}^{\mathrm{m}_{ps}-1}\sum_{j=0}^{\mathrm{k}}\frac{2}{\mathrm{k}!}\left(\frac{T_0x}{\theta_x}\right)^k e^{-\left(\frac{T_0x\zeta\beta}{\theta_x}\right)}\left(\frac{\mathrm{m}_{sq}}{\Omega_{sq}}\right)^{\mathrm{m}_{sq}}\frac{1}{\Gamma(\mathrm{m}_{sq})}\binom{\mathrm{k}}{j}(\zeta\beta)^j$$
$$\times\left(\frac{T_0x\Omega_{sq}}{\theta_x\mathrm{m}_{sq}}\right)^{\frac{\mathrm{m}_{sq}+j-k}{2}}\mathcal{K}_{\mathrm{m}_{sq}+j-k}\left(2\sqrt{\frac{T_0x\mathrm{m}_{sq}}{\theta_x\Omega_{sq}}}\right), \tag{3.28}$$

with $T_0=\frac{\mathrm{m}_{ps}}{\Omega_{ps}\eta_p\beta}$ and $\theta_x=\zeta-(1-\zeta)x$.

Proof. See Appendix C. ■

It is noteworthy that the condition $x<\frac{\zeta}{1-\zeta}$ in (3.27) makes the CSS effective through the IAF relaying scheme, otherwise the value of the CDF $F_{\gamma_{psq}^{\mathrm{AF}}}(x)$ becomes unity. This phenomenon is referred to as relay cooperation ceiling (RCC), and hereby, the primary communication solely follows the DLT scheme. By substituting (3.23) and (3.27) (with $x=\gamma_p-\gamma_p'$) into (3.26), one can obtain I_1.

Next, we evaluate the probability term I_2 as

$$\begin{aligned}I_2&=\Pr\left[\gamma_{psq}^{\mathrm{AF}}<\gamma_p-\gamma_{pq}^{\mathrm{DL}},\ \gamma_{psq}^{\mathrm{AF}}\geq\gamma_p-\gamma_p')\right]\\&=\int_{\gamma_p-\gamma_p'}^{\gamma_p-y}\int_0^{\gamma_p}f_{\gamma_{psq}^{\mathrm{AF}}}(x)f_{\gamma_{pq}^{\mathrm{DL}}}(y)dxdy\\&=\int_0^{\gamma_p}F_{\gamma_{psq}^{\mathrm{AF}}}(\gamma_p-y)f_{\gamma_{pq}^{\mathrm{DL}}}(y)dy-\int_0^{\gamma_p}F_{\gamma_{psq}^{\mathrm{AF}}}(\gamma_p-\gamma_p')f_{\gamma_{pq}^{\mathrm{DL}}}(y)dy.\end{aligned} \tag{3.29}$$

Using the CDF $F_{\gamma_{psq}^{\mathrm{AF}}}(x)$ into (3.29), it is intricate to get a closed-form solution for I_2. Hence, by applying an M-step staircase approximation approach [76] for the involved triangular integral region in (3.29), I_2 can be expressed as

$$\begin{aligned}I_2\approx&\sum_{i=0}^{M-1}\left\{F_{\gamma_{pq}^{\mathrm{DL}}}\left(\frac{i+1}{M}\gamma_p\right)-F_{\gamma_{pq}^{\mathrm{DL}}}\left(\frac{i}{M}\gamma_p\right)\right\}F_{\gamma_{psq}^{\mathrm{AF}}}\left(\frac{M-i}{M}\gamma_p\right)\\&-F_{\gamma_{psq}^{\mathrm{AF}}}(\gamma_p-\gamma_p')F_{\gamma_{pq}^{\mathrm{DL}}}(\gamma_p).\end{aligned} \tag{3.30}$$

Finally, after inserting the expressions of I_1 and I_2 into (3.25), the analytical expression of $P_{\mathrm{out}}^{\mathrm{AF}}(R_p)$ can be obtained. As such, relying on the conditions on the threshold γ_p using (3.27), $P_{\mathrm{out}}^{\mathrm{AF}}(R_p)$ can be expressed for the following cases:

- When $\gamma_p<\frac{\zeta}{1-\zeta}$,

$$\begin{aligned} P_{\text{out}}^{\text{AF}}(R_p) \triangleq P_1(R_p) &= F_{\gamma_{pq}^{\text{DL}}}(\gamma_p')\, F_{\gamma_{psq}^{\text{AF}}}(\gamma_p - \gamma_p') \\ &+ \sum_{i=0}^{M-1} \left\{ F_{\gamma_{pq}^{\text{DL}}}\left(\frac{i+1}{M}\gamma_p\right) - F_{\gamma_{pq}^{\text{DL}}}\left(\frac{i}{M}\gamma_p\right) \right\} F_{\gamma_{psq}^{\text{AF}}}\left(\frac{M-i}{M}\gamma_p\right) \\ &- F_{\gamma_{psq}^{\text{AF}}}(\gamma_p - \gamma_p') F_{\gamma_{pq}^{\text{DL}}}(\gamma_p). \end{aligned} \tag{3.31}$$

- When $\frac{\zeta}{1-\zeta} \leq \gamma_p < \frac{\zeta}{1-\zeta} + \gamma_p'$,

$$\begin{aligned} P_{\text{out}}^{\text{AF}}(R_p) \triangleq P_2(R_p) &= F_{\gamma_{pq}^{\text{DL}}}(\gamma_p')\, F_{\gamma_{psq}^{\text{AF}}}(\gamma_p - \gamma_p') \\ &+ \sum_{i=0}^{M-1} \left\{ F_{\gamma_{pq}^{\text{DL}}}\left(\frac{i+1}{M}\gamma_p\right) - F_{\gamma_{pq}^{\text{DL}}}\left(\frac{i}{M}\gamma_p\right) \right\} - F_{\gamma_{psq}^{\text{AF}}}(\gamma_p - \gamma_p') F_{\gamma_{pq}^{\text{DL}}}(\gamma_p). \end{aligned} \tag{3.32}$$

- When $\gamma_p \geq \frac{\zeta}{1-\zeta} + \gamma_p'$,

$$\begin{aligned} P_{\text{out}}^{\text{AF}}(R_p) \triangleq P_3(R_p) &= F_{\gamma_{pq}^{\text{DL}}}(\gamma_p') - F_{\gamma_{pq}^{\text{DL}}}(\gamma_p) \\ &+ \sum_{i=0}^{M-1} \left\{ F_{\gamma_{pq}^{\text{DL}}}\left(\frac{i+1}{M}\gamma_p\right) - F_{\gamma_{pq}^{\text{DL}}}\left(\frac{i}{M}\gamma_p\right) \right\}. \end{aligned} \tag{3.33}$$

Hereby, depending on the above cases, the OP of the primary network for CSS-IAF scheme can be expressed as

$$P_{\text{out}}^{\text{AF}}(R_p) = \begin{cases} P_1(R_p), & \text{if } \gamma_p < \frac{\zeta}{1-\zeta}, \\ P_2(R_p), & \text{if } \frac{\zeta}{1-\zeta} \leq \gamma_p < \frac{\zeta}{1-\zeta} + \gamma_p', \\ P_3(R_p), & \text{if } \gamma_p \geq \frac{\zeta}{1-\zeta} + \gamma_p'. \end{cases} \tag{3.34}$$

Remarks: The M-step staircase approximation method is a numerical technique used to approximate a function by dividing the domain into a series of equal-length subintervals and constructing a triangular region over each subinterval. The height of each triangle is set to the average value of the function over the subinterval, and the area of the triangle is calculated as the product of the height and the width of the subinterval. By summing the areas of all the triangles, an approximation to the integral of the function over the entire domain can be obtained. This method is useful for approximating piecewise linear functions but may not be accurate for functions with significant curvature or nonlinearity. A suitable value for M can be chosen to ensure that the convergence error is minimized. Thus, for all of the analytical curves shown in Section 3.5, we assume M = 50.

CSS with IDF Relaying (CSS-IDF)

Considering a target rate R_p, the OP of the primary network for CSS-IDF scheme can be expressed as

$$P_{\text{out}}^{\text{DF}}\left(R_p\right) = \Pr\left[\gamma_{pq}^{\text{DL}} < \gamma_p', \gamma_{ps}^{\text{DL}} < \gamma_p\right] + \Pr\left[\gamma_{pq}^{\text{DL}} < \gamma_p', \gamma_{ps}^{\text{DL}} \geq \gamma_p, \gamma_{pq}^{\text{DL}} + \gamma_{sq}^{\text{DF}} < \gamma_p\right], \tag{3.35}$$

which can be further written as

$$P_{\text{out}}^{\text{DF}}\left(R_p\right) = \underbrace{F_{\gamma_{pq}^{\text{DL}}}(\gamma_p') F_{\gamma_{ps}^{\text{DL}}}(\gamma_p)}_{I_3} + \underbrace{\bar{F}_{\gamma_{ps}^{\text{DL}}}(\gamma_p) \Pr\left[\gamma_{pq}^{\text{DL}} < \gamma_p', \gamma_{pq}^{\text{DL}} + \gamma_{sq}^{\text{DF}} < \gamma_p\right]}_{I_4}, \tag{3.36}$$

where $\bar{F}_{\gamma_{ps}^{\text{DL}}}(\cdot) = 1 - F_{\gamma_{ps}^{\text{DL}}}(\cdot)$ represents the complementary CDF. Hereby, to solve (3.36), it requires the assessment of the probability terms I_3 and I_4. To evaluate I_3, it further requires the CDFs $F_{\gamma_{pq}^{\text{DL}}}(\gamma_p')$ and $F_{\gamma_{ps}^{\text{DL}}}(\gamma_p)$, which can be deduced while accompanied by the steps as in Sec. 3.2.1. However, I_4 can be computed in a similar fashion to (3.25), and is obtained as

$$\begin{aligned} I_4 &\approx \Pr\left[\gamma_{pq}^{\text{DL}} < \min(\gamma_p - \gamma_{sq}^{\text{DF}}, \gamma_p')\right] \bar{F}_{\gamma_{ps}^{\text{DL}}}(\gamma_p) \\ &= \Bigg[F_{\gamma_{pq}^{\text{DL}}}(\gamma_p') F_{\gamma_{sq}^{\text{DF}}}(\gamma_p - \gamma_p') + \sum_{i=0}^{M-1} \left\{ F_{\gamma_{pq}^{\text{DL}}}\left(\frac{i+1}{M}\gamma_p\right) - F_{\gamma_{pq}^{\text{DL}}}\left(\frac{i}{M}\gamma_p\right) \right\} \\ &\qquad \times F_{\gamma_{sq}^{\text{DF}}}\left(\frac{M-i}{M}\gamma_p\right) \Bigg] \bar{F}_{\gamma_{ps}^{\text{DL}}}(\gamma_p). \end{aligned} \tag{3.37}$$

To simplify (3.37), we need to find the CDF $F_{\gamma_{sq}^{\text{DF}}}(\gamma_p - \gamma_p')$, which can be derived as in the following lemma.

Lemma 1. *The CDF $F_{\gamma_{sq}^{DF}}(x)$ under Nakagami-m fading can be deduced as*

$$F_{\gamma_{sq}^{DF}}(x) = \begin{cases} 1, & \text{if } x \geq \frac{\zeta}{1-\zeta}, \\ \phi_2(x), & \text{if } x < \frac{\zeta}{1-\zeta}, \end{cases} \tag{3.38}$$

where $\phi_2(x)$ is given as

$$\phi_2(x) = 1 - \sum_{\text{k}=0}^{\text{m}_{ps}-1} \frac{2}{\text{k}!} \left(\frac{T_0 x}{\theta_x}\right)^k \left(\frac{\text{m}_{sq}}{\Omega_{sq}}\right)^{\text{m}_{sq}} \frac{1}{\Gamma(\text{m}_{sq})} \left(\frac{T_0 x \Omega_{sq}}{\theta_x \text{m}_{sq}}\right)^{\frac{\text{m}_{sq}-k}{2}} \mathcal{K}_{\text{m}_{sq}-k}\left(2\sqrt{\frac{T_0 x \text{m}_{sq}}{\theta_x \Omega_{sq}}}\right). \tag{3.39}$$

Proof. Following the analogous steps as used in deriving (3.27) in Appendix C with (3.12), one can assess the result in (3.38). ∎

By substituting the CDFs $F_{\gamma_{sq}^{\mathrm{DF}}}(x)$, $F_{\gamma_{pq}^{\mathrm{DL}}}(x)$, and $\bar{F}_{\gamma_{ps}^{\mathrm{DL}}}(x)$ into (3.37), I_4 can be obtained. Finally, after using the expressions for I_3 and I_4 into (3.36), and applying the conditions on threshold γ_p with the help of (3.38), $P_{\mathrm{out}}^{\mathrm{DF}}(R_p)$ can be expressed for the following cases:

- When $\gamma_p < \frac{\zeta}{1-\zeta}$,

$$
\begin{aligned}
&P_{\mathrm{out}}^{\mathrm{DF}}(R_p) \triangleq P_4(R_p) \\
&= \left[F_{\gamma_{pq}^{\mathrm{DL}}}(\gamma_p') F_{\gamma_{sq}^{\mathrm{DF}}}(\gamma_p - \gamma_p') + \sum_{i=0}^{M-1} \left\{ F_{\gamma_{pq}^{\mathrm{DL}}}\left(\frac{i+1}{M}\gamma_p\right) - F_{\gamma_{pq}^{\mathrm{DL}}}\left(\frac{i}{M}\gamma_p\right) \right\} \right. \\
&\left. \times F_{\gamma_{sq}^{\mathrm{DF}}}\left(\frac{M-i}{M}\gamma_p\right) \right] \bar{F}_{\gamma_{ps}^{\mathrm{DL}}}(\gamma_p) + F_{\gamma_{pq}^{\mathrm{DL}}}(\gamma_p') F_{\gamma_{ps}^{\mathrm{DL}}}(\gamma_p).
\end{aligned} \tag{3.40}
$$

- When $\frac{\zeta}{1-\zeta} \leq \gamma_p < \frac{\zeta}{1-\zeta} + \gamma_p'$,

$$
\begin{aligned}
&P_{\mathrm{out}}^{\mathrm{DF}}(R_p) \triangleq P_5(R_p) \\
&= \left[F_{\gamma_{pq}^{\mathrm{DL}}}(\gamma_p') F_{\gamma_{sq}^{\mathrm{DF}}}(\gamma_p - \gamma_p') + \sum_{i=0}^{M-1} \left\{ F_{\gamma_{pq}^{\mathrm{DL}}}\left(\frac{i+1}{M}\gamma_p\right) - F_{\gamma_{pq}^{\mathrm{DL}}}\left(\frac{i}{M}\gamma_p\right) \right\} \right] \\
&\times \bar{F}_{\gamma_{ps}^{\mathrm{DL}}}(\gamma_p) + F_{\gamma_{pq}^{\mathrm{DL}}}(\gamma_p') F_{\gamma_{ps}^{\mathrm{DL}}}(\gamma_p).
\end{aligned} \tag{3.41}
$$

- When $\gamma_p \geq \frac{\zeta}{1-\zeta} + \gamma_p'$,

$$
\begin{aligned}
&P_{\mathrm{out}}^{\mathrm{DF}}(R_p) \triangleq P_6(R_p) \\
&= \left[F_{\gamma_{pq}^{\mathrm{DL}}}(\gamma_p') + \sum_{i=0}^{M-1} \left\{ F_{\gamma_{pq}^{\mathrm{DL}}}\left(\frac{i+1}{M}\gamma_p\right) - F_{\gamma_{pq}^{\mathrm{DL}}}\left(\frac{i}{M}\gamma_p\right) \right\} \right] \bar{F}_{\gamma_{ps}^{\mathrm{DL}}}(\gamma_p) \\
&+ F_{\gamma_{pq}^{\mathrm{DL}}}(\gamma_p') F_{\gamma_{ps}^{\mathrm{DL}}}(\gamma_p).
\end{aligned} \tag{3.42}
$$

Thus, depending on the above cases, the OP of the primary network for the CSS-IDF scheme can be expressed as

$$P_{\text{out}}^{\text{DF}}(R_p) = \begin{cases} P_4(R_p), & \text{if } \gamma_p < \frac{\zeta}{1-\zeta}, \\ P_5(R_p), & \text{if } \frac{\zeta}{1-\zeta} \leq \gamma_p < \frac{\zeta}{1-\zeta} + \gamma_p', \\ P_6(R_p), & \text{if } \gamma_p \geq \frac{\zeta}{1-\zeta} + \gamma_p'. \end{cases} \tag{3.43}$$

Remark 1: Referring to (3.34) and (3.43), it can be observed that the proposed CSS-IAF and CSS-IDF schemes are effective, when $\gamma_p < \frac{\zeta}{1-\zeta}+\gamma_p'$. Once $\gamma_p \geq \frac{\zeta}{1-\zeta}+\gamma_p'$, the RCC effect occurs, and hereby, the performance of the primary network solely depends on the DLT scheme. On the contrary, for the FR-based AF and DF relaying schemes, this RCC effect occurs once $\gamma_p \geq \frac{\zeta}{1-\zeta}$. Hence, the proposed IR-based schemes can support relatively higher data rate than the FR-based schemes till the occurrence of RCC effect. This implication is illustrated later in the Results and Discussion section.

3.2.3 NOMA-Based Power Allocation Parameter

In order to accomplish the QoS criterion for the primary network, the NOMA power allocation strategy at relay node S must be developed. Herein, we choose the effective value of the NOMA-based power allocation parameter ζ such that the OP of primary network for CSS scheme lies below or equal to that for DLT scheme. From (3.34) and (3.43), referring the condition $\gamma_p < \frac{\zeta}{1-\zeta} + \gamma_p'$, the permissible range of ζ under the CSS-IAF and CSS-IDF schemes for a given threshold γ_p can be calculated as

$$\frac{\gamma_p - \gamma_p'}{1 + \gamma_p - \gamma_p'} < \zeta < 1. \tag{3.44}$$

Consequently, the effective value of ζ can be evaluated for a given target rate R_p under the CSS-IAF and CSS-IDF schemes based on the respective conditions

$$P_{\text{out}}^{\text{AF}}(R_p) \leq P_{\text{out}}^{\text{DL}}(R_p) \tag{3.45}$$

and

$$P_{\text{out}}^{\text{DF}}(R_p) \leq P_{\text{out}}^{\text{DL}}(R_p). \tag{3.46}$$

Note that a lower value of ζ can allocate more power to the secondary communication, resulting in better CSS possibilities. Since the PR is a high-priority NOMA recipient, a higher value of ζ is assigned to the PR.

3.3 Outage Performance of Secondary Network

This section provides the OP expression for the secondary network under both the CSS-IAF and CSS-IDF schemes while considering the two cases of SIC i.e., ipSIC and pSIC.

3.3.1 CSS-IAF Scheme

Considering a target rate R_s, the OP of the secondary network for the CSS-IAF scheme can be expressed as

$$\begin{aligned} P_{\text{out}}^{\text{AF}}\left(R_s\right) = &\Pr\left[\gamma_{pq}^{\text{DL}} \geq \gamma_p', \gamma_{sr}^{\text{noc}} < \gamma_s\right] \\ &+ \Pr\left[\gamma_{pq}^{\text{DL}} < \gamma_p', \gamma_{psr}^{\text{AF}} < \gamma_s\right], \end{aligned} \tag{3.47}$$

where $\gamma_s = 2^{\frac{2R_s}{1-\alpha}} - 1$. Further, $P_{\text{out}}^{\text{AF}}\left(R_s\right)$ in (3.47) can be expressed as

$$P_{\text{out}}^{\text{AF}}\left(R_s\right) = \bar{F}_{\gamma_{pq}^{\text{DL}}}\left(\gamma_p'\right) F_{\gamma_{sr}^{\text{noc}}}(\gamma_s) + F_{\gamma_{pq}^{\text{DL}}}(\gamma_p') F_{\gamma_{psr}^{\text{AF}}}(\gamma_s). \tag{3.48}$$

As discussed, we evaluate the $F_{\gamma_{psr}^{\text{AF}}}(\gamma_s)$ for the ipSIC and pSIC cases as given in the subsequent subsections.

ipSIC

Hereby, $F_{\gamma_{psr}^{\text{AF}}}\left(\gamma_s\right)$ in (3.48) can be obtained for the case of ipSIC as given in the following theorem.

Theorem 2. *The CDF $F_{\gamma_{psr}^{AF}}\left(\gamma_s\right)$ for the case of ipSIC in CSS-IAF scheme for EH-OCNOMA system under Nakagami-m fading can be given by*

$$F_{\gamma_{psr}^{AF}}\left(\gamma_s\right) = \Psi_1(\gamma_s) - \Psi_2(\gamma_s), \tag{3.49}$$

where $\Psi_1(\gamma_s)$ and $\Psi_2(\gamma_s)$ are given as

$$\Psi_1(\gamma_s) = \sum_{k=0}^{\mathrm{m}_{sr}-1} \frac{(T_2\zeta)^k}{k!} \frac{1}{\Gamma(\mathrm{m}_R)} \left(\frac{\mathrm{m}_R}{\Omega_R}\right)^{\mathrm{m}_R} (k + \mathrm{m}_R - 1)! \left(T_2\zeta + \frac{\mathrm{m}_R}{\Omega_R}\right)^{-(k+\mathrm{m}_R)}, \tag{3.50}$$

$$\Psi_2(\gamma_s) = \sum_{\mathrm{k}=0}^{\mathrm{m}_{ps}-1} \sum_{j=0}^{\mathrm{k}} \sum_{m=0}^{j+\mathrm{m}_{sr}-1} \sum_{v=0}^{j+\mathrm{m}_R+\mathrm{m}_{sr}-2-m} \frac{2(T_0\gamma_s)^{\mathrm{k}}}{\mathrm{k}!} \frac{1}{\Gamma(\mathrm{m}_{sr})} \left(\frac{\mathrm{m}_{sr}}{\Omega_{sr}}\right)^{\mathrm{m}_{sr}} \frac{1}{\Gamma(\mathrm{m}_R)}$$
$$\times \left(\frac{\mathrm{m}_R}{\Omega_R}\right)^{\mathrm{m}_R} \binom{\mathrm{k}}{j} (\zeta\beta)^j \binom{j+\mathrm{m}_{sr}-1}{m} (\zeta\gamma_s)^{j+\mathrm{m}_{sr}-1-m} e^{\left(\frac{T_2T_1}{\zeta\beta\gamma_s} - \frac{T_0\gamma_s\zeta\beta}{T_1} + T_3\right)}$$
$$\times \binom{j+\mathrm{m}_{sr}+\mathrm{m}_R-2-\mathrm{m}}{v} \left(\frac{T_1}{\zeta^2\beta\gamma_s}\right)^{j+\mathrm{m}_R+\mathrm{m}_{sr}-1-m} \left(\frac{T_0\gamma_s T_1\Omega_{sr}}{\mathrm{m}_{sr}}\right)^{\frac{\mathrm{m}+1-k}{2}}$$
$$\times (-1)^{j+\mathrm{m}_R+\mathrm{m}_{sr}-2-m-v} \left(\frac{1}{T_1}\right)^{j+\mathrm{m}_{sr}} \int_1^\infty \theta^{\frac{m+2v+1-k}{2}} e^{-\left(\frac{T_2T_1\theta}{\zeta^2\beta\gamma_s} + T_3\theta\right)}$$
$$\times \mathcal{K}_{\mathrm{m}-k+1}\left(2\sqrt{\frac{\mathrm{m}_{sr}T_0\gamma_s\theta}{\Omega_{sr}T_1}}\right) d\theta, \tag{3.51}$$

with $T_1 = (1-\zeta)$, $T_2 = \frac{\mathrm{m}_{sr}\gamma_s}{\Omega_{sr}T_1}$, *and* $T_3 = \frac{\mathrm{m}_R T_1}{\Omega_R\zeta^2\beta\gamma_s}$.

Proof. See Appendix D. ■

Although the expression in (3.51) is presented in a one-integral form, it can be efficiently computed using symbolic software like Mathematica or Maple and consumes much less time than the computer simulation approach.

pSIC

For the pSIC case, the $F_{\gamma_{psr}^{\mathrm{AF}}}(\gamma_s)$ can be evaluated as in the following lemma.

Lemma 2. *The CDF* $F_{\gamma_{psr}^{AF}}(\gamma_s)$ *for the case of pSIC under Nakagami-m fading can be given by*

$$F_{\gamma_{psr}^{AF}}(\gamma_s) = 1 - 2\sum_{\mathrm{k}=0}^{\mathrm{m}_{ps}-1} \sum_{j=0}^{\mathrm{k}} \left(\frac{T_0\gamma_s}{T_1}\right)^{\mathrm{k}} \frac{1}{\mathrm{k}!} e^{\frac{-T_0\gamma_s\zeta\beta}{T_1}} \binom{\mathrm{k}}{j} (\zeta\beta)^j \frac{1}{\Gamma(\mathrm{m}_{sr})} \left(\frac{\mathrm{m}_{sr}}{\Omega_{sr}}\right)^{\mathrm{m}_{sr}}$$
$$\times \left(\frac{T_0\gamma_s\Omega_{sr}}{T_1\mathrm{m}_{sr}}\right)^{\frac{j-k+\mathrm{m}_{sr}}{2}} \mathcal{K}_{j-k+\mathrm{m}_{sr}}\left(2\sqrt{\frac{T_0\gamma_s\mathrm{m}_{sr}}{T_1\Omega_{sr}}}\right). \tag{3.52}$$

Proof. By adopting the similar steps as followed for (3.49) in Appendix D, one can get the result in (3.52). ■

Next, $F_{\gamma_{sr}^{\mathrm{noc}}}(\gamma_s)$ can be obtained using (3.18) with the help of following lemma as follows:

Lemma 3. *The CDF $F_{\gamma_{sr}^{noc}}(\gamma_s)$ for the no cooperation case under Nakagami-m fading can be given by*

$$F_{\gamma_{sr}^{noc}}(\gamma_s) = 1 - 2\sum_{\mathrm{k}=0}^{\mathrm{m}_{ps}-1} \frac{2(T_0\gamma_s)^k}{\mathrm{k}!}\frac{1}{\Gamma(\mathrm{m}_{sr})}\left(\frac{\mathrm{m}_{sr}}{\Omega_{sr}}\right)^{\mathrm{m}_{sr}} \times \left(\frac{T_0\gamma_s\Omega_{sr}}{\mathrm{m}_{sr}}\right)^{\frac{\mathrm{m}_{sr}-k}{2}} \mathcal{K}_{\mathrm{m}_{sr}-k}\left(2\sqrt{\frac{T_0\gamma_s\mathrm{m}_{sr}}{\Omega_{sr}}}\right). \tag{3.53}$$

Proof. See Appendix E. ■

Hereby, the desired OP for the cases of ipSIC and pSIC can be evaluated by substituting the involved CDF expressions in (3.48).

3.3.2 CSS-IDF Scheme

Considering a target rate R_s, the OP of the secondary network for the CSS-IDF scheme can be expressed as

$$P_{\mathrm{out}}^{\mathrm{DF}}(R_s) = \Pr\left[\gamma_{pq}^{\mathrm{DL}} \geq \gamma_p', \gamma_{sr}^{\mathrm{noc}} < \gamma_s\right] + \Pr\left[\gamma_{pq}^{\mathrm{DL}} < \gamma_p', \gamma_{ps}^{\mathrm{DL}} < \gamma_p, \gamma_{sr}^{\mathrm{noc}} < \gamma_s\right] + \Pr\left[\gamma_{pq}^{\mathrm{DL}} < \gamma_p', \gamma_{ps}^{\mathrm{DL}} \geq \gamma_p, \gamma_{sr}^{\mathrm{DF}} < \gamma_s\right], \tag{3.54}$$

which can be further expressed as

$$P_{\mathrm{out}}^{\mathrm{DF}}(R_s) = \bar{F}_{\gamma_{pq}^{\mathrm{DL}}}(\gamma_p')F_{\gamma_{sr}^{\mathrm{noc}}}(\gamma_s) + F_{\gamma_{pq}^{\mathrm{DL}}}(\gamma_p')\underbrace{\Pr\left[\gamma_{ps}^{\mathrm{DL}} < \gamma_p,\ \gamma_{sr}^{\mathrm{noc}} < \gamma_s\right]}_{P_1} + F_{\gamma_{pq}^{\mathrm{DL}}}(\gamma_p')\underbrace{\Pr\left[\gamma_{ps}^{\mathrm{DL}} \geq \gamma_p, \gamma_{sr}^{\mathrm{DF}} < \gamma_s\right]}_{P_2}. \tag{3.55}$$

As such, (3.55) requires the evaluation of the two probability terms P_1 and P_2. Hereby, we first evaluate the probability term P_1 as

$$P_1 = \Pr\left[\gamma_{ps}^{\mathrm{DL}} < \gamma_p,\ \gamma_{sr}^{\mathrm{noc}} < \gamma_s\right], \tag{3.56}$$

which can be re-expressed using (3.18) as

$$
\begin{aligned}
P_1 &= \Pr\left[\gamma_{ps}^{\mathrm{DL}} < \gamma_p,\ \beta\gamma_{ps}|h_{sr}|^2 < \gamma_s\right] \\
&= \Pr\left[\gamma_{ps}^{\mathrm{DL}} < \min\left(\gamma_p,\ \frac{\gamma_s}{\beta|h_{sr}|^2}\right)\right] \\
&= \underbrace{\Pr\left[\gamma_{ps}^{\mathrm{DL}} < \gamma_p,\ \gamma_p < \frac{\gamma_s}{\beta|h_{sr}|^2}\right]}_{P_{11}} + \underbrace{\Pr\left[\gamma_{ps}^{\mathrm{DL}} < \frac{\gamma_s}{\beta|h_{sr}|^2},\ \gamma_p \geq \frac{\gamma_s}{\beta|h_{sr}|^2}\right]}_{P_{12}},
\end{aligned}
\tag{3.57}
$$

where P_{11} can be given as

$$
P_{11} = F_{\gamma_{ps}^{\mathrm{DL}}}(\gamma_p) F_{|h_{sr}|^2}\left(\frac{\gamma_s}{\beta\gamma_p}\right). \tag{3.58}
$$

To evaluate P_{11}, we require the CDFs $F_{\gamma_{ps}^{\mathrm{DL}}}(\gamma_p)$ and $F_{|h_{sr}|^2}(\frac{\gamma_s}{\beta\gamma_p})$, which can be obtained readily using (3.20). Now, the next probability term P_{12} in (3.57) can be computed through the following lemma.

Lemma 4. *The probability term P_{12} in (3.57) can be expressed under Nakagami-m fading as*

$$
\begin{aligned}
P_{12} = \sum_{k=0}^{\mathrm{m}_{sr}-1} \frac{1}{k!}&\left(\left(\frac{T_2T_1}{\beta\gamma_p}\right)^k e^{\left(-\frac{T_2T_1}{\beta\gamma_p}\right)} - 2\left(\frac{T_1T_2}{\eta_p}\right)^{\mathrm{k}}\left(\frac{\mathrm{m}_{ps}}{\Omega_{ps}}\right)^{\mathrm{m}_{ps}}\right. \\
&\left.\times \frac{1}{\Gamma(\mathrm{m}_{ps})}\left(\frac{T_1T_2\Omega_{ps}}{\eta_p\mathrm{m}_{ps}}\right)^{\frac{\mathrm{m}_{ps}-k}{2}} \mathcal{K}_{\mathrm{m}_{ps}-k}\left(2\sqrt{\frac{T_1T_2\mathrm{m}_{ps}}{\eta_p\Omega_{ps}}}\right)\right).
\end{aligned}
\tag{3.59}
$$

Proof. See Appendix F ■

Next, we evaluate the other probability term P_2 in (3.55) for the ipSIC and pSIC cases in the sequel.

ipSIC

For this case, we proceed with the analysis using the following lemma.

Lemma 5. *The probability term P_2 in (3.55) for the ipSIC case under Nakagami-m fading can be given as*

$$
P_2 = \bar{F}_{\gamma_{ps}^{DL}}(\gamma_p) P_{21} - P_{22}, \tag{3.60}
$$

where P_{21} and P_{22} are given by

$$P_{21} = \sum_{k=0}^{\mathrm{m}_{sr}-1} \frac{(T_2\zeta)^k}{k!} \frac{1}{\Gamma(\mathrm{m}_R)} \left(\frac{\mathrm{m}_R}{\Omega_R}\right)^{\mathrm{m}_R} (k+\mathrm{m}_R-1)! \left(T_2\zeta + \frac{\mathrm{m}_R}{\Omega_R}\right)^{-(k+\mathrm{m}_R)},$$

$$P_{22} = \sum_{\mathrm{k}=0}^{\mathrm{m}_{ps}-1} \sum_{j=0}^{\mathrm{m}_{sr}-1} \frac{2(T_0\gamma_s)^{\mathrm{k}}}{\mathrm{k}!} \frac{1}{\Gamma(\mathrm{m}_{sr})} \left(\frac{\mathrm{m}_{sr}}{\Omega_{sr}T_1}\right)^{\mathrm{m}_{sr}} \binom{\mathrm{m}_{sr}-1}{j} (\zeta\gamma_s)^j$$
$$\times \frac{1}{\Gamma(\mathrm{m}_R)} \left(\frac{\mathrm{m}_R}{\Omega_R}\right)^{\mathrm{m}_R} \left(\frac{T_0\gamma_s T_1 \Omega_{sr}}{\mathrm{m}_{sr}}\right)^{\frac{\mathrm{m}_{sr}-j-k}{2}} \mathcal{K}_{\mathrm{m}_{sr}-j-k}\left(2\sqrt{\frac{\mathrm{m}_{sr}T_0\gamma_s}{\Omega_{sr}T_1}}\right)$$
$$\times (\mathrm{m}_R+j-1)! \left(T_2\zeta + \frac{\mathrm{m}_R}{\Omega_R}\right)^{-(\mathrm{m}_R+j)}. \tag{3.61}$$

Proof. By adopting the similar procedure used for the derivation of (3.59) in Appendix F, one can get the result in (3.60). ■

pSIC

For the pSIC case, the analysis can be conducted further with the aid of following lemma.

Lemma 6. *For the pSIC case, the probability term P_2 in (3.55) can be computed under Nakagami-m fading as*

$$P_2 = P_{23} - F_{\gamma_{ps}^{DL}}(\gamma_p), \tag{3.62}$$

where P_{23} is given by

$$P_{23} = 1 - 2\sum_{\mathrm{k}=0}^{\mathrm{m}_{ps}-1} \left(\frac{T_0\gamma_s}{T_1}\right)^{\mathrm{k}} \frac{1}{\Gamma(\mathrm{m}_{sr})} \left(\frac{\mathrm{m}_{sr}}{\Omega_{sr}}\right)^{\mathrm{m}_{sr}} \frac{1}{\mathrm{k}!} \left(\frac{T_0\gamma_s\Omega_{sr}}{T_1\mathrm{m}_{sr}}\right)^{\frac{\mathrm{m}_{sr}-k}{2}}$$
$$\times \mathcal{K}_{\mathrm{m}_{sr}-k}\left(2\sqrt{\frac{T_0\gamma_s\mathrm{m}_{sr}}{T_1\Omega_{sr}}}\right). \tag{3.63}$$

Proof. By following the same line of derivation used to obtain (3.59) in Appendix F, one can get the result in (3.62). ■

Thus, the required OP for the cases of ipSIC and pSIC can be evaluated by inserting the associated CDF and above-mentioned probability expressions in (3.55).

Remark 2: Under the proposed CSS schemes, ST can apply NOMA only when the target rate of the primary network is not satisfied. Otherwise, secondary communication takes place separately in conjunction with primary communication. Therefore, the performance of the secondary network is greatly influenced by the parameters of the primary network. As such, the impact of ipSIC/pSIC may become insignificant depending upon m_{pq} and γ_p of primary communication network.

3.4 Overall EH-OCNOMA System Performance

This section investigates the throughput and energy efficiency measures for the considered EH-OCNOMA system based on the outcomes in previous sections.

3.4.1 System Throughput

The system throughput is a crucial performance metric for evaluating the spectrum utilization of the considered EH-OCNOMA. It essentially signifies the mean spectral efficiency for cooperative communication based wireless networks [77], [53]. In this chapter, it is defined as the sum of individual target rates for both the primary and secondary communications that can be accomplished successfully over the Nakagami-m fading channels. Relying on the results derived in sections 3.2 and 3.3, we obtain here the system throughput for the respective CSS-IAF and CSS-IDF schemes as

$$\mathcal{S}_T^{\mathrm{AF}} = \frac{(1-\alpha)}{2}\Big[\left(1 - P_{\mathrm{out}}^{\mathrm{AF}}\left(R_p\right)\right) R_p + \left(1 - P_{\mathrm{out}}^{\mathrm{AF}}\left(R_s\right)\right) R_s\Big] \tag{3.64}$$

and

$$\mathcal{S}_T^{\mathrm{DF}} = \frac{(1-\alpha)}{2}\Big[\left(1 - P_{\mathrm{out}}^{\mathrm{DF}}\left(R_p\right)\right) R_p + \left(1 - P_{\mathrm{out}}^{\mathrm{DF}}\left(R_s\right)\right) R_s\Big]. \tag{3.65}$$

It can be observed that the maximum achievable system throughput is $\mathfrak{R}(1-\alpha)$ with setting $R_p = R_s = \mathfrak{R}$ for both the proposed schemes, which could be attained with pSIC conditions at a high SNR region, as the OP approaches zero.

3.4.2 Energy Efficiency

Based on the throughput expressions in (3.64) and (3.65), one can quantify the energy efficiency of the considered EH-OCNOMA system under the CSS-IAF and CSS-IDF schemes. As a result of such analysis, an EH-OCNOMA system with an extended network lifespan can be designed. Fundamentally, the system energy efficiency refers to the ratio between the amount of data delivered and the amount of energy consumed [77], [78]. The system throughput represents the total amount of data delivered as given in (3.64) and (3.65) for the CSS-IAF and CSS-IDF schemes, respectively. The energy consumed by the PT in the EH phase (of duration αT) and in the first IT phase (of duration $(1-\alpha)T/2$) accounts for the overall energy consumed in the TS-based EH approach for the considered system. It should be emphasized that the energy consumed in the second IT phase is the energy harvested by node S in the EH phase, and thus, does not contribute to the overall energy consumed in the system. Hence, the energy efficiency for the proposed EH-OCNOMA system under the CSS-IAF and CSS-IDF schemes can be expressed as

$$\Xi^{\mathrm{AF}} = \frac{\mathcal{S}_T^{\mathrm{AF}}}{P_p\left[\alpha + \frac{(1-\alpha)}{2}\right]} \tag{3.66}$$

and

$$\Xi^{\mathrm{DF}} = \frac{\mathcal{S}_T^{\mathrm{DF}}}{P_p\left[\alpha + \frac{(1-\alpha)}{2}\right]}, \tag{3.67}$$

where $\mathcal{S}_T^{\mathrm{AF}}$ and $\mathcal{S}_T^{\mathrm{DF}}$ in bps/Hz are given in (3.64) and (3.65), respectively.

Remark 3: We can observe that the harvested energy at the ST increases with increase in TS parameter α, where $\alpha \in (0,1)$ refers to the fraction of transmission block time T for EH and rest $(1-\alpha)$ for IT. On the contrary, an increase in α also brings a decrease in IT time. Thereby, with the initial increase in α, the system throughput improves as a result of the more harvested energy at the ST. However, with a further increase in α, the degradation in system throughput results due to the decreased IT time.

3.5 Results and Discussion

This section carries out the numerical findings to validate our analytical expressions derived in the previous sections and endorses the results further through Monte-Carlo simulations, while examining the impact of critical measures on the system performance. For the proposed EH-OCNOMA system, we plot the curves based on the mathematical analysis for the two CSS schemes build on the IR protocol using AF and DF strategies, viz., CSS-IAF and CSS-IDF. Further, we plot the curves for the FR-based AF and DF relaying schemes through simulations to compare their performance with the proposed schemes. It is demonstrated from the various figures that the proposed schemes improve the overall performance of considered EH-OCNOMA in terms of the OP, system throughput, and energy efficiency. Moreover, DF relaying outperforms the AF relaying for both IR and FR based schemes. Unless otherwise stated, we set the following parameters: $m_{pq} = 1$, $m_{ps} = 2$, $m_{sq} = m_{sr} = m_R = 3$ as fading severity parameters, $\Omega_{pq} = \Omega_{ps} = \Omega_{sq} = 1$, $\Omega_{sr} = 16$ as the average power[6] of the multipath components, $\Omega_R = 0.01$ as the mean value of the IS channel power gain, $\alpha = 0.18$ as the TS parameter, $\Theta = 0.7$ as the energy conversion efficiency, η_p as the SNR, $N_o = 1$, and block duration $T = 1$ sec. We also set $M = 50$ in Sec. 3.2.2 to significantly reduce the approximation error [76].

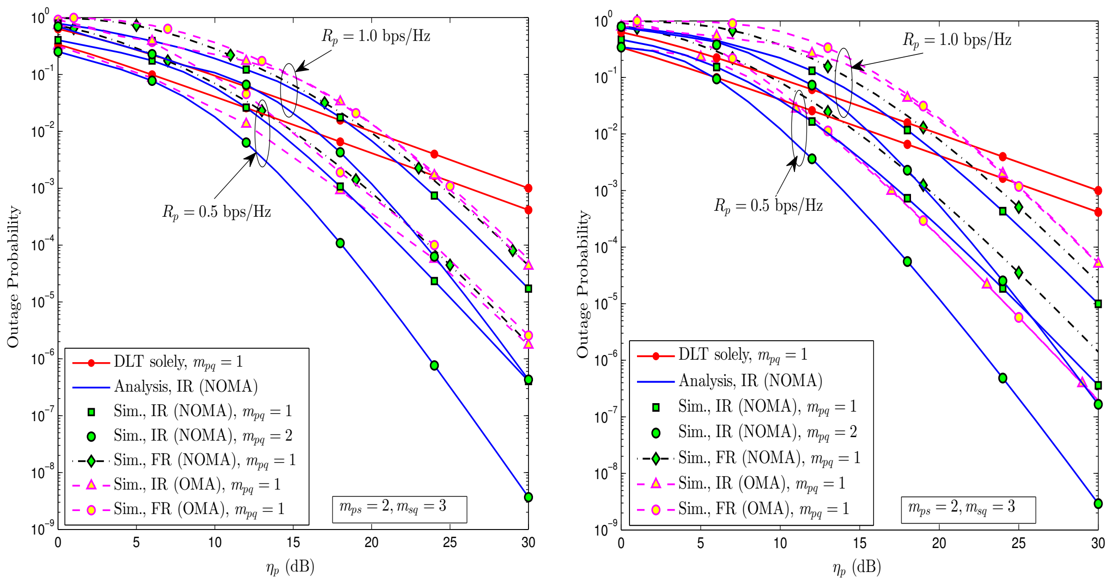

(a) (b)

Figure 3.4: OP versus SNR plots for the primary network with different target rates (R_p) (a) AF (b) DF.

In Fig. 3.4, we plot the OP versus SNR curves for the primary network under the AF and DF relaying to show the impact of various values of target rates (R_p).

[6] In the path loss environment, the average power of fading channel coefficients are presented as $\Omega_{ij} = d_{ij}^{-\nu}$ [79], where d_{ij} is the normalized distance between transmit node i and receive node j, and ν be the path loss exponent which is function of carrier frequency, environment, obstructions, etc. It typically ranges from 2 to 6 (at around 1 GHz) in the free-space loss to the dense urban environmental conditions, correspondingly. As such, in the RF-based EH system, the RF energy must be extracted at very low power density since the propagation energy drops off at the rate of $d_{ij}^{-\nu}$.

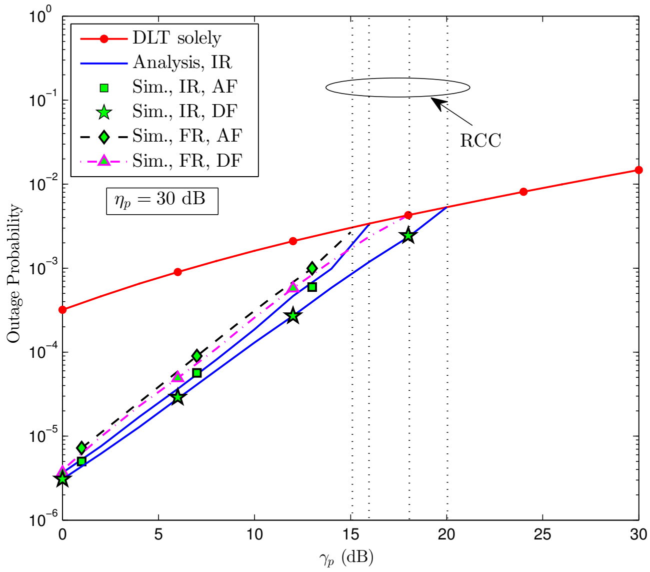

Figure 3.5: OP versus γ_p plots for the primary network.

Herein, we set $R_p = 0.5, 1.0$ bps/Hz. Based on the values of R_p and α, we decide the appropriate value of ζ for the CSS-IAF and CSS-IDF schemes according to Sec. 3.2.3. It can be observed that the proposed schemes outperform the FR-based schemes over the entire SNR regime, and the performance of the DF relaying strategy is slightly better than that of the AF relaying one. Further, the OP performance for the baseline DLT scheme and the OMA scheme is also depicted for comparison purposes. From the plot, one can observe that the proposed CSS schemes considerably outperform the DLT scheme in the medium-to-high SNR regime. This is because of the additional diversity gain obtained through the proposed CSS schemes. The CSS schemes with NOMA surpass the OMA scheme for the high data rate requirements. Since the OMA scheme requires three time slots to execute its operation [26], the target SINR threshold (for a fixed value of target rate) relatively increases for the OMA scheme which degrades its performance. However, for the low data rate requirements, the OMA scheme can provide better performance compared to NOMA in the low SNR region. Moreover, it is evident that as the target rate increases from $R_p = 0.5$ to 1.0 bps/Hz, the outage performance of the primary network degrades.

Fig. 3.5 depicts the OP versus threshold γ_p for the primary network to show the superiority of proposed IR-based schemes over the FR-based schemes. For this, we set the SNR as $\eta_p = 30$ dB. We further select the value of ζ based on fulfilling the QoS criteria as discussed in Sec. 3.2.3. From the figure, one can observe that the OP degrades as the value of γ_p increases. When the threshold approaches $\gamma_p = \frac{\zeta}{1-\zeta} + \gamma_p'$

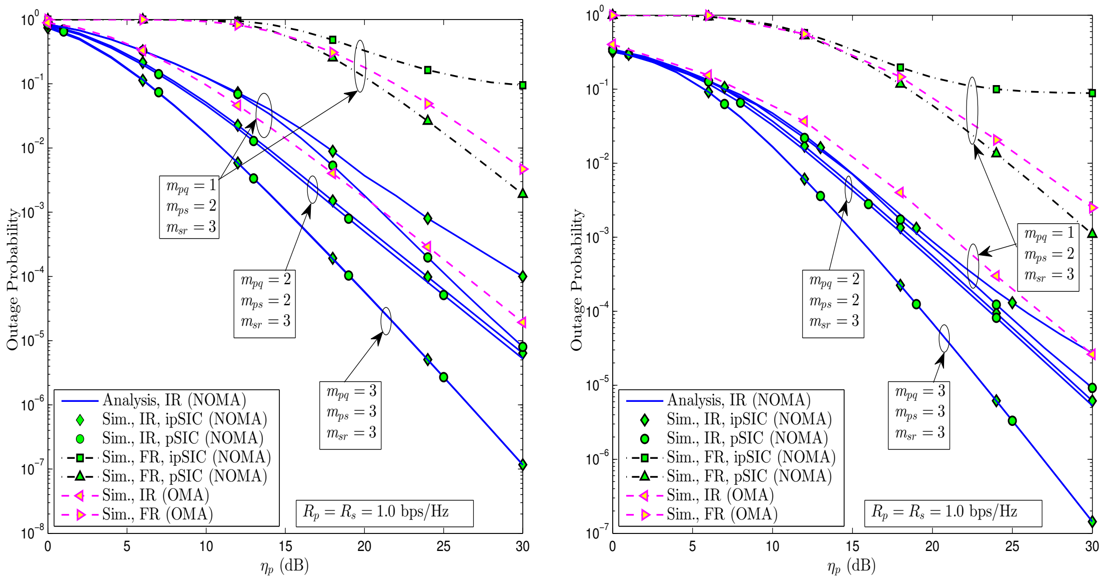

(a) (b)

Figure 3.6: OP versus SNR plots for the secondary network (a) AF (b) DF.

[refer to (3.34) and (3.43)] for both CSS-IAF and CSS-IDF schemes, the RCC effect occurs, and hereby, the performance of the proposed schemes follow the DLT scheme. On the contrary, for the FR-based schemes, this RCC effect takes place relatively at the lower value of threshold i.e., $\gamma_p = \frac{\zeta}{1-\zeta}$. Hence, the proposed schemes can support comparatively higher data rates till the occurrence of RCC effect.

Fig. 3.6 illustrates the OP performance of the secondary network under the AF and DF relaying strategies using the derived analytical expressions in Section 3.3. For this, we particularly plot the curves for both ipSIC and pSIC cases while setting the values of target rates as $R_p = R_s = 1.0$ bps/Hz. Resorting to the values of target rates and α, we find the respective values of ζ for the CSS-IAF and CSS-IDF schemes. The performance gap between pSIC and ipSIC cases, which is more pronounced for AF than DF relaying, diminishes with the increase of $m_{pq} = 1, 2, 3$. This is because better primary channel condition helps the primary network to meet its target rate and thereby relaxes the requirement of NOMA-based cooperative relaying by the secondary network. We can also see that, under the case of pSIC, the CSS schemes with NOMA offer relatively better outage performance than the benchmark OMA scheme.

Fig. 3.7 shows the impact of ipSIC on the OP performance of secondary network by varying the values of Ω_R. For this, we set $R_p = R_s = 1.0$ bps/Hz. As can be seen from the figure, the OP performance improves with the decrease in the level of ipSIC

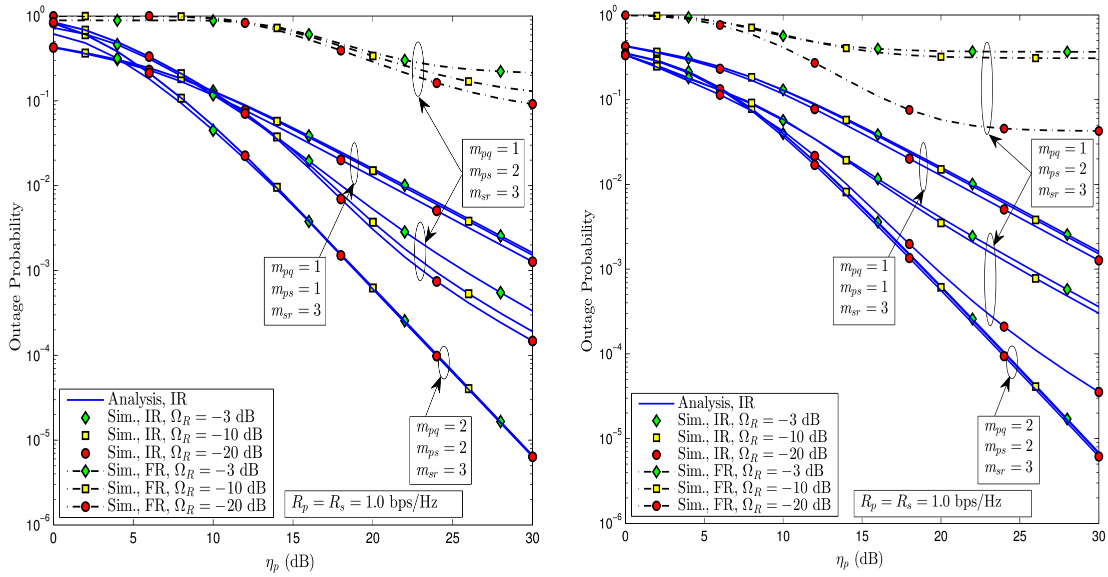

(a) (b)

Figure 3.7: Impact of ipSIC on the OP performance of secondary network (a) AF (b) DF.

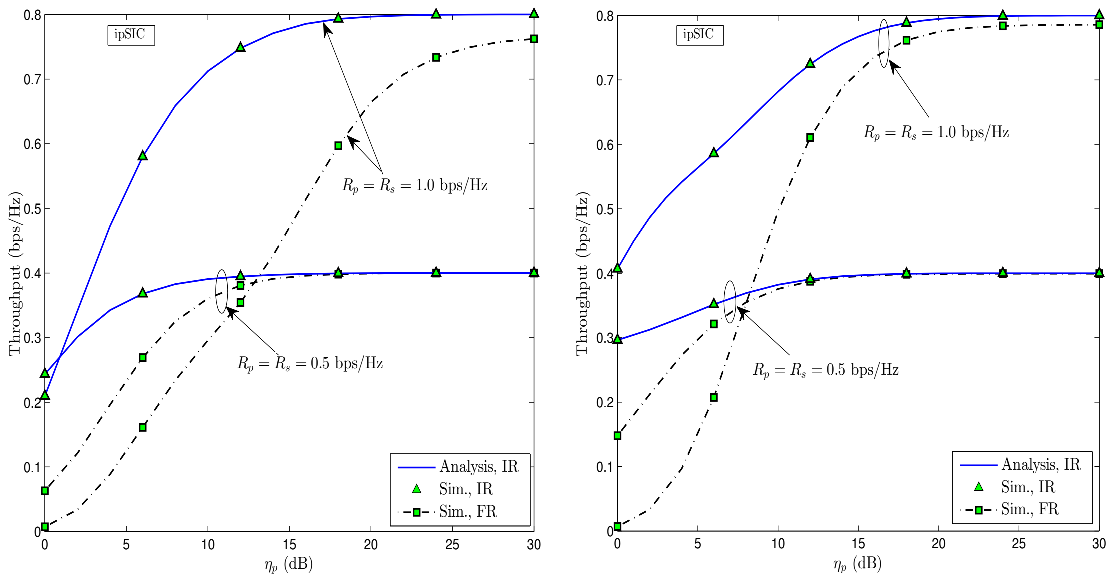

(a) (b)

Figure 3.8: Throughput versus SNR plots for the EH-OCNOMA system (a) AF (b) DF.

($\Omega_R = -3, -10, -20$ dB), especially when $\{m_{pq} = 1, m_{ps} = 2, m_{sr} = 3\}$. We can further see that when Ω_R decreases, the secondary network performance gets more improved under the CSS-IDF scheme as compared with the CSS-IAF scheme in the high SNR regime. This is because the performance of secondary network improves under CSS-IDF scheme when m_{ps} increases as it can help in decoding of primary signal at the ST node (relay). The impact of ipSIC/pSIC gets insignificant as the

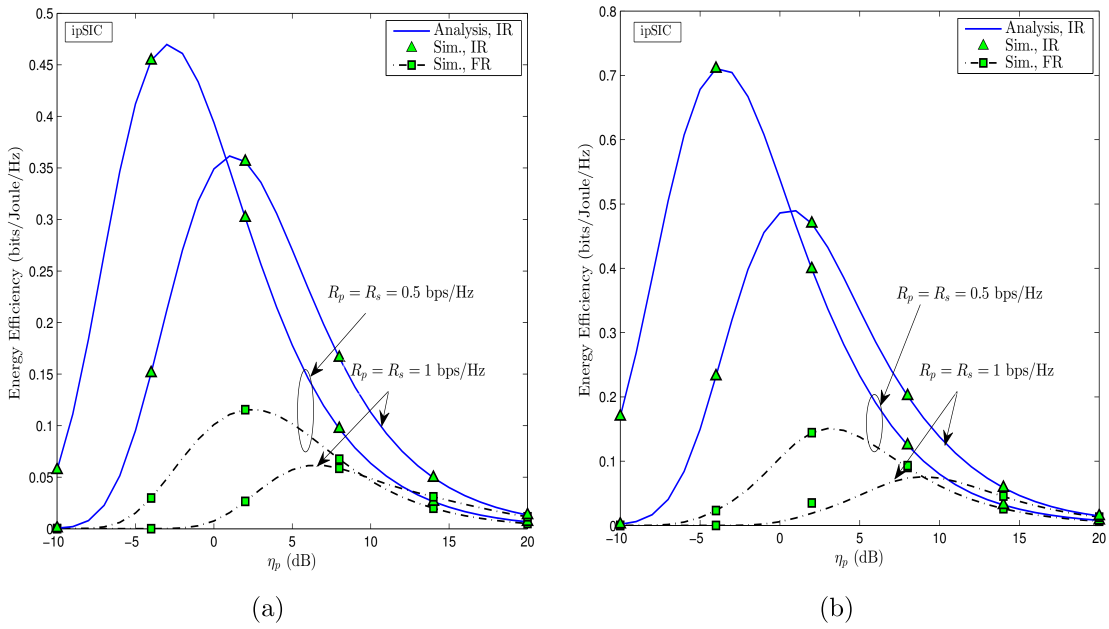

Figure 3.9: Energy efficiency versus SNR plots for the EH-OCNOMA system (a) AF (b) DF.

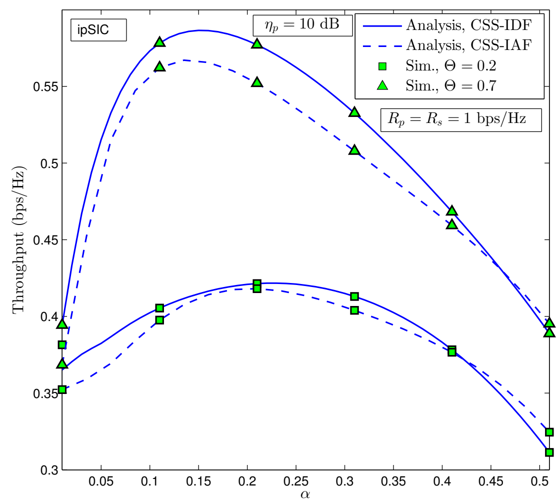

Figure 3.10: Throughput versus α plots for the EH-OCNOMA system.

value of m_{pq} increases. This is attributed to the fact that NOMA based relaying at the ST node is employed only when the target rate of the primary network is not satisfied. Otherwise, ST utilizes all the harvested power for its own communication only.

Fig. 3.8 exhibits the system throughput versus SNR curves for two distinct values of target rates ($R_p = R_s = 0.5, 1.0$ bps/Hz). One can observe from the figure that the proposed IR-based schemes substantially improve the system throughput as compared to the FR-based schemes, specially in low-to-medium SNR regime. In the high SNR region, the system throughput saturates as the OP tends to zero. Thus, the maximum system throughput for both the FR- and IR-based schemes become the sum of individual target rates of the primary and secondary networks.

Fig. 3.9 shows the impact of the SNR on the energy efficiency of the proposed EH-OCNOMA system for two different values of target rates ($R_p = R_s = 0.5, 1.0$ bps/Hz) under the AF and DF relaying strategies. It can be observed from the curves that the energy efficiency is maximal at a certain value of the SNR for a particular target rate. By varying the target rate, the SNR value at which systems achieves maximum energy efficiency also varies. It is also worth noting that the system energy efficiency is lowest in the high SNR region, because the utilized power is much higher than the system throughput at higher SNR values. Further, it can be observed that the IR protocol is more energy efficient than the FR protocol.

Fig. 3.10 depicts the impacts of the TS parameter α and energy conversion factor Θ on the system throughput for a certain value of target rates ($R_p = R_s =$ 1.0 bps/Hz). From the curves, it can be visualized that when α increases, the system throughput initially increases up to some extent, and afterwards, it starts to decrease. Hereby, one can observe an effective value of α around 0.18. Such performance characteristic conforms that the harvested energy at the ST increases with an increase in α. However, an increase in α subsequently decreases the IT time. Thereby, with the initial increase in α, the system throughput improves as a result of more harvested energy at the ST. However, with a further increase in α, the degradation in system throughput results due to the decreased IT time. The effective value of α decreases for the CSS-IAF scheme as compared to the CSS-IDF scheme. On the other hand, when Θ increases, the throughput performance of the EH-OCNOMA system upgrades. It accords with the basic fact that the amount of energy harvested in EH phase increases as the energy conversion factor Θ increases.

3.6 Summary

In this chapter, we investigated the performance of an EH-OCNOMA system over the Nakagami-m fading channel, wherein an energy-constrained ST node has been assumed to cooperate with the primary signal transmission while simultaneously transmitting its own information using the NOMA principle. For this, we proposed two CSS schemes based on IR protocol using the AF and DF relaying strategies, viz., CSS-IAF and CSS-IDF, and compared their performance with the conventional

FR-based AF and DF relaying schemes, DLT scheme, and OMA scheme. The proposed schemes have significantly improved the performance of both primary and secondary networks over the baseline schemes, as the proposed schemes efficiently utilize the available spectrum resources to improve the system performance. Further, to get more insight, we examined the system throughput and energy efficiency for the considered EH-OCNOMA system. Above all, a comparison with FR-based schemes reveals that the proposed schemes can support relatively higher data rates till the occurrence of the RCC effect. Further, the CSS-IDF scheme illustrates comparatively better performance than its CSS-IAF counterpart. Additionally, the performance of secondary network is significantly improved for the CSS-IDF scheme.

CHAPTER 4

IOT-BASED COORDINATED AND DIRECT RELAY TRANSMISSION NETWORK WITH NOMA

In recent years, the IoT has been highlighted for its ability to connect things in the physical world by exploring wireless communication technologies [80], leading to WBANs [81], D2D communications [82], and vehicular networks [83]. It allows entities to be controlled remotely across existing infrastructure, and it is an intelligent technology that reduces human effort while facilitating the access to physical devices. However, given the large scale of application of IoT devices, the resulting spectrum scarcity needs to be addressed [84]. In the previous chapter, we integrated overlay CR with NOMA to improve the SE. Another strategy that can maximize SE of 5G wireless networks is utilizing NOMA based CDRT. The NOMA-based CDRT enables the source node to communicate directly with the near-by user, while a dedicated relay is used to communicate with the far-off user [85]. Authors in [29] have studied the NOMA with CDRT and demonstrated that the proposed scheme outperforms the NOMA without CDRT in terms of ESC. Based on [29], authors in [18] proposed a dynamic transmission scheme for NOMA-based CDRT system. In [87], authors investigated a device-to-device aided NOMA-based CDRT network where the proposed network outperforms the conventional CDRT network in terms of ESC and sum throughput. Very recently, by considering IoT-based CDRT with NOMA assisted network, the system performance was examined for the OP and ESC [88].

Besides SE improvement of IoT-based CNOMA-CDRT network, EE is another key parameter that should be considered while designing a futuristic 5G wireless network to enhance the lifespan. Recent studies indicate that the power requirement of IoT sensors and devices could be met by harvesting energy from RF signals.

In fact, RF signals carry both energy and information. The IoT sensors or nodes can recharge themselves by energy harvested from RF signals while simultaneously decoding the information data and relaying or transmitting the source node's information to its destination[90]. Among the potential EH techniques, SWIPT has received much attention as the key enabling technique for future IoT networks[91]. A SWIPT-based amplify-and-forward (AF) relaying NOMA network was investigated over imperfect Weibull channels considering imperfect channel state information and residual hardware impairments (HI) in [92]. Authors in [14] examined an overlay CNOMA with TS-based receiver architecture considering HI at transceivers for OP performance. A NOMA-assisted cooperative overlay spectrum-sharing network was developed in [93] where a full-duplex ST is exploited for relaying the primary information, and in exchange, STs can harvest energy and access the primary spectrum.

The research mentioned above mainly investigated the impact of deploying NOMA in CR networks, while EH has received less attention in the context of cognitive IoT implementations. The research work in [29], [89] emphasized the NOMA-based CDRT network but have considered the ideal case of pSIC and analysed the system performance over Rayleigh fading channels. However, it is unviable to implement the pSIC in a practical scenario considering error propagation and complexity scaling [24]. Above all, it is apparent from the literature survey that employing EH with overlay CNOMA-CDRT network still stands unexplored. Inspired by these studies, we propose a SWIPT enabled IoT based overlay CNOMA-CDRT system considering both pSIC and ipSIC. The IoT-relay employs TS-based receiver architecture for EH and operates in a DF relaying mode.

In summary, the key contributions of this chapter are emphasized as follows:

- We propose a novel SWIPT enabled IoT-based CNOMA-CDRT system in which cellular primary network collaborates with a cognitive IoT network to further improve far user performance by exploiting the NOMA principle. In view of the practical implementation of the proposed work, we investigate the impact of pSIC and ipSIC on the system performance.

- For the proposed system model, we investigate the outage performance of both primary and secondary networks under the pSIC/ipSIC cases. For this, we analytically derive the expressions of the OP for pSIC/ipSIC cases based on their received SNRs and SINRs over Nakagami-m fading environment.

- With the derived OP expressions, we evaluate the system throughput and EE to gain further insights into the considered system.

- Additionally, we propose an iterative algorithm to minimize a user's OP over an optimal TS factor to further improve the performance of the proposed system.

The rest of the chapter is arranged as follows. In Section 4.1, the description of the proposed SWIPT enabled IoT-based CNOMA-CDRT network is given while deriving the end-to-end SNRs/SINRs. Section 4.2 investigates the system performance in terms of OP, system throughput, and EE. Section 4.3 elucidates the results and discussions, followed by some concluding remarks in Section 4.4.

4.1 System Descriptions

As shown in Fig. 4.1, we propose an EH assisted IoT-based CDRT system with overlay CNOMA, where a primary network coexists with a secondary network. The primary network consists of a PT node P, near user $UE1$ and far user $UE2$, whereas an energy-constrained IoT-relay node S and IoT user ($IoT\text{-}U$) node R make up the secondary network. Herewith, node P directly communicates with $UE1$, whereas, to establish communication with $UE2$, it seeks cooperation from the energy-constrained IoT-relay node S, which acts as a DF relay. The direct link from source node P to $UE2$ or $IoT\text{-}U$ is presumed to be unavailable due to the long distance and severe path loss [88]. As IoT-relay node S is energy limited, it has to first harvest energy from the radiated RF signal by the source node and then split the corresponding power to relay the primary signal as well as to transmit its own information. Here, the TS-based receiver architecture is implemented at node S for EH and IT. As shown in Fig. 4.2, the time block duration T is divided in the ratio of $\alpha T : (1-\alpha)T$, with $\alpha \in (0,1)$ being the TS parameter. The αT duration corresponds to EH phase and remaining $(1-\alpha)T$ duration is used for the IT phase. Additionally, the duration of $(1-\alpha)T$ is subdivided into two IT phases to facilitate overall communication. All the nodes are equipped with a single antenna and operate in half-duplex mode. The channel coefficients for the links P-$UE1$, P-$UE2$, P-S, S-$UE1$, S-$UE2$, and S-R are denoted by $h_{p,1}$, $h_{p,2}$, $h_{p,s}$, $h_{s,1}$, $h_{s,2}$, and $h_{s,r}$, respectively. Considering Nakagami-m fading environment, the PDF and CDF of $|h_{i,j}|^2$, for $i \in \{p, s\}$ and $j \in \{1, 2, s, r\}$

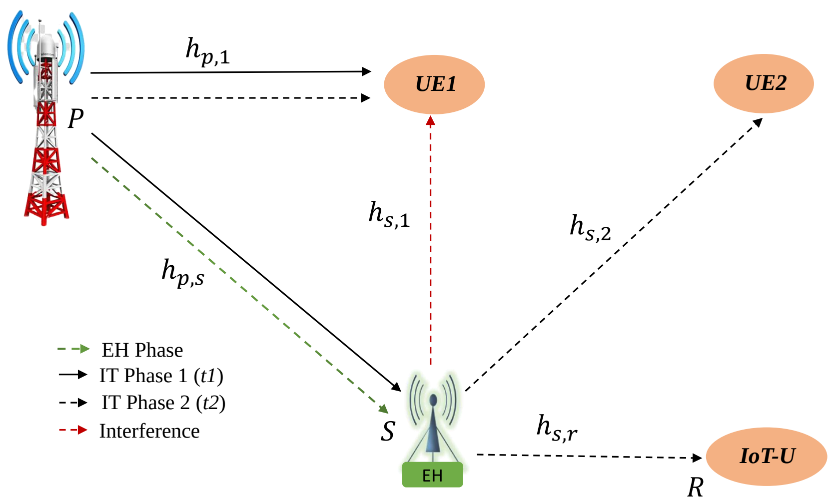

Figure 4.1: Proposed system model.

with $i \neq j$, can be given respectively by

$$f_{|h_{i,j}|^2}(x) = \left(\frac{m_{ij}}{\Omega_{ij}}\right)^{m_{ij}} \frac{x^{m_{ij}-1}}{\Gamma(m_{ij})} \mathrm{e}^{-\frac{m_{ij}}{\Omega_{ij}}x} \tag{4.1}$$

and

$$F_{|h_{i,j}|^2}(x) = \frac{1}{\Gamma(m_{ij})} \Upsilon\left(m_{ij}, \frac{m_{ij}}{\Omega_{ij}}x\right), \tag{4.2}$$

where Ω_{ij} is the average power and m_{ij} is the fading severity parameter. It is assumed that each receiving node suffers from an AWGN, modelled as $\mathcal{CN}(0, N_o)$.

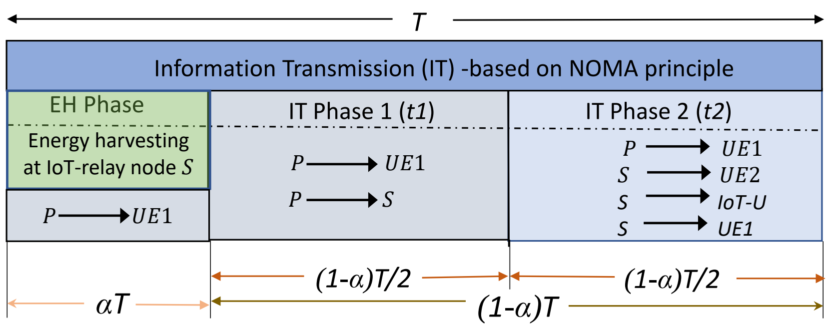

Figure 4.2: Transmission block structure for EH and IT phases.

4.1.1 EH Phase

During the αT duration, source node P transmits its energy signal to S which is also received by $UE1$. Thus, total energy harvested during this time period at node S can be given as

$$E_h = \eta P_p |h_{p,s}|^2 \alpha T, \tag{4.3}$$

where P_p is the source transmit power and $\eta \in (0,1)$ is the energy conversion efficiency which depends on the rectification process and the EH circuitry [16]. Hence, the transmit power of node S over the time $(1-\alpha)T/2$ can be obtained as

$$P_s = \frac{E_h}{(1-\alpha)T/2} = \beta P_p |h_{p,s}|^2, \tag{4.4}$$

where $\beta = \frac{2\eta\alpha}{1-\alpha}$.

4.1.2 IT Phase

The dedicated time for IT i.e., $(1-\alpha)T$ is subdivided into two equal sub-slots: IT phase 1 (denoted as $t1$) and IT phase 2 (denoted as $t2$). During $t1$, source node P transmits its NOMA signal $X_p = \sqrt{\psi_1 P_p} x_1 + \sqrt{\psi_2 P_p} x_2$ towards the nodes $UE1$ and S. Note that x_1 and x_2 are the intended signals for $UE1$ and $UE2$, respectively, and ψ_i is the PAF with $\sum_{i=1}^{2} \psi_i = 1$, $\psi_2 > \psi_1$. Thus, the received signals at nodes $UE1$ and S are represented by $y_{p,1}$ and $y_{p,s}$, respectively, which are given as

$$y_{p,j} = h_{p,j} X_p + n_{p,j}, \ \text{ for } j \in \{1, s\}, \tag{4.5}$$

where $n_{p,j}$ is the AWGN variable. Following the NOMA principle, $UE1$ performs SIC to decode the symbol x_1. Firstly, $UE1$ decodes the symbol x_2 assuming x_1 as noise and then, after performing SIC, symbol x_1 is decoded at $UE1$. Thus, the received SINRs at $UE1$ to decode x_2 and x_1, respectively, are expressed as

$$\gamma^{t1}_{x_2 \to p,1} = \frac{\psi_2 \eta_p |h_{p,1}|^2}{\psi_1 \eta_p |h_{p,1}|^2 + 1}, \tag{4.6}$$

$$\gamma^{t1}_{x_1 \to p,1} = \frac{\psi_1 \eta_p |h_{p,1}|^2}{\lambda \psi_2 \eta_p |h_1|^2 + 1}, \tag{4.7}$$

where $\eta_p = \frac{P_p}{N_0}$ is the transmit SNR at source node and λ $(0 < \lambda < 1)$ is the residual interference parameter pertaining to ipSIC, with $\lambda = 0$ corresponds to pSIC. Here, h_1 denotes residual IS channel coefficient at $UE1$ subjected to Nakagami-m fading with m_1 as fading severity parameter and average channel power gain as Ω_1.

Moreover, the end-to-end SINR at node S for decoding x_2 can be given as

$$\gamma^{t1}_{x_2 \to p,s} = \frac{\psi_2 \eta_p |h_{p,s}|^2}{\psi_1 \eta_p |h_{p,s}|^2 + 1}. \tag{4.8}$$

In the IT phase 2 ($t2$), following the successful decoding of x_2, node S combines x_2 with its own signal x_r to create a superimposed signal $X_s = \sqrt{\psi_2 P_s} x_2 + \sqrt{\psi_r P_s} x_r$ in accordance with NOMA principle, where ψ_2 and ψ_r are PAFs for $UE2$ and IoT-U, respectively, with $\psi_2 + \psi_r = 1$ and $\psi_2 > \psi_r$. This superimposed signal X_s is broadcasted towards the nodes $UE1, UE2$, and IoT-U. Thus, the received signals at $UE2$ and IoT-U are represented by $y_{s,2}$ and $y_{s,r}$, respectively, and are given as

$$y_{s,j} = h_{s,j} X_s + n_{s,j}, \ \text{ for } j \in \{2, r\}, \tag{4.9}$$

where $n_{s,j}$ is the AWGN variable. Here, x_2 can be directly decoded at $UE2$ because of high power allocation, whereas SIC is employed to decode x_r at IoT-U. It first decodes x_2 considering x_r as noise and then decodes x_r by discarding x_2 using SIC. Therefore, the received SINR at $UE2$ to decode x_2 can be given as

$$\gamma^{t2}_{x_2 \to s,2} = \frac{\psi_2 \beta \eta_p |h_{p,s}|^2 |h_{s,2}|^2}{\psi_r \beta \eta_p |h_{p,s}|^2 |h_{s,2}|^2 + 1}. \tag{4.10}$$

While, the received SINRs at IoT-U to decode x_2 and x_r can be, respectively, expressed as

$$\gamma^{t2}_{x_2 \to s,r} = \frac{\psi_2 \eta_p \beta |h_{p,s}|^2 |h_{s,r}|^2}{\psi_r \beta \eta_p |h_{p,s}|^2 |h_{s,r}|^2 + 1}, \tag{4.11}$$

$$\gamma^{t2}_{x_r \to s,r} = \frac{\psi_r \beta \eta_p |h_{p,s}|^2 |h_{s,r}|^2}{\lambda \psi_2 \beta \eta_p |h_{p,s}|^2 |h_r|^2 + 1}. \tag{4.12}$$

Here, h_r denotes residual IS channel coefficient at IoT-U which is subjected to Nakagami-m fading with m_r as fading severity parameter and average channel power gain as Ω_r.

In order to maximize spectral utilization over the wireless channel, source node P transmits a new signal $\hat{x}_1$ to $UE1$ with transmit power $\sqrt{\psi_3 P_p}, \psi_3 \in (0, 1)$. However, during $t2$, $UE1$ faces the interference from IoT-relay node S, which can be estimated and partially eliminated by using the side information of x_2 which was obtained through SIC process during $t1$. Therefore, the signal received at $UE1$ during $t2$ is given by

$$y^{t2}_{p,1} = \sqrt{\psi_3 P_p} h_{p,1} \hat{x}_1 + h_{s,1} X_s + n_{p,1}, \tag{4.13}$$

and the corresponding SINR, after the partial interference cancellation, is deduced as

$$\gamma^{t2}_{\hat{x}_1\to p,1} = \frac{\psi_3\eta_p|h_{p,1}|^2}{\psi_r\beta\eta_p|h_{p,s}|^2|h_{s,1}|^2+1}. \tag{4.14}$$

Next, based on the derived SNRs/SINRs, we conduct performance analysis of the proposed CNOMA-CDRT system.

4.2 Performance Analysis

In this section, we evaluate the performance of primary and secondary networks in terms of their OP, system throughput, and EE by deriving analytical expressions over Nakagami-m fading channels. To further improve the system performance, we propose an iterative algorithm to minimize the user's OP over an optimal TS factor. Here, we consider R_1, R_2 and R_r as predefined target thresholds for $UE1$, $UE2$, and IoT-U, respectively.

4.2.1 Outage Probability of the Primary Network

Outage Probability of UE1

During $t1$, $UE1$ is said to be in the outage when it is unable to decode either of the symbols x_1 or x_2, and hence its OP can be expressed as

$$P^{t1}_{\text{out},UE1} = 1 - \Pr\left[\gamma^{t1}_{x2\to p,1} > \gamma_{R_2}, \gamma^{t1}_{x_1\to p,1} > \gamma_{R_1}\right], \tag{4.15}$$

where $\gamma_{R_1} = 2^{\frac{2R_1}{1+\alpha}} - 1$ and $\gamma_{R_2} = 2^{\frac{2R_2}{1-\alpha}} - 1$.
Further, we evaluate $P^{t1}_{\text{out},UE1}$ in (4.15) for the ipSIC and pSIC cases in subsequent subsections.

ipSIC For the ipSIC case, $P^{t1}_{\text{out},UE1}$ can be computed through the following theorem.

Theorem 3. *The closed-form expression of $P^{t1}_{out,UE1}$ for ipSIC over Nakagami-m fading can be deduced as*

$$P^{t1,\ ipSIC}_{out,UE1} = 1 - \mathcal{Z}_0 - \mathcal{Z}_1, \tag{4.16}$$

where $\mathcal{Z}_0$ and $\mathcal{Z}_1$ are given by

$$\mathcal{Z}_0 = \sum_{k=0}^{m_{p1}-1} \frac{1}{k!}\left(\frac{m_{p1}\mathcal{U}_2}{\Omega_{p1}}\right)^k e^{-\left(\frac{m_{p1}\mathcal{U}_2}{\Omega_{p1}}\right)} \left[1 - \sum_{j=0}^{m_1-1} \frac{1}{j!}\left(\frac{m_1\mathcal{U}_0}{\Omega_1}\right)^k e^{-\left(\frac{m_1\mathcal{U}_0}{\Omega_1}\right)}\right], \tag{4.17}$$

$$\mathcal{Z}_1 = \sum_{k=0}^{m_{p1}-1} \sum_{k_1=0}^{k} \sum_{k_2=0}^{m_1+k_1-1} \frac{(\bar{\mathcal{U}_1})^{k_1}}{k!\Gamma(m_1)} \left(\frac{m_1}{\Omega_1}\right)^{m_1} \left(\frac{m_{p1}}{\Omega_{p1}}\right)^k \binom{k}{k_1} e^{-\left(\frac{m_{p1}\mathcal{U}_1}{\Omega_{p1}}+\mathcal{B}\mathcal{U}_0\right)} \times \frac{\Gamma(m_1+k_1)\mathcal{U}_0^{k_2}}{k_2!(\mathcal{B})^{m_1+k_1-k_2}}, \tag{4.18}$$

with $\mathcal{U}_1 = \frac{\gamma_{R_1}}{\psi_1\eta_p}$, $\bar{\mathcal{U}_1} = \mathcal{U}_1\lambda\psi_2\eta_P$, $\mathcal{U}_2 = \frac{\gamma_{R_2}}{(\psi_2-\psi_1\gamma_{R_2})\eta_p}$, $\mathcal{U}_0 = \frac{\mathcal{U}_2-\mathcal{U}_1}{\bar{\mathcal{U}_1}}$, $\mathcal{B} = \frac{m_1}{\Omega_1} + \frac{m_{p1}\bar{\mathcal{U}_1}}{\Omega_{p1}}$, *and the condition that* $\gamma_{R_2} < \frac{\psi_2}{\psi_1}$.

Proof. See Appendix G. ∎

pSIC Herein, by plugging the respective SINRs with $\lambda = 0$ for pSIC case in (4.15), one can compute $P^{t1}_{\text{out},UE1}$ after some manipulations as

$$\begin{aligned} P^{t1,\text{ pSIC}}_{\text{out},UE1} &= 1 - \Pr\left[|h_{p,1}|^2 > \max\{\mathcal{U}_1, \mathcal{U}_2\}\right] \\ &= \Pr\left[|h_{p,1}|^2 \le \Delta_1\right] \\ &= F_{|h_{p,1}|^2}(\Delta_1), \end{aligned} \tag{4.19}$$

where $\Delta_1 \triangleq \max\{\mathcal{U}_1, \mathcal{U}_2\}$. On substituting the corresponding CDF using (4.2) and simplifying using [95, eq. 8.352.1], one can evaluate (4.19) as

$$P^{t1,\text{ pSIC}}_{\text{out},UE1} = 1 - \sum_{k=0}^{m_{p1}-1} \frac{1}{k!}\left(\frac{m_{p1}\mathcal{U}_2}{\Omega_{p1}}\right)^k \mathrm{e}^{-\left(\frac{m_{p1}\Delta_1}{\Omega_{p1}}\right)}, \tag{4.20}$$

under the condition that $\gamma_{R_2} < \frac{\psi_2}{\psi_1}$.

Moreover, during the $t2$ phase, the outage event of $UE1$ can be expressed as

$$P^{t2}_{\text{out},UE1} = 1 - \Pr[\gamma^{t1}_{x_2\to p,1} > \gamma_{R_2}, \gamma^{t2}_{\hat{x}_1\to p,1} > \gamma_{R_1}]. \tag{4.21}$$

Further, we compute OP in (4.21) through the following lemma.

Lemma 7. *The closed-form expression for $P^{t2}_{out,UE1}$ computed over Nakagami-m fad-*

ing channel can be given as

$$P^{t2}_{out,UE1} = 1 - \mathcal{Z}_2 - \mathcal{Z}_3, \tag{4.22}$$

where $\mathcal{Z}_2$ *and* $\mathcal{Z}_3$ *can be given as*

$$\begin{aligned}\mathcal{Z}_2 = &\sum_{k=0}^{m_{p1}-1} \frac{1}{k!}\left(\frac{m_{p1}\mathcal{U}_2}{\Omega_{p1}}\right)^k e^{-\left(\frac{m_{p1}\mathcal{U}_2}{\Omega_{p1}}\right)} \Bigg[1 - \sum_{k_2=0}^{m_{s1}-1} \frac{2}{k_2!}\left(\frac{m_{s1}\bar{\mathcal{U}_0}}{\Omega_{s1}}\right)^{k_2} \left(\frac{m_{s1}\Omega_{ps}\bar{\mathcal{U}_0}}{m_{ps}\Omega_{s1}}\right)^{\frac{m_{ps}-k_2}{2}} \\ &\times \mathcal{K}_{m_{ps}-k_2}\left(2\sqrt{\frac{m_{ps}m_{s1}\bar{\mathcal{U}_0}}{\Omega_{ps}\Omega_{s1}}}\right)\Bigg],\end{aligned} \tag{4.23}$$

$$\begin{aligned}\mathcal{Z}_3 = &\frac{2}{\Gamma(m_{s1})}\left(\frac{m_{s1}}{\Omega_{s1}}\right)^{m_{s1}} \sum_{k=0}^{m_{ps}-1} \frac{1}{k!}\left(\frac{m_{ps}\bar{\mathcal{U}_0}}{\Omega_{ps}}\right)^k \left(\frac{m_{ps}\Omega_{s1}\bar{\mathcal{U}_0}}{m_{s1}\Omega_{ps}}\right)^{\frac{m_{s1}-k}{2}} \\ &\times \mathcal{K}_{m_{s1}-k_1}\left(2\sqrt{\frac{m_{s1}m_{ps}\bar{\mathcal{U}_0}}{\Omega_{s1}\Omega_{ps}}}\right) - \Bigg[\sum_{k=0}^{m_{ps}-1}\sum_{k_1=0}^{k}\sum_{k_2=0}^{m_{p1}+k-1}\sum_{l=0}^{m_{ps}+m_{p1}-j-1}\binom{k}{k_1}\binom{m_{ps}+m_{p1}-j-1}{l} \\ &\times \left(\frac{m_{ps}m_{s1}}{\Omega_{ps}\Omega_{s1}\hat{\mathcal{U}}_{11}}\right)^{k+l} \frac{(-\hat{\mathcal{U}}_1)^{k-k_1}(\hat{\mathcal{U}}_{11})^k(-1)^l}{\Gamma(m_{p1})\Gamma(m_{s1})k!j!}\left(\frac{m_{p1}}{\Omega_{p1}}\right)^{j+l-k} e^{-\left(\Phi-\frac{m_{p1}\hat{\mathcal{U}}_1}{\Omega_{p1}}\right)} \\ &\times \Gamma(m_{p1}+k_1)\Gamma\big(m_{s1}-k-l,\Phi\big)\Bigg],\end{aligned} \tag{4.24}$$

with $\bar{\mathcal{U}_0} = \frac{\mathcal{U}_2-\hat{\mathcal{U}}_1}{\hat{\mathcal{U}}_{11}}$, $\hat{\mathcal{U}}_1 = \frac{\gamma_{R_1}}{\psi_3\eta_p}$, $\hat{\mathcal{U}}_{11} = \hat{\mathcal{U}}_1\psi_r\beta\eta_p$, $\Phi = \frac{m_{ps}m_{s1}\Omega_{p1}}{\Omega_{ps}\Omega_{s1}m_{ps}\hat{\mathcal{U}}_{11}}$, *and the constraint that* $\gamma_{R_2} < \frac{\psi_2}{\psi_1}$.

Proof. See Appendix H. ■

Outage Probability of UE2

For a pre-defined target data rate R_2, the OP for $UE2$ can be formulated as

$$P_{\text{out},UE2} = \Pr[\gamma^{t1}_{x_2\to p,s} > \gamma_{R_2}, \gamma^{t2}_{x_2\to s,2} < \gamma_{R_2}] + \Pr[\gamma^{t1}_{x_2\to p,s} < \gamma_{R_2}]. \tag{4.25}$$

By invoking respective SINR expressions in (4.25), $P_{\text{out},UE2}$ can be expressed as

$$\begin{aligned}P_{\text{out},UE2} =&\Pr\left[\frac{\psi_2\eta_p|h_{p,s}|^2}{\psi_1\eta_p|h_{p,s}|^2+1} > \gamma_{R_2}, \frac{\psi_2\beta\eta_p|h_{p,s}|^2|h_{s,2}|^2}{\psi_r\beta\eta_p|h_{p,s}|^2|h_{s,2}|^2+1} > \gamma_{R_2}\right] \\ &+ \Pr\left[\frac{\psi_2\eta_p|h_{p,s}|^2}{\psi_1\eta_p|h_{p,s}|^2+1} \leq \gamma_{R_2}\right],\end{aligned} \tag{4.26}$$

Letting $W \triangleq |h_{p,s}|^2$ and $V \triangleq |h_{s,2}|^2$, we can evaluate (4.27) as

$$\begin{aligned} P_{\text{out},UE2} &= \Pr\left[W > \mathcal{U}_2, V < \frac{\mathcal{U}_3}{W}\right] + \Pr[W \leq \mathcal{U}_2] \\ &= \int_{\mathcal{U}_2}^{\infty} F_V\left(\frac{\mathcal{U}_3}{w}\right) f_W(w)dw + F_W\left(\mathcal{U}_2\right), \end{aligned} \tag{4.27}$$

with $\mathcal{U}_3 = \frac{\gamma_{R_2}}{(\psi_2 - \psi_r\gamma_{R_2})\beta\eta_p}$ and the conditions that $\gamma_{R_2} < \frac{\psi_2}{\psi_r}$ and $\gamma_{R_2} < \frac{\psi_2}{\psi_1}$. On inserting the respective CDFs and PDF in (4.27), $P_{\text{out,UE2}}$ can be further evaluated as

$$\begin{aligned} P_{\text{out},UE2} = 1 - &\sum_{k=0}^{m_{s2}-1} \frac{1}{\Gamma(m_{ps})k!}\left(\frac{m_{ps}}{\Omega_{ps}}\right)^{m_{ps}} \left(\frac{m_{s2}\mathcal{U}_3}{\Omega_{s2}}\right)^{k} \\ &\times \int_{\mathcal{U}_2}^{\infty} w^{m_{s2}-k-1} \mathrm{e}^{-\left(\frac{m_{s2}\mathcal{U}_3}{\Omega_{s2}w} + \frac{m_{ps}w}{\Omega_{ps}}\right)} dw. \end{aligned} \tag{4.28}$$

As one can observe, it is quite difficult to solve further the integral in (4.28) in an exact closed-form. Therefore, by expanding the term $\mathrm{e}^{-\left(\frac{m_{s2}\mathcal{U}_3}{\Omega_{s2}w}\right)}$ as Maclaurin series [96], (4.28) can be simplified as

$$\begin{aligned} P_{\text{out},UE2} = 1 - &\sum_{k=0}^{m_{s2}-1} \frac{1}{\Gamma(m_{ps})k!}\left(\frac{m_{ps}}{\Omega_{ps}}\right)^{m_{ps}} \left(\frac{m_{s2}\mathcal{U}_3}{\Omega_{s2}}\right)^{k} \\ \times &\sum_{l=0}^{\infty} \frac{(-1)^l}{l!}\left(\frac{m_{s2}\mathcal{U}_3}{\Omega_{s2}}\right)^{l} \int_{\mathcal{U}_2}^{\infty} w^{m_{s2}-k-l-1} \mathrm{e}^{-\frac{m_{ps}}{\Omega_{ps}}w} dw. \end{aligned} \tag{4.29}$$

Now, we can solve the integral in (4.29) using [95, eq. 8.351.2] to get

$$\begin{aligned} P_{\text{out},UE2} = 1 - &\sum_{k=0}^{m_{s2}-1}\sum_{l=0}^{\infty} \frac{(-1)^l}{\Gamma(m_{ps})k!l!}\left(\frac{m_{s2}\mathcal{U}_3}{\Omega_{s2}}\right)^{k+l} \\ \times &\left(\frac{m_{ps}}{\Omega_{ps}}\right)^{m_{ps}-m_{s2}+k+l} \Gamma\left(m_{s2}-k-l, \frac{m_{ps}\mathcal{U}_2}{\Omega_{ps}}\right). \end{aligned} \tag{4.30}$$

Remark 1: The infinite series in (4.29), as obtained by expansion of $\mathrm{e}^{-\left(\frac{m_{s2}\mathcal{U}_3}{\Omega_{s2}w}\right)}$, can be truncated to the first L terms such that the convergence error is kept to a bare minimum. Convergence error because of truncation can be expressed as

$$\epsilon(w) = \left| e^{-\left(\frac{m_{s2}\mathcal{U}_3}{\Omega_{s2}w}\right)} - \sum_{l=0}^{L} \frac{(-1)^l}{l!}\left(\frac{m_{s2}\mathcal{U}_3}{\Omega_{s2}w}\right)^{l} \right|, \tag{4.31}$$

where $|.|$ represents the absolute value. A suitable value for L can be chosen to ensure that the convergence error is minimized. This is illustrated in Fig. 4.3 by

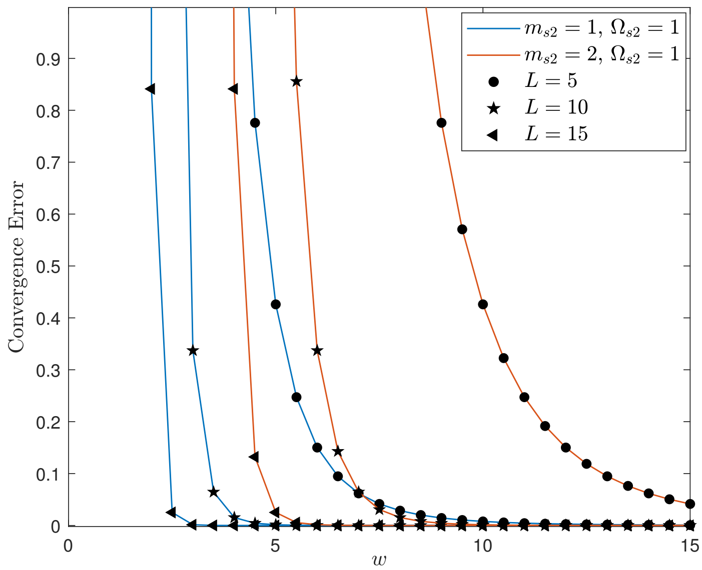

Figure 4.3: Variation of convergence error for different L values.

plotting the convergence error for various values of L and m_{s2}. As can be seen from the figure, the convergence error deviates from zero error line for lower value of L with lower range of w. As we increase the value of L, the convergence error remains zero for medium to high range of w. Thus, for all of the analytical curves shown in Section 4.3, we assume $L = 15$.

4.2.2 Outage Probability of Secondary Network

For the IoT-U, the outage event occurs either when IoT-relay node S could not detect symbol x_2 or when IoT-U node R is unable to detect any symbol in anticipation with successful detection of x_2. For a given target data rate R_r, the OP of the secondary network can be posed as

$$P_{\text{out},sr} = \Pr[\gamma^{t1}_{x_2\to p,s} < \gamma_{R_2}] + \Pr[\gamma^{t1}_{x_2\to p,s} \geq \gamma_{R_2}, \bar{P}_{sr}], \tag{4.32}$$

where $\bar{P}_{sr}$ denotes the OP that SR fails to detect any symbol and can be given as

$$\bar{P}_{sr} = 1 - \Pr[\gamma^{t2}_{x_2\to s,r} > \gamma_{R_2}, \gamma^{t2}_{x_r\to s,r} > \gamma_{R_r}], \tag{4.33}$$

where $\gamma_{R_r} = 2^{\frac{2R_r}{1-\alpha}} - 1$. By invoking the respective SINRs in (4.33) with some algebraic manipulations, $\bar{P}_{sr}$ can be expressed under the ipSIC and pSIC cases as

$$\bar{P}^{\text{ipSIC}}_{sr} = \Pr\left[Z_1 \leq \min\left\{\frac{\mathcal{U}_4}{W}, \frac{\mathcal{U}_5(\psi_2\beta\eta_p W Z_2 + 1)}{W}\right\}\right] \tag{4.34}$$

and

$$\bar{P}_{sr}^{\text{pSIC}} = \Pr\left[Z_1 \leq \frac{\Delta_2}{W}\right], \tag{4.35}$$

respectively, where $W \triangleq |h_{p,s}|^2$, $Z_1 \triangleq |h_{s,r}|^2, Z_2 \triangleq |h_r|^2$, $\mathcal{U}_4 = \frac{\gamma_{R_2}}{(\psi_2 - \psi_r\gamma_{R_2})\beta\eta_p}$, $\mathcal{U}_5 = \frac{\gamma_{R_r}}{(\psi_r - \lambda\psi_2\gamma_{R_2})\beta\eta_p}$, $\bar{\mathcal{U}}_5 = \frac{\mathcal{U}_4 - \mathcal{U}_5}{\mathcal{U}_5\psi_2\beta\eta_p}$, $\mathcal{U}_6 = \frac{\gamma_{R_r}}{\psi_r\beta\eta_p}$, $\Delta_2 \triangleq \min\{\mathcal{U}_4, \mathcal{U}_6\}$.

Further, we compute $P_{\text{out},sr}$ for ipSIC and pSIC cases, conditioned on $\gamma_{R_2} < \frac{\psi_2}{\psi_r}$ and $\gamma_{R_r} < \frac{\psi_r}{\lambda\psi_2}$, in the subsequent subsections.

ipSIC For this case, we substitute (4.34) in (4.32) and proceed further as given in following theorem.

Theorem 4. *An analytical expression for $P_{out,sr}^{ipSIC}$ calculated over Nakagami-m fading can be given as*

$$\begin{aligned}
P_{out,sr}^{ipSIC} =& 1 - \sum_{k=0}^{m_{sr}-1}\sum_{u=0}^{m_r-u}\sum_{l=0}^{\infty} \frac{(-1)^l(\mathcal{A}_1)^l}{l!k!u!\Gamma(m_{ps})}\left(\frac{m_{ps}}{\Omega_{ps}}\right)^{k+u+l}\left(\frac{m_{sr}\mathcal{U}_4}{\Omega_{sr}}\right)^k\left(\frac{m_r\bar{\mathcal{U}}_5}{\Omega_r}\right)^u \\
&\times \Gamma\left(m_{ps} - k - l - u, \frac{m_{ps}\mathcal{U}_2}{\Omega_{ps}}\right) - \left[\sum_{k=0}^{m_{sr}-1}\sum_{m=0}^{k}\sum_{l=0}^{\infty}\binom{k}{m}\frac{(-1)^l\Gamma(m_r+k-m)}{k!l!\Gamma(m_r)\Gamma(m_{ps})}\right. \\
&\left.\times\left(\frac{m_{ps}\mathcal{U}_5}{\Omega_{ps}}\right)^{m+l}\left(\frac{m_{sr}}{\Omega_{sr}}\right)^{k+u}\left(\frac{m_r}{\Omega_r}\right)^{m_r}\mathcal{A}_2^{-(m_r+k-m)}\Gamma\left(m_{ps} - m - l, \frac{m_{ps}\mathcal{U}_2}{\Omega_{ps}}\right)\right] \\
&+\left[\sum_{k=0}^{m_{sr}-1}\sum_{m=0}^{k}\sum_{j=0}^{m_r+k-m-1}\sum_{l=0}^{\infty}\binom{k}{m}\left(\frac{m_{sr}\mathcal{U}_5}{\Omega_{sr}}\right)^k\frac{(-1)^l\Gamma(m_r+k-m)!}{l!k!u!\Gamma(m_{ps})\Gamma(m_r)}\left(\frac{m_r}{\Omega_r}\right)^{m_r}\right. \\
&\left.\times\left(\frac{m_{ps}}{\Omega_{ps}}\right)^{m+j+u}\frac{(\mathcal{A}_3)^u(\beta\eta_p\psi_2)^{k-m}}{\mathcal{A}_2^{m_r+k-m-j}}\Gamma\left(m_{ps} - m - j - l, \frac{m_{ps}\mathcal{U}_2}{\Omega_{ps}}\right)\right].
\end{aligned} \tag{4.36}$$

where $\mathcal{A}_1 = \frac{m_{sr}\mathcal{U}_4}{\Omega_{sr}} + \frac{m_r\bar{\mathcal{U}}_5}{\Omega_r}$, $\mathcal{A}_2 = \frac{m_{sr}\eta_p\mathcal{U}_5\beta\psi_2}{\Omega_{sr}} + \frac{m_r}{\Omega_r}$, $\mathcal{A}_3 = \frac{m_{sr}\mathcal{U}_5\beta\psi_2\bar{\mathcal{U}}_5}{\Omega_{sr}} + \frac{m_{sr}\mathcal{U}_5}{\Omega_{sr}} + \frac{m_r\bar{\mathcal{U}}_5}{\Omega_r}$.

Proof. See Appendix I. ∎

Remark 2: The infinite series in (4.36) is truncated to the first 15 terms for the numerical analysis purposes in Section 4.3 as discussed in *Remark 1*.

pSIC For the pSIC case, (4.25) can be evaluated as $P_{\text{out},sr}^{\text{pSIC}}$ in the following lemma.

Lemma 8. *The analytical expression for $P_{out,sr}^{pSIC}$ calculated over Nakagami-m fading* *can be given as*

$$P^{pSIC}_{out,sr} = 1 - \sum_{k=0}^{m_{sr}-1} \sum_{u=0}^{\infty} \frac{(-1)^u}{k!u!\Gamma(m_{ps})} \left(\frac{m_{ps}}{\Omega_{ps}}\right)^{k+l} \times \left(\frac{m_{sr}\Delta_2}{\Omega_{sr}}\right)^{k+l} \Gamma\left(m_{ps} - k - l, \frac{m_{ps}\mathcal{U}_2}{\Omega_{ps}}\right). \tag{4.37}$$

Proof. By adopting the same line of derivation steps as used to obtain (4.36) in Appendix I, (4.37) can be derived. ■

4.2.3 System Throughput

The system throughput is one of the key performance measures to assess the proposed system spectrum utilization. In the case of cooperative communication based wireless networks, the system throughput implies the mean spectral efficiency[53]. For the proposed SWIPT based NOMA-CDRT system, it can be quantified as the sum of individual target rates for both primary and secondary communications that can be achieved successfully over the Nakagami-m fading channels. From the derived OP expressions, system throughput can be formulated as

$$\mathcal{S}_{\mathcal{T}} = \frac{1-\alpha}{2}\Big[\left(1 - P^{t1}_{\text{out},UE1}\right) R_1 + \left(1 - P^{t2}_{\text{out},UE1}\right) R_1 + \left(1 - P_{\text{out},UE2}\right) R_2 + \left(1 - P_{\text{out},\ sr}\right) R_r\Big]. \tag{4.38}$$

4.2.4 Energy Efficiency

The EE of the proposed system can be evaluated using the system throughput expression in (4.38). We measure EE as the ratio of total data delivered to total energy consumed [77]. Here, total amount of data delivered is given by the system throughput and the required expression for EE of the considered system model can be given as

$$\Xi_{\mathcal{E}} = \frac{\mathcal{S}_{\mathcal{T}}}{\frac{P_p}{2}(1+\alpha)}, \tag{4.39}$$

where $\mathcal{S}_{\mathcal{T}}$ is the achievable throughput as expressed in (4.38).

4.2.5 Optimal Solution for TS Parameter

To determine the optimal TS factor, a low-complexity algorithm is proposed to obtain the minimal OP of users through optimization of the TS factor, α, which is a key parameter to balance the EH and IT phases. For this, we formulate the optimization problem which can be expressed as

$$\begin{aligned} \text{(P1)}:\ & \underset{\alpha}{\text{minimize}} \quad P_{\text{out},n} \\ & \text{s.t. } 0<\alpha<1-\frac{2R_a}{\log_2\left(\frac{\psi_2}{\psi_b}\right)}, \end{aligned} \tag{4.40}$$

where $n \in \{UE1, UE2, sr\}$, $a \in \{1, 2, r\}$, and $b \in \{1, r\}$. Herein, $P_{\text{out},UE1}$ refers to $P^{t1}_{\text{out},UE1}$ and is used for the brevity of presentation. Similar to [94], there is an optimal α^* for the OP curve plotted as a function of α on the interval $[\vartheta < \alpha < 1-2R_a/\log_2\left(\frac{\psi_2}{\psi_b}\right)]$, illuminating the convex functions as shown in Fig. 4.8. Moreover, the properties of the convex functions are demonstrated in [97], thus the proof has been omitted. So, the problem in (4.40) can be re-expressed as

$$\begin{aligned} \text{(P2)}:\ & \underset{\alpha}{\text{maximize}} \quad -P_{\text{out},n} \\ & \text{s.t. } 0<\alpha<1-\frac{2R_a}{\log_2\left(\frac{\psi_2}{\psi_b}\right)}. \end{aligned} \tag{4.41}$$

For the problem formulated in (4.41), we propose an algorithm based on golden search section (GSS) method to find α^* as given in Algorithm 1. The complexity of GSS is $\mathcal{O}(\log(1/\vartheta))$, where ϑ denotes the search accuracy [98]. The number of iterations, i.e., $\mathbb{N}$, can be attained as

$$\mathbb{N} = \frac{2\log(\vartheta)}{\log(1-\mu)}. \tag{4.42}$$

It is evident from (4.42) that the smaller value of the stoping threshold leads to more number of iterations which provides higher accuracy. Note that the aforesaid optimization algorithm requires only the average channel gains of the pertinent links rather than instantaneous channel gains. It has more practical importance [100] since the average channel gains are more stable and can be gathered by capitalizing on the transmission distance, frequency of the radio waves, etc.

Algorithm 1: Algorithm to find optimal TS factor (α^*)

Input Initialize $\alpha_{min} = 0$, $\alpha_{max} = 1 - \frac{2R_a}{\log_2\left(\frac{\psi_2}{\psi_b}\right)}$,
the Golden ratio $\mu = \frac{\sqrt{5}-1}{2}$, $\alpha_1 = \alpha_{max} - (\alpha_{max} - \alpha_{min})\,\mu$,
$\alpha_2 = \alpha_{min} + (\alpha_{max} - \alpha_{min})\,\mu$, and a stopping threshold $\vartheta = 10^{-5}$.
Output $\alpha^* = \frac{\alpha_{max}+\alpha_{min}}{2}$.
while $|\alpha_{max} - \alpha_{min}| \leq \vartheta$ **do**
  Update: $P_{out,\,tem1} \leftarrow P_{out,\,x}(\alpha_1)$
  Update: $P_{out,\,tem2} \leftarrow P_{out,\,x}(\alpha_2)$
    //$\{P_{out,\,x}(\cdot)$ is given by (4.16), (4.30), and (4.36)$\}$
  if $P_{out,\,tem1} < P_{out,\,tem2}$ **then**
    Update: $\alpha_{max} \leftarrow \alpha_2$
  else
    Update: $\alpha_{min} \leftarrow \alpha_1$
  end
  Update: $\alpha_1 \leftarrow \alpha_{max} - (\alpha_{max} - \alpha_{min})\,\mu$
  Update: $\alpha_2 \leftarrow \alpha_{min} + (\alpha_{max} - \alpha_{min})\,\mu$
end

4.3 Numerical Results

In this section, the numerical and simulation results for the proposed IoT-based CNOMA-CDRT system are presented to provide insights and validate our analytical findings in Section 4.2. Here, we consider the following parameters: $\Omega_{p1} = \Omega_{sr} = 16, \Omega_{ps} = \Omega_{s1} = \Omega_{s2} = 1$ as the average power of the multipath components, $\alpha = 0.2$ as the TS factor, the energy conversion efficiency $\eta = 0.7$[14], the PAF as $\psi_1 = \psi_r$ $= 0.3$, $\psi_2 = 0.7$, $\psi_3 = 1$, the residual interference parameter as $\lambda = 0.2$, η_p as the SNR, $N_o = 1$, and the block duration as $T = 1$; unless otherwise defined.

In Fig. 4.4, the outage performance curves for $UE1$ and $UE2$ are plotted against the transmit SNR (η_p) under both pSIC and ipSIC cases. Also, the curves are plotted considering OMA scheme for the comparison purpose. Herein, we took the fixed data rates $R_1 = R_2 = R_{th} = 0.5$ bps/Hz, with varying fading severity parameter (m parameter). For the $UE1$ in IT phase 1, the impact of ipSIC on the OP is shown by varying $\Omega_1 = -10, -20$ dB. One can observe from the figure, as the m parameter increases, outage performance improves; while unlike this observation, as a level of ipSIC Ω_1 increases, outage performance deteriorates. In addition to this, it can be seen that as the η_p increases, outage performance improves for the users $UE2$ and $UE1$ (under pSIC). For the $UE1$, under ipSIC in the IT phase1 and IT phase 2, outage floor appears particularly in the high range of SNR. This is because

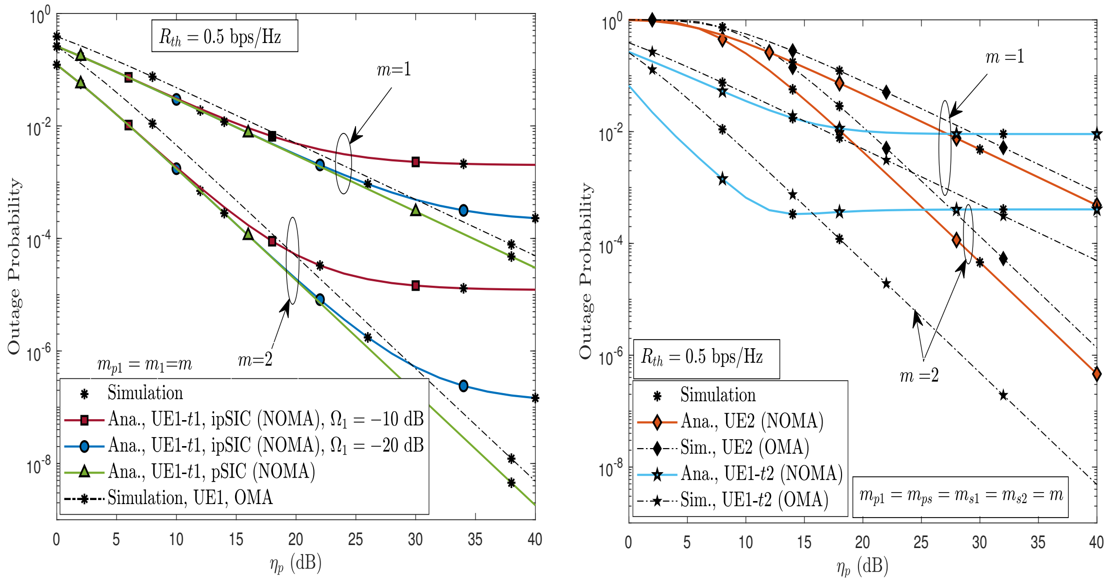

(a) (b)

Figure 4.4: OP versus SNR plots for the primary network with varying m parameter (a) IT phase 1 (b) IT phase 2.

the $UE1$ experiences residual interference during SIC in IT phase 1 and receives interference from IoT-relay in IT phase 2 owing to the simultaneous transmissions from node P and S. It can also be observed that the proposed NOMA scheme outperforms the OMA scheme in lower-to-medium SNR region for the ipSIC case of $UE1$. However, OMA scheme surpasses the NOMA scheme for ipSIC case as SNR increases from medium to high region because of the residual interference, while for $UE2$, the proposed NOMA scheme outperforms the OMA throughout the SNR region. Also, it is found that $UE2$ outperforms $UE1$ under the considered set of parameters, which is expected as per the higher power allocation for $UE2$ and adoption of the NOMA in the second stage of transmission.

Fig. 4.5 demonstrates the OP curves for the $IoT\text{-}U$ plotted against η_p under both the pSIC and ipSIC cases. Herein, we set the target data rates $R_2 = R_r = R_{th} = 0.5$ bps/Hz. As one can observe from the figure, the outage performance of the $IoT\text{-}U$ improves as m parameter increases from 1 to 2. The impact of ipSIC level on outage performance can be observed from the figure when Ω_r varies from -20 dB to -10 dB, the performance gets deteriorated. The outage floor for $\Omega_r = -10$ dB occurs at comparatively lower SNR than $\Omega_r = -20$ dB, which is attributed to an increase in residual interference level. However, no outage floor occurs for the pSIC case owing to the absence of residual interference, and hence, pSIC outperforms ipSIC case. Furthermore, it can also be observed from the plot that the proposed NOMA

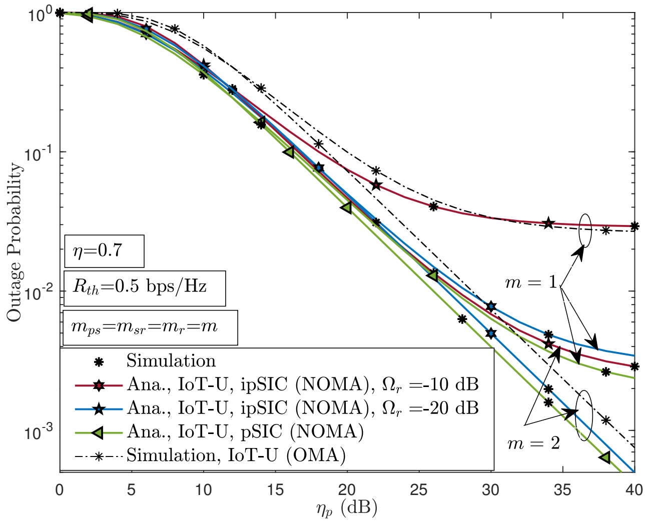

Figure 4.5: OP versus SNR plot for the IoT user.

scheme outperforms the conventional OMA scheme.

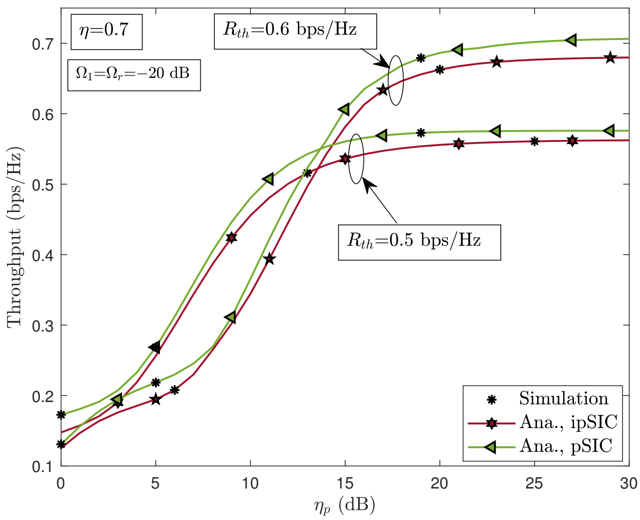

Figure 4.6: System throughput.

Fig. 4.6 illustrates the impact of SNR on system throughput for both the cases of ipSIC and pSIC under the parameter setting as $R_1 = R_2 = R_r = R_{th} = (0.5, 0.6)$ bps/Hz, with all m parameters equal to 2 and $\Omega_1 = \Omega_r = -20$ dB. It can be seen from the figure that the system throughput increases for lower to medium range of SNR, but after that it gets saturated, which refers to the maximum attainable throughput for the specific data rate. For higher data rate, it attains its maximum at relatively high SNR. It happens because the outage performance at a higher target rate is relatively poorer than the lower target rate.

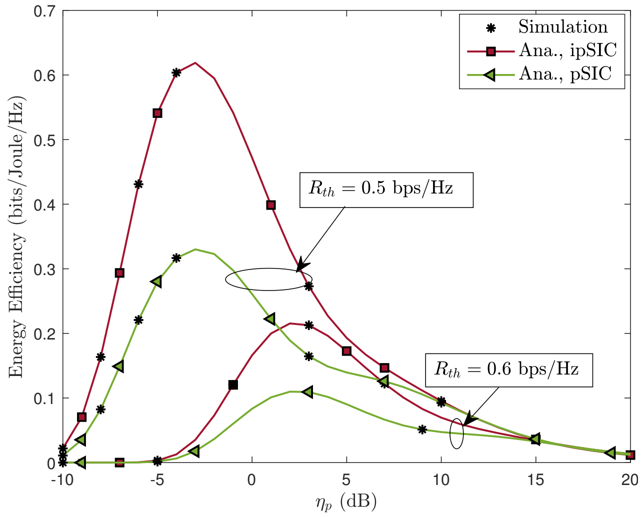

Figure 4.7: Energy efficiency for the CNOMA-CDRT system.

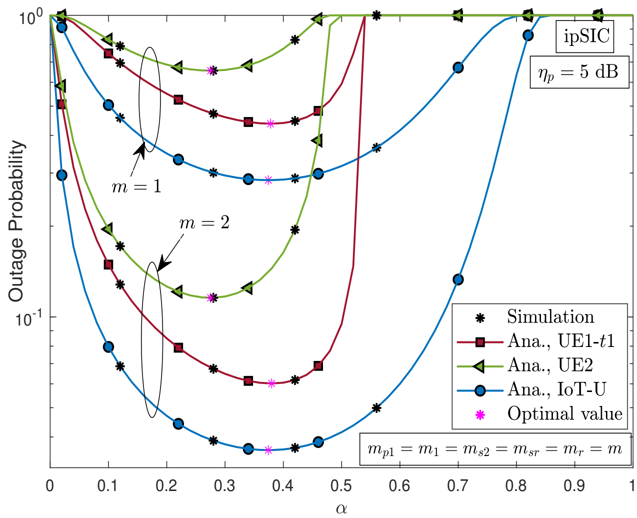

Figure 4.8: OP versus α plot the CNOMA-CDRT system.

Fig. 4.7 depicts the curves for EE versus SNR for both the cases of ipSIC and pSIC under the same set of parameters used in Fig. 4.5. Here, one can observe that the maximum EE attains at a specific SNR for the given target rate. It changes when we change the target rate. Further, high SNR region exhibits the lowest EE because, at high SNR, energy consumption is more than the achieved system throughput.

Fig. 4.8 illustrates the impact of TS factor α on outage performance of $UE1$, $UE2$, and $IoT-U$. Herein, we set the target rates as $R_1 = R_2 = R_r = 0.5$ bps/Hz, transmit SNR $\eta_p = 5$ dB, with varying m parameter. It can be seen that the OP curves of all the users are convex functions of α, and that there are optimal points that minimize the OP of the corresponding users. From the curves, it is obvious that as α increases, the outage performance initially improves, but as α increases further, the outage performance degrades. This outage behavior is a result of the fact that the energy-constrained IoT-relay node is able to harvest energy for a longer time when there is an increase in α. Consequently, the IT time decreases, which degrades the outage performance.

4.4 Summary

In this chapter, we proposed and investigated a SWIPT enabled IoT-based overlay CNOMA-CDRT system that improves spectrum utilization and EE. We evaluated the performance of the proposed system in terms of OP, system throughput and EE by deriving the analytical expressions, which are calculated over Nakagami-m fading for both the pSIC and the ipSIC cases and validated through Monte-Carlo simulations. Numerical results emphasized the importance of employing SWIPT enabled IoT relay which provides self-reliant energy-efficient communication and data transmission.

CHAPTER 5

DEEP LEARNING ANALYSIS OF CDRT SYSTEMS WITH COGNITIVE NOMA

In the previous chapter, we proposed an IoT-based CNOMA-CDRT system with TS-based relaying architecture and examined the system performance in terms of OP, system throughput and EE by deriving the analytical expressions over Nakagami-m fading. However, due to the enormous complexity and variability of future wireless network service requirements, it is probable that standard model-based approaches, i.e., using closed-form expressions, are no longer sufficient for deployment, network resource management, and operation. In recent years, data-driven approaches for system performance evaluation have been developed, such as deep learning modeling, which make performance analysis efficient and accurate without having to make mathematical derivations [99]. Furthermore, data-driven methods can provide real-time configurations and align with future wireless system trends. As a result, the model-based approach has been challenged by the deep learning model for system metric evaluation. Thus, in this chapter, we pursue a deep learning approach along with model-based approach for the performance evaluation of the system.

Different from the previous chapter, here, we proposed an EH-assisted CDRT in an overlay cognitive NOMA with PS-based relaying architecture, assuming pSIC and ipSIC cases. In a nutshell, the main contributions of this chapter are emphasized as follows:

- For the proposed EH-based CDRT-NOMA system, we derive the analytical expressions of the OP for the primary and secondary networks under the pSIC and ipSIC cases. Additionally, a performance comparison with the EH-based CDRT-OMA is carried out through simulations. Moreover, we obtain asymptotic OP expressions at high SNR to provide useful insights.

- Further, to garner the more insight, we also deduce the expressions of system throughput and energy efficiency for the considered EH-based CDRT-NOMA system.

- Owing the high complexity and variability of the proposed system model as characterized by emerging communications system requirements, the derivation of the closed-form expression of the OP is intractable, let alone the EC/ESC. To address these limitations, we propose a data-driven approach through deep learning to estimate the exact EC/ESC along with OP with a high accuracy and low latency.

The rest of the chapter is ordered as follows. In Section 5.1, the system model of EH-based CDRT-NOMA system is framed while deriving the expressions for SINRs over Rician/Rayleigh fading channels. In Section 5.2, we investigate the performance of the proposed network by analyzing the OP, system throughput and EE. Deep learning approach for performance evaluation is presented in Section 5.3 and numerical results are presented in Section 5.4. Finally, Section 5.5 summarizes the chapter.

5.1 System Model

As shown in Fig. 5.1, we propose an EH-based CDRT system with an overlay cognitive NOMA scheme, wherein the primary network consists of a source node S, a near-user D_1 and a far-user D_2, while the secondary network consists of an energy-constrained IoT-transmitter node I (which acts as a PS-based EH DF relay) and an IoT-receiver node R. All the nodes are assumed to be equipped with a single antenna. Here, node S directly communicates with node D_1. It is assumed that the direct link between node S and D_2 is absent [88]. Thus, S seeks relay cooperation from node I to communicate with its far-user D_2. As the IoT-transmitter node I is energy-constrained, it first harvests energy from the received RF signal from node S and then splits the corresponding received power to relay the primary signal and to transmit its own signal.

The channel coefficient and distance between any two nodes j and k are represented by h_{jk} and d_{jk}, respectively, with $j \in (S, I)$, $k \in (D_1, I, D_2, R)$, and $j \neq k$. It

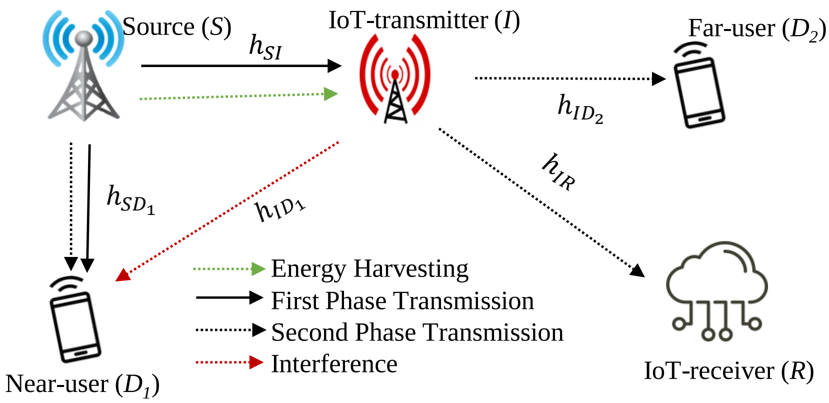

Figure 5.1: System model.

is assumed that all the channels experience Rayleigh fading except the channel h_{SD_1} which follows Rician distribution due to the viability of a line-of-sight (LoS) link. Therefore, $|h_{jk}|^2$, for $j \in (S, I)$, $k \in (I, D_2, R)$, $j \neq k$, is an exponential random variable (RV) with mean $\lambda_{jk} = d_{jk}^{-\nu}$, where ν denotes the path-loss exponent and $|h_{SD_1}|^2$ is a non-central chi-square distributed RV with mean $\lambda_{SD_1} = d_{SD_1}^{-\nu}$. Under statistical channel state information, it is assumed that the average channel powers associated with links $j \to k$, $j \in (S, I)$, $k \in (I, D_2, R)$, $j \neq k$ are ordered as $\lambda_{SI} < \lambda_{SD_1}$ and $\lambda_{ID_1} < \lambda_{IR} < \lambda_{ID_2}$, without loss of generality [104][1]. The PDF and CDF of $W \triangleq |h_{SD_1}|^2$ are given, respectively, by $f_W(w) = \phi e^{-(\phi w + K)} I_0\left(2\sqrt{\phi K w}\right)$ and $F_W(w) = 1 - Q_1\left(\sqrt{2K}, \sqrt{2\phi w}\right)$, where $\phi = \frac{(1+K)}{\lambda_{SD_1}}$, K is the Rician K-factor, $I_0(\cdot)$ is the modified Bessel function of the first kind [95, eq. 8.447], and $Q_1(\cdot,\cdot)$ is the Marcum-Q function [101, eq. 4.10]. All the links are inflicted by AWGN with mean zero and variance σ^2. The overall communication occurs in two phases over a transmission block of duration T as described in the sequel.

5.1.1 First Phase Transmission

For the first phase transmission of duration $T/2$ (denoted by t_1), source node S broadcasts the superimposed signal $X_S = \sum_{m=1}^{2} \sqrt{\alpha_m P_s} x_m$ towards D_1 and node I. Here, P_s denotes the source's transmit power, x_m is the intended signal for D_m, α_m is the PAF, $m \in (1, 2)$, with $\sum_{m=1}^{2} \alpha_m = 1$ and $\alpha_2 > \alpha_1$. Thus, the signal received at node k, $k \in (D_1, I)$, can be given by

$$y_{Sk}^{t_1} = h_{Sk} X_S + n_{Sk}, \tag{5.1}$$

[1]The decoding method adopted in this work is based on the average power λ_{jk}, i.e., on the distance. Although, this is not a standard approach, it may have some practical feasibility [104].

where n_{Sk} is the AWGN variable. Following the NOMA principle, D_1 first decodes signal x_2 assuming x_1 as noise, and then applies SIC to decode signal x_1. Thus, the SINRs at D_1 to decode x_2 and x_1, respectively, are given by

$$\gamma_{S\to D_1}^{x_2,t_1} = \frac{\alpha_2\rho_s|h_{SD_1}|^2}{\alpha_1\rho_s|h_{SD_1}|^2+1}, \tag{5.2}$$

$$\gamma_{S\to D_1}^{x_1,t_1} = \frac{\alpha_1\rho_s|h_{SD_1}|^2}{\psi_1\alpha_2\rho_s|h_{SD_1}|^2+1}, \tag{5.3}$$

where $\rho_s = P_s/\sigma^2$ is the transmit SNR, ψ_1 $(0 \le \psi_1 \le 1)$ is the residual interference parameter and $\psi_1 = 0$ denotes the pSIC case. However, the received signal at I is bifurcated as $\sqrt{\beta}y_{SI}^{t_1}$ for EH and $\sqrt{(1-\beta)}y_{SI}^{t_1}$ for information transmission, where $0 \le \beta \le 1$ represents the PS factor. The received signal for EH at node I can be expressed as

$$\sqrt{\beta}y_{SI}^{t_1} = \sqrt{\beta}h_{SI}X_s + \sqrt{\beta}n_{SI}. \tag{5.4}$$

From (5.4), the harvested energy at node I can be given by

$$E_h = \beta\mu\left(P_s\alpha_1 + P_s\alpha_2\right)|h_{SI}|^2T/2 = \beta\mu P_s|h_{SI}|^2T/2, \tag{5.5}$$

where μ $(0 < \mu \le 1)$ indicates the energy conversion efficiency, and the noise statistic is ignored [102]. Thus, the transmit power of node I for the remaining $T/2$ period can be given as $P_r = \frac{E_h}{T/2} = \beta\mu|h_{SI}|^2P_s$ while the received base-band signal at node R is given by

$$\sqrt{(1-\beta)}y_{SI}^{t_1} = \sqrt{(1-\beta)}h_{SI}\left(\sum_{m=1}^{2}\sqrt{\alpha_mP_s}x_m\right) + N_{SI}, \tag{5.6}$$

where $N_{SI} = \sqrt{(1-\beta)}n_{SI} + n_{RF}$, and n_{RF} is the sampled AWGN due to RF to base-band signal conversion . Thus, the SINR at I to decode x_2 can be expressed as

$$\gamma_{S\to I}^{x_2,t_1} = \frac{\alpha_2(1-\beta)\rho_s|h_{SI}|^2}{\alpha_1(1-\beta)\rho_s|h_{SI}|^2+1}. \tag{5.7}$$

5.1.2 Second Phase Transmission

In the next $T/2$ time period (denoted by t_2), upon successful decoding of x_2, node I combines its own signal x_i with x_2 as $X_I = \sqrt{\alpha_3P_r}x_i + \sqrt{\alpha_4P_r}x_2$, where x_i and

x_2 are intended signals for R and D_2 respectively, α_3 and α_4 are PAFs. Here, we assume that $d_{IR} > d_{ID_2}$, yielding $\alpha_3 > \alpha_4$ and $\alpha_3 + \alpha_4 = 1$. Thus, the signal received at node p, $p \in (R, D_2)$, can be written as

$$y_{Ip}^{t_2} = h_{Ip} X_I + n_{Ip}. \tag{5.8}$$

Herein, signal x_i is directly decoded at node R and SIC is conducted at D_2 to decode x_2. Thus, the received SINR to decode x_i at node R can be given as

$$\gamma_{I \to R}^{x_i, t_2} = \frac{\alpha_3 \beta \mu \rho_s |h_{SI}|^2 |h_{IR}|^2}{\alpha_4 \beta \mu \rho_s |h_{SI}|^2 |h_{IR}|^2 + 1}. \tag{5.9}$$

After applying the SIC, the end-to-end SINRs to decode x_i and x_2 at D_2 can be expressed, respectively, as

$$\gamma_{I \to D_2}^{x_i, t_2} = \frac{\alpha_3 \beta \mu \rho_s |h_{SI}|^2 |h_{ID_2}|^2}{\alpha_4 \beta \mu \rho_s |h_{SI}|^2 |h_{ID_2}|^2 + 1}, \tag{5.10}$$

$$\gamma_{I \to D_2}^{x_2, t_2} = \frac{\alpha_4 \beta \mu \rho_s |h_{SI}|^2 |h_{ID_2}|^2}{\psi_2 \alpha_3 \beta \mu \rho_s |h_{SI}|^2 |h_{ID_2}|^2 + 1}, \tag{5.11}$$

where ψ_2 $(0 \le \psi_2 \le 1)$ is the residual interference parameter.

In order to maximize spectrum utilization, source S simultaneously transmits the new signal $\hat{x}_1$ to D_1 with transmit power $\sqrt{\alpha_1^* P_s}$, for $\alpha_1^* \in (0,1)$, during the second phase. However, during the second phase transmission, D_1 experiences some interference from node I, which can be estimated and partially eliminated by using the side information of x_2 that is obtained during the SIC process in the first phase transmission. Therefore, the signal received during the second phase at D_1 can be given as

$$y_{SD_1}^{t2} = \sqrt{\alpha_1^* P_s} h_{SD_1} \hat{x}_1 + h_{ID_1} X_I + n_{SD_1}, \tag{5.12}$$

and the corresponding SINR, after partial interference cancellation can be expressed as

$$\gamma_{S \to D_1}^{\hat{x}_1, t_2} = \frac{\alpha_1^* \rho_s |h_{SD_1}|^2}{\alpha_3 \mu \beta \rho_s |h_{SI}|^2 |h_{ID_1}|^2 + 1}. \tag{5.13}$$

5.2 Performance Analysis

Considering the target data rates R_{d_1}, R_{d_2}, and R_r for D_1, D_2, and R, respectively, we execute the performance analysis of the proposed EH-based CDRT-NOMA system as follows.

5.2.1 OP Analysis

Near-User D_1

In the first phase, D_1 is said to be in outage if it is unable to decode either of the symbols x_1 or x_2. Hence, its OP expression is given by

$$P_{D_1}^{\mathrm{out},t_1} = 1 - \Pr\left[\gamma_{S\to D_1}^{x_2,t_1} > \gamma_{D_2}, \gamma_{S\to D_1}^{x_1,t_1} > \gamma_{D_1}\right], \tag{5.14}$$

where $\gamma_{D_1} = 2^{2R_{d_1}} - 1$ and $\gamma_{D_2} = 2^{2R_{d_2}} - 1$. By substituting the involved SINRs from (5.2) and (5.3) in (5.14), and performing some algebraic manipulations, $P_{D_1}^{\mathrm{out},t_1}$ can be expressed as

$$P_{D_1}^{\mathrm{out},t_1} = 1 - \Pr\left[|h_{SD_1}|^2 > \frac{\max\{\mathcal{A}_1, \mathcal{A}_2\}}{\rho_s}\right], \tag{5.15}$$

where $\mathcal{A}_1 = \frac{\gamma_{D_2}}{\alpha_2 - \alpha_1\gamma_{D_2}}$ and $\mathcal{A}_2 = \frac{\gamma_{D_1}}{\alpha_1 - \psi_1\alpha_2\gamma_{D_1}}$. Under the conditions $\frac{\alpha_2}{\alpha_1} > \gamma_{D_2}$ and $\frac{\alpha_1}{\psi_1\alpha_2} > \gamma_{D_1}$, (5.15) can be further re-expressed and evaluated as

$$P_{D_1}^{\mathrm{out},t_1} = \Pr\left[W \le \Delta_1/\rho_s\right] = 1 - Q_1\left(\sqrt{2K}, \sqrt{2\phi\Delta_1/\rho_s}\right), \tag{5.16}$$

where $\Delta_1 \triangleq \max\{\mathcal{A}_1, \mathcal{A}_2\}$. At high SNR ($\rho_s \to \infty$), the asymptotic expression for $P_{D_1}^{\mathrm{out},t_1}$ can be obtained by making use of [103, eq. 9.6.7] and the following approximation $e^{-x} \simeq 1 - x$ for small x in (5.16). It can be given by

$$P_{D_1,asy}^{\mathrm{out},t_1} = \phi e^{-K}\Delta_1/\rho_s. \tag{5.17}$$

In the second phase transmission, the OP for D_1 is given by

$$P_{D_1}^{\mathrm{out},t_2} = \Pr\left[\gamma_{S\to D_1}^{\hat{x}_1,t_2} < \gamma_{D_1}\right]. \tag{5.18}$$

By substituting (5.13) in (5.18), and after doing some mathematical re-arrangement, $P_{D_1}^{\text{out},t_2}$ can be written as

$$P_{D_1}^{\text{out},t_2} = \Pr\left[W < \mathcal{B}_1 XV + \mathcal{B}_2\right], \tag{5.19}$$

with $V \triangleq |h_{ID_1}|^2$, $X \triangleq |h_{SI}|^2$, $\mathcal{B}_1 = \frac{\gamma_{D_1}\alpha_3\beta\mu}{\alpha_1^*}$ and $\mathcal{B}_2 = \frac{\gamma_{D_1}}{\alpha_1^*\rho_s}$.

Theorem 5. *The expression of $P_{D_1}^{out,t_2}$ in (5.19) can be given by*

$$P_{D_1}^{out,t_2} = 1 - \sum_{l=0}^{\infty}\sum_{m=0}^{l}\sum_{n=0}^{m}\binom{m}{n}\frac{\mathcal{B}_2^{m-n}K^l n!\mathcal{B}_1^n\phi^m e^{-K}}{l!m!\lambda_{SI}\lambda_{ID_1}}\frac{e^{-\phi\mathcal{B}_2}e^{-\Theta_1\Theta_2}}{(\phi\mathcal{B}_1)^{n+1}}\sum_{j=0}^{n}\binom{n}{j}(-\Theta_2)^{n-j}$$
$$\times\left[(-1)^{n-j+1}\Theta_1^{n-j}\frac{\mathrm{Ei}(\Theta_1\Theta_2)}{(n-j)!} + \frac{e^{-\Theta_1\Theta_2}}{\Theta_2^{n-j}}\sum_{k=0}^{n-j-1}\frac{(-1)^k(\Theta_1\Theta_2)^k k!}{(n-j-k)!}\right], \tag{5.20}$$

where $\Theta_1 = \frac{1}{\phi\mathcal{B}_1\lambda_{ID_1}}$, $\Theta_2 = \frac{1}{\lambda_{SI}}$, and $\mathrm{Ei}(\cdot)$ is the exponential integral function [95, eq. 8.211].

Proof. See Appendix J. ∎

By following the same steps of derivation used to compute (5.20) in Appendix J and by making use of [103, eq. 9.6.7] and the approximation $e^{-x} \simeq 1 - x$ for small x, we derive the asymptotic expression for $P_{D_1}^{\text{out},t_2}$ in the high-SNR regime as

$$P_{D_1,asy}^{\text{out},t_2} = \phi e^{-K}\left(\frac{\gamma_{D_1}^{\text{th}}}{\alpha_1^*\rho_s} + \frac{1}{\lambda_{SI}\lambda_{ID_1}}\right). \tag{5.21}$$

Far-User D_2

The outage event for D_2 takes place either when the IoT-transmitter node I is unable to decode the symbol x_2 or when the node D_2 is unable to detect any symbol in conjunction with the successful detection of x_2 at node I. Hence, the OP expression for D_2 can be given as

$$P_{D_2}^{\text{out},t_2} = \Pr\left[\gamma_{S\to I}^{x_2,t_1} < \gamma_{D_2}\right] + \Pr\left[\gamma_{S\to I}^{x_2,t_1} \geq \gamma_{D_2}, \overline{P}_{SD_2}\right], \tag{5.22}$$

where $\overline{P}_{SD_2}$ signifies probability of failure to detect any symbol at D_2 and can be given as

$$\overline{P}_{SD_2} = 1 - \Pr\left[\gamma_{I\to D_2}^{x_i,t_2} > \gamma_R, \gamma_{I\to D_2}^{x_2,t_2} > \gamma_{D_2}\right], \tag{5.23}$$

where $\gamma_R = 2^{2R_r} - 1$. After substituting the respective SINRs in (5.23) and with some mathematical re-arrangement, we get

$$\overline{P}_{SD_2} = 1 - \Pr\left[|h_{ID_2}|^2 > \frac{\max\{\mathcal{A}_3, \mathcal{A}_4\}}{|h_{SI}|^2\rho_s}\right] = \Pr\left[Y \leq \frac{\Delta_2}{X\rho_s}\right], \tag{5.24}$$

where $\Delta_2 \triangleq \max\{\mathcal{A}_3, \mathcal{A}_4\}$, $\mathcal{A}_3 = \frac{\gamma_R}{(\alpha_4 - \psi_2\alpha_3\gamma_R)\beta\mu}$, $\mathcal{A}_4 = \frac{\gamma_{D_2}}{(\alpha_3 - \alpha_4\gamma_{D_2})\beta\mu}$, and $Y \triangleq |h_{ID_2}|^2$ with condition $\frac{\alpha_4}{\psi_2\alpha_3} > \gamma_R$ and $\frac{\alpha_3}{\alpha_4} > \gamma_{D_2}$. One can deduce permissible range of PAF from these imposed constraints to maintain QoS of primary users as $\frac{\gamma_{D_2}}{1+\gamma_{D_2}} < \alpha_3 < \frac{1}{1+\psi_2\gamma_R}$. By inserting (5.24) into (5.22), one can derive the expression for $P_{D_2}^{\text{out},t_2}$ as given in the following theorem.

Theorem 6. *The analytical expression for $P_{D_2}^{out,t_2}$, conditioned over $\frac{\alpha_2}{\alpha_1} > \gamma_{D_2}$, can be given by*

$$P_{D_2}^{out,t_2} = 1 - \sum_{l=0}^{\infty} \frac{(-1)^l}{l!} \left(\frac{\Delta_2}{\lambda_{ID_2}\rho_s}\right)^l \frac{1}{\lambda_{SI}} \left(\frac{\mathcal{A}_5}{\rho_s}\right)^{1-l} \mathrm{E}_l\left(\frac{\mathcal{A}_5}{\lambda_{SI}\rho_s}\right), \tag{5.25}$$

where $\mathcal{A}_5 = \frac{\gamma_{D_2}}{(\alpha_2 - \alpha_1\gamma_{D_2})(1-\beta)}$ and $\mathrm{E}_l(\cdot)$ is the l-th order exponential integral function [103, eq. 5.1.1].

Proof. See Appendix K. ■

Furthermore, with the use of approximation $e^{-x} \simeq 1-x$ for small x and following the similar steps used to derive (5.25) in Appendix (K), the asymptotic expression for $P_{D_2}^{\text{out},t_2}$ at high SNR can be obtained as

$$P_{D_2,asy}^{\text{out},t_2} = \frac{\mathcal{A}_5}{\lambda_{SI}\rho_s} - \left(\frac{\Delta_2}{\lambda_{ID_2}\lambda_{SI}\rho_s}\right) \mathrm{Ei}\left(-\frac{\mathcal{A}_5}{\lambda_{SI}\rho_s}\right). \tag{5.26}$$

IoT-Receiver R

The OP for R can be formulated as

$$P_R^{\text{out},t_2} = \Pr\left[\gamma_{S\to I}^{x_2,t_1} < \gamma_{D_2}\right] + \Pr\left[\gamma_{S\to I}^{x_2,t_1} \geq \gamma_{D_2}, \gamma_{I\to R}^{x_i,t_2} < \gamma_R\right]. \tag{5.27}$$

By invoking the respective SINRs in (5.27) with some algebraic manipulations, P_R^{out,t_2} can be expressed as

$$P_R^{\text{out},t_2} = \Pr\left[X < \frac{\mathcal{A}_5}{\rho_s}\right] + \Pr\left[X \geq \frac{\mathcal{A}_5}{\rho_s}, Z \leq \frac{\mathcal{A}_6}{X\rho_s}\right], \tag{5.28}$$

where $Z \triangleq |h_{IR}|^2$ and $\mathcal{A}_6 = \frac{\gamma_R}{(\alpha_3 - \alpha_4\gamma_R)\beta\mu}$. The analytical expression for P_R^{out,t_2} in (5.28), under the conditions $\frac{\alpha_2}{\alpha_1} > \gamma_{D_2}$ and $\frac{\alpha_3}{\alpha_4} > \gamma_R$, can be derived as given in subsequent theorem.

Theorem 7. *The analytical expression for P_R^{out,t_2} derived over Rayleigh fading channel can be given as*

$$P_R^{out,t_2} = 1 - \sum_{l=0}^{\infty} \frac{(-1)^l}{l!} \left(\frac{\mathcal{A}_6}{\lambda_{IR}\rho_s}\right)^l \frac{1}{\lambda_{SI}} \left(\frac{\mathcal{A}_5}{\rho_s}\right)^{1-l} \mathrm{E}_l \left(\frac{\mathcal{A}_5}{\lambda_{SI}\rho_s}\right). \tag{5.29}$$

Proof. By following the similar steps used to obtain (5.25) in Appendix (K), one can derive (5.29). ■

By following the analogous steps used to derive (5.26), one can obtain the asymptotic expression for P_R^{out,t_2} at high SNR as

$$P_{R,asy}^{\text{out},t_2} = \frac{\mathcal{A}_5}{\lambda_{SI}\rho_s} - \left(\frac{\mathcal{A}_6}{\lambda_{IR}\lambda_{SI}\rho_s}\right) \mathrm{Ei}\left(-\frac{\mathcal{A}_5}{\lambda_{SI}\rho_s}\right). \tag{5.30}$$

Remark 1: The infinite summation series in (5.20), (5.25), and (5.29) can be truncated to the first L terms such that the convergence error is kept to a bare minimum. For instance, the truncation accuracy of the summation limits L are listed below in Table 5.1, Table 5.2, and Table 5.3 for (5.20), (5.25), and (5.29), respectively. Herein, the parameters are taken as given in Section 5.4 with $\psi_2 = 0.1$, $\rho_s = 20$ dB, and $\rho_s = 30$ dB. It can be observed from Table 5.1 that the infinite summation limits of (5.20) can be truncated to $L = 20$ because $L > 20$ has no effect on the third decimal place of $P_{D_1}^{\text{out},t_2}$. From Table 5.2 and Table 5.3, one can observed that infinite summation limits in (5.25), and (5.29) converges early at lower SNR (ρ_s) for $L = 30$ but at high SNR it takes more terms to converge. Therefore, to minimize the convergence error and to get more accurate value, we have considered first 40 terms.

Table 5.1: Truncation accuracy for $P_{D_1}^{\text{out},t_2}$ evaluation in (5.20).

L	$\rho_s = 20$ dB	$\rho_s = 30$ dB
15	0.212268	0.192431
20	0.259471	0.254354
25	0.259213	0.254351
30	0.259210	0.254356

Table 5.2: Truncation accuracy for $P_{D_2}^{\text{out},t_2}$ evaluation in (5.25).

L	$\rho_s = 20$ dB	$\rho_s = 30$ dB
15	0.0182314	0.001417
20	0.0203116	0.001649
25	0.0203141	0.002162
30	0.0203112	0.002176

Table 5.3: Truncation accuracy for P_{R}^{out,t_2} evaluation in (5.29).

L	$\rho_s = 20$ dB	$\rho_s = 30$ dB
15	0.016451	0.001977
20	0.021120	0.002231
25	0.022143	0.002652
30	0.025164	0.0028413
35	0.025121	0.0028641

Remark 2: Using the definition of the diversity gain, the asymptotic OP expressions in (5.17) and (5.21) imply that the diversity order of D_1 is one in the first phase and zero in the second phase (this can be explained intuitively by the fact that D_1 faces interference from the secondary transmission during the second phase). As for the asymptotic OP expressions in (5.26) and (5.30), with the aid of the following approximation $\text{Ei}(x) \approx C + \ln(-x) + x$ for small x (where C is the Euler's constant), it can be inferred that the diversity order is one for both D_2 and R.

5.2.2 System Throughput

For a relay based wireless network, the system throughput is a measure of the average SE. The system throughput for the proposed EH-based CDRT-NOMA system is evaluated as the total of individual target rates for both primary and secondary communications that can be attained successfully over Rician/Rayleigh fading channels. It can be formulated as

$$\mathcal{S}_{\mathcal{T}} = \frac{1}{2}\Big[\big(1 - P_{D_1}^{\text{out},t_1}\big) r_{d_1} + \big(1 - P_{D_1}^{\text{out},t_2}\big) R_{d_1} \\ + \big(1 - P_{D_2}^{\text{out},t_2}\big) R_{d_2} + \big(1 - P_{R}^{\text{out},t_2}\big) R_r\Big]. \tag{5.31}$$

5.2.3 Energy Efficiency

The EE is measured as the ratio of total data delivered to the total power consumed by the proposed system. It can be given as

$$\Xi_{\mathcal{E}} = \frac{\mathcal{S}_{\mathcal{T}}}{P_s/2}, \tag{5.32}$$

where $\mathcal{S}_{\mathcal{T}}$ is the achievable throughput as expressed in (5.31).

5.3 Deep Learning Architecture

Here, we develop a DNN model to predict the OP and ESC of the system. As the conventional approaches and Monte-Carlo simulations to calculate the OP and ESC are intractable and cumbersome, respectively, this DNN model will help to predict OP and ESC in a short time and with less computational complexity.

5.3.1 Dataset Generation

The following set of parameters have been taken as input for the proposed DNN model: source power $P_s \in [0, 40]$ dB, PS factor $\beta \in [0.01, 0.99]$, dual PAFs $\alpha_1 \in [0, 0.49]$ and $\alpha_3 \in [0.5, 0.99]$, the corresponding residual interference coefficients $\psi_1 \in [0, 0.1]$ and $\psi_2 \in [0, 0.1]$, and the target data rates $R_{d_1} \in [0.25, 1]$, $R_{d_2} \in [0.25, 0.8]$, and $R_r \in [0.25, 0.8]$. The model has been trained over 120,000 data points, where 80% of the points are used for training, and the remaining 20% are used for validation and testing.

5.3.2 Description of DNN Model

The proposed framework for DL evaluation includes the training and prediction phases, as shown in Fig. 5.2. In the training phase, the DL model learns the input-output relation of the considered system setup, where the adaptive moment estimation (Adam) optimization algorithm is used for minimizing the loss function in the back-propagation process. In the prediction phase, the resulting DL model obtained from the training phase is utilized to predict the OP/ESC value whenever any new information is available at the input of the deep model.

5.3.3 DNN learning model

We design a DNN model as a regression problem to evaluate the OP/ESC performance. The architecture of the DNN is illustrated in Fig. 5.3. At each hidden layer, we use an exponential linear unit (eLU) activation function to execute a threshold operation for every input parameter $\mathcal{I}$, where the operation of eLU can be presented as follows:

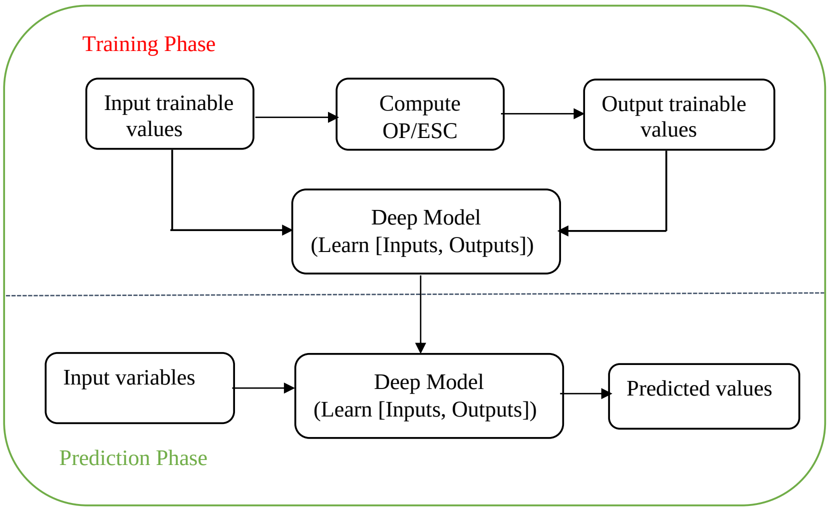

Figure 5.2: Illustrations of deep model training and prediction phases.

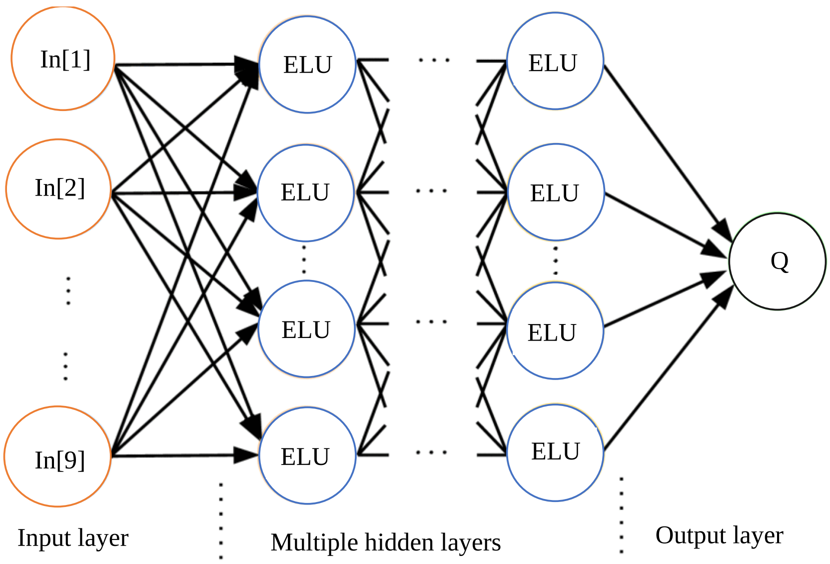

Figure 5.3: Illustrations of the DNN architecture.

$$\mathrm{eLU}(\mathcal{I}) = \begin{Bmatrix} \varphi\left(e^{\mathcal{I}}-1\right), & \text{if } \mathcal{I} < 0 \\ \mathcal{I}, & \text{if } \mathcal{I} \geq 0 \end{Bmatrix}. \tag{5.33}$$

where φ is a constant value initialized to 1. There is one neuron at the output layer since the regression problem directly predicts numerical values without any further transformation and activation function. We consider four fully connected layers with 100 hidden neurons per layer, where the activation $\mathcal{T}_l^j$ of the l-th neuron in the j-th layer is linked with activations in the $(j-1)$-th layer according to the following expression:

$$\mathcal{T}_l^j = \text{eLU}\left(\sum_{t=1}^{Z_{j-1}} \Lambda_{l,t}^j \mathcal{T}_t^{j-1} + \mathcal{S}_l^j\right), \tag{5.34}$$

where Z_{j-1} denotes the neuron quantity in the $(j-1)$-th layer, $\Lambda_{l,t}^j$ represents the weight linking to the t-th neuron in the $(j-1)$ layer, and finally $\mathcal{S}_l^j$ is a scalar bias at the j-th layer.

5.3.4 Real-time Prediction

The Adam optimization algorithm is employed for the considered deep model to calculate/update the weights and biases during the back-propagation procedure. This is because Adam demonstrates superior performance gains in terms of the training speed compared to other learning optimization algorithms (e.g., stochastic gradient descent, momentum, nesterov accelerated gradient, RMSProp). Let Q^v and $\bar{Q}^v$ denote the actual and predicted output values of the deep model accommodating the v-th testing sample, respectively. The loss function representing the mean-square error between the estimated and predicted values can be calculated as follows:

$$Loss\left(Q^v, \bar{Q}^v\right) = \frac{1}{\mathcal{V}} \sum_{v}^{\mathcal{V}} \left(Q^v - \bar{Q}^v\right)^2. \tag{5.35}$$

After finishing the training phase, the resulting deep learning model including weights and biases can be symbolized via a compact mapping function $\mathcal{F}(\cdot)$. The resulting deep model will output a predicted OP/ESC value whenever any new information is available at the input. The input information was arranged as a vector $x \triangleq [P_s, \beta, \alpha_1, \alpha_3, \psi_1, \psi_2, R_{d_1}, R_{d_2}, R_r]$. The predicted process can be expressed as

$$\bar{Q} = \mathcal{F}(x). \tag{5.36}$$

As a result, the i-th training samples can be represented as $\mathbf{z}_i = \left[\mathbf{x}_i, \mathbf{y}_i^1, \ldots, \mathbf{y}_i^t, \ldots, \mathbf{y}_i^T\right]$ where $\mathbf{y}_i^t$ denote the target outputs, i.e., OP/EC of different users for the i-th sample and the training set $z = \{z_1, z_2, ...\}$. T is the total of the the target outputs. Through a low-latency inference process in (5.36), the OP/ESC can be predicted by the resulting deep model. We evaluate the performance of the proposed DL approaches in terms of the RMSE and runtime prediction. The RMSE is considered to determine the difference between the forecast value and the actual output value across the overall test set, which can be calculated as follows:

$$\mathrm{RMSE} = \sqrt{\frac{1}{\mathcal{V}} \sum_{v}^{\mathcal{V}} \left(Q^v - \bar{Q}^v\right)^2}, \tag{5.37}$$

where $\mathcal{V}$ is the total samples in the test set. It is noted that the complexity of our approach mainly relies on the training data set generation while the computational cost during the estimating process is measured by the number of floating point operations. Our model has a computation cost of 31,101 trainable parameters. The detailed algorithm for DL approach is depicted in Algorithm 2.

Algorithm 2: Procedure of training and testing DL approach

Input: Initialize the DL model and input parameters
$\mathbf{x} = [P_s, \beta, \alpha_1, \alpha_3, \psi_1, \psi_2, R_{d_1}, R_{d_2}, R_r]$.

Output: Set a target output $\mathbf{y}_i^t, t \in \{1, ..., T\}$, from vector
$\mathbf{z}_i = \left[\mathbf{x}_i, \mathbf{y}_i^1, \ldots, \mathbf{y}_i^t, \ldots, \mathbf{y}_i^T\right]$

Network: Set the key parameters: hidden layer, neuron per layer, activation, kernel, learning rate, epochs, and output functions of the hidden and output layers.

while *the number of epochs are less than the setting target* **do**

  Implement the forward DL process and attain the result of the output layer's data, denoted as $\mathbf{y}_{\text{out}}^t$.

  Calculate the loss function, that is, the mean square error over the test set $Loss\left(\mathbf{y}_i^t, \mathbf{y}_{\text{out}}^t\right) = \frac{1}{\mathcal{V}} \sum_v^{\mathcal{V}} \left(\mathbf{y}_i^{t,v} - \mathbf{y}_{\text{out}}^{t,v}\right)^2$.

  Compute the corrective parameter with the Adam optimization algorithm and update the parameters with the algorithm to search for the optimal solution.

end

Test the trained DL with the test data and plot the training and validation curve.

Save the trained output associating input parameters into a defined file " .h5"

5.4 Numerical Results

This section presents the numerical findings illustrating the performance of the proposed system. The analytical results are verified by Monte-Carlo simulations. We have also included the DNN model results here. The following parameters set [88] is used throughout this section, if not mentioned specifically: $\alpha_1 = 0.3$, $\alpha_3 = 0.8$, $\alpha_1^* = 1$, $\beta = 0.3$, $\mu = 0.7$, and $\sigma^2 = 1$. Considering the 2-dimensional (x, y) plane, the positions for nodes S, D_1, I, D_2, and R are given as $(0, 0)$, $(0, -0.3)$, $(0.4, 0)$, $(0.5, 0)$, and $(-0.2, -0.45)$, respectively.

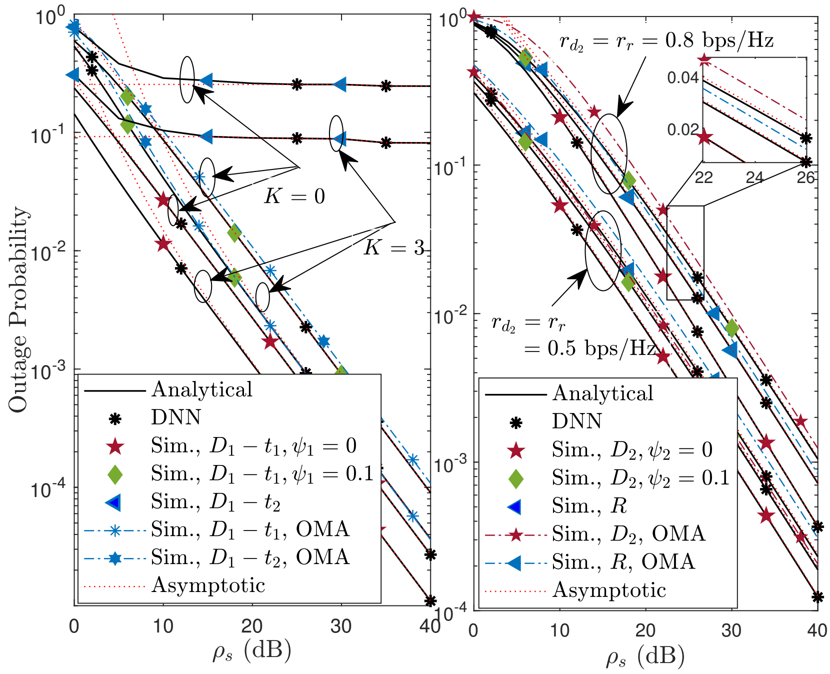

Figure 5.4: OP of D_1, D_2 and R versus SNR.

Fig. 5.4 depicts the OP performance versus the transmit SNR (ρ_s) for D_1, D_2, and R under the pSIC and ipSIC cases. Herein, we set the parameters as $R_{d_1} = 1$ bps/Hz, $R_{d_2} = R_r = \{0.5, 0.8\}$ bps/Hz. It can be seen from the curves that our simulation results are well aligned with the analytical ones as well as the DNN predictions. For D_1, when we increase the Rician-K factor from 0 to 3, the OP performance improves. This is expected since the viability of the LoS increases with K. For D_2 and R, as the target rate ($R_{d_2} = R_r$) increases from 0.5 to 0.8 bps/Hz, the outage performance degrades. It is also worth noting that when we increase the level of residual interference parameter, the performance of D_1 and D_2 deteriorates. It indicates that the decoding capability of D_1 and D_2 decreases with an increase in ipSIC level. Further, the OP of the proposed EH-based CDRT-NOMA system

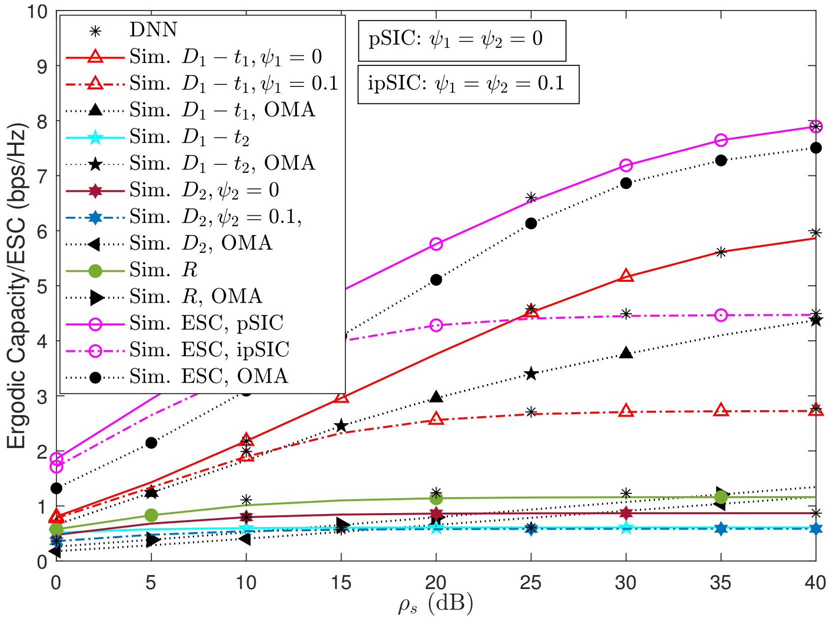

Figure 5.5: EC/ESC versus SNR.

model is compared with the OMA equivalent, which clearly shows the superiority of the former over the latter. In addition, for all the users, the asymptotic curves attained from derived expressions and the corresponding simulated ones overlap in high-SNR regions, which corroborates the proposed asymptotic analysis.

Fig. 5.5 depicts the EC versus transmit SNR (ρ_s) curves for D_1, D_2, and R under both the pSIC and ipSIC cases. We observe that as SNR increases, the EC of the system improves. The results demonstrate that the ESC of our proposed system achieves better performance in comparison to its OMA equivalent in the case of pSIC. In addition, it demonstrates that the simulation and DNN prediction results are highly congruent, validating our deep learning framework.

In Fig. 5.6, we plot throughput of the proposed system as a function of ρ_s for both pSIC and ipSIC cases under the parameter setting $R_{d_1} = 1$ bps/Hz, $R_{d_2} = R_r = \{0.5, 0.8\}$ bps/Hz, $K = 3$, with different values of PS factor $\beta = 0.2, 0.5$. We can see that the system throughput increases for lower to medium range of SNR, and subsequently gets saturated, reflecting the maximum attainable throughput for the specific data rate. For the higher data rate, it attains its maximum at relatively high SNR. It happens because the outage performance at a higher target rate is relatively poorer than the lower target rate.

In Fig. 5.7, we plot the EE of the proposed system as a function of ρ_s for both pSIC and ipSIC cases with the same set of parameters as the ones used in Fig. 5.6. We observe that the EE first increases as ρ_s increases from lower to medium region.

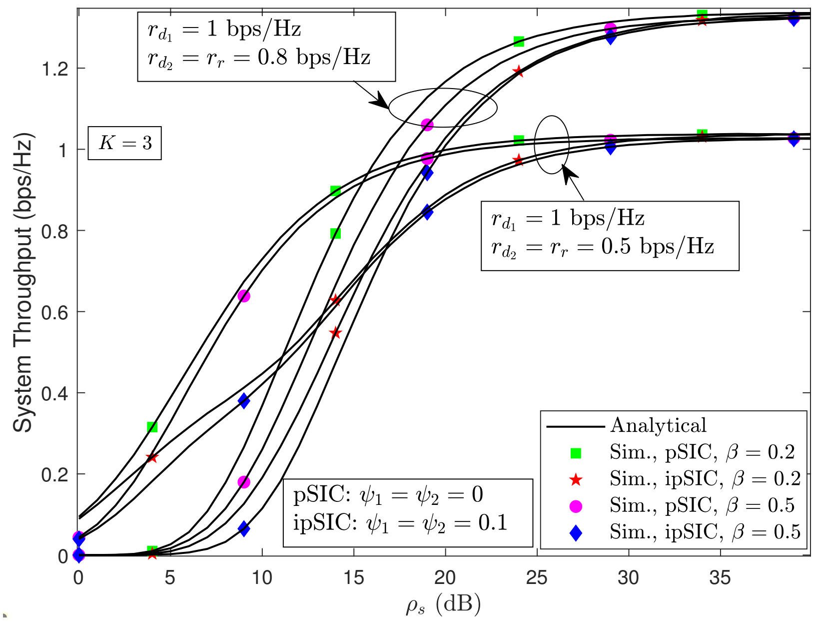

Figure 5.6: System throughput versus SNR.

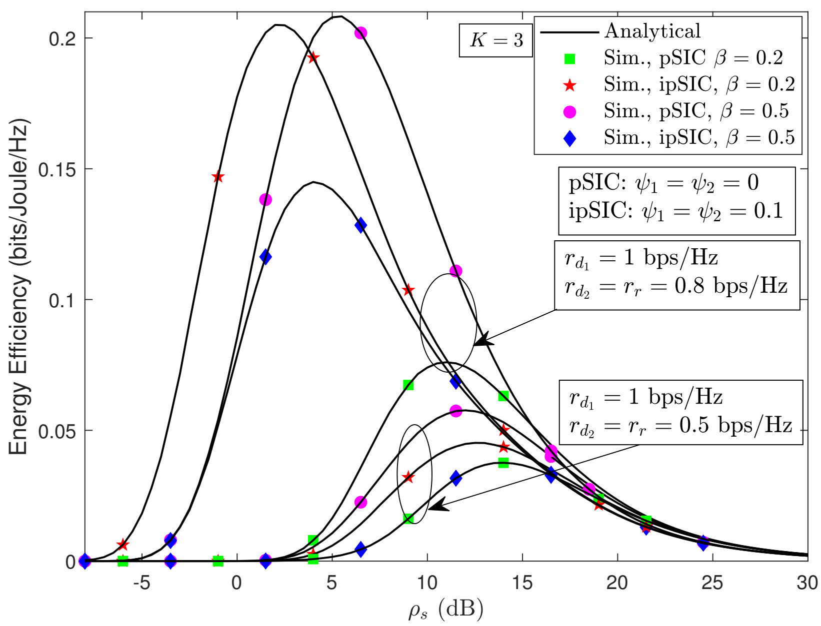

Figure 5.7: Energy efficiency versus SNR.

For higher SNR regime, the EE of both pSIC and ipSIC starts to decay and to converge because of the higher power consumption of the network.

Moreover, we compare the execution time taken by the Monte-Carlo simulation and the DNN for ESC evaluation. It is noted that the DNN prediction takes 0.0175 seconds, compared to 4.95 seconds for the Monte-Carlo simulation. Also, the proposed DL framework has the lowest RMSE of 1.43×10^{-3}. One can observe hereby that the DL framework exhibits a low execution time as compared to the Monte-Carlo simulation to evaluate the ESC, which helps to explore real-time configurations for the proposed system.

5.5 Summary

In this chapter, we investigated an EH-based CDRT-NOMA system that improves spectral and energy efficiency. We evaluated the performance of the proposed system in terms of OP, EC/ESC, system throughput, and EE for both the pSIC and ipSIC cases. The proposed EH-based CDRT-NOMA system achieved notable performance improvements in terms of OP/ESC as compared to OMA equivalent. Asymptotic OP expressions are also examined to provide useful insights into the achievable diversity order. A DL framework was designed to predict the OP/ESC performance with low complexity and low-latency processes in practical future networks while avoiding complex closed-form analytical expressions. Although the present work constitutes an advancement to the current state-of-the-art, it can be further extended to other emerging wireless systems, e.g., massive multiple input multiple output (MIMO)-based systems. These systems can be considered as they add another degree of complexity inherent to channel estimation, pilot contamination, precoding, user scheduling and signal detection.

CHAPTER 6

CONCLUSIONS AND FUTURE WORKS

This chapter summarizes the contributions presented in this thesis and provides possible extensions for future works.

6.1 Conclusions

This thesis presented a comprehensive performance evaluations of overlay cognitive systems with various energy- and spectral-efficient schemes. Specifically, the thesis provided various system designs for futuristic wireless networks that can make efficient use of precious energy and spectrum resources. This thesis draws the following conclusions:

- Firstly, we have studied the EH-based overlay CR-WBAN, where both the primary (medical sensors) and secondary (motion sensors) communications are realized on the human body through a cooperative spectrum sharing technique. We employed two EH-based spectrum sharing cooperation protocols, called TSC and PSC protocols for the considered network, and analyzed their performance in terms of OP, throughput and energy efficiency over the pertinent log-normally distributed fading channels. Our results reveal that the PSC protocol notably outperforms the TSC protocol and thereby explores more spectrum sharing opportunities in the proposed CR-WBAN. Furthermore, the impact of key parameters are highlighted to provide useful insights into the practical design of spectral and energy-efficient WBANs for smart healthcare applications.

- Then, we examined the performance of an EH-OCNOMA system over the Nakagami-m fading channel, wherein an energy-constrained ST node has been assumed to cooperate with the primary signal transmission while simultaneously transmitting its own information using the NOMA principle. For this, we proposed two CSS schemes based on IR protocol using the AF and DF relaying strategies, viz., CSS-IAF and CSS-IDF, and compared their performance with the conventional FR-based AF and DF relaying schemes, DLT scheme, and OMA scheme. The proposed schemes have significantly improved the performance of both primary and secondary networks over the baseline schemes, as the proposed schemes efficiently utilize the available spectrum resources to improve the system performance. Further, to get more insight, we examined the system throughput and EE for the considered EH-OCNOMA system. Above all, a comparison with FR-based schemes reveals that the proposed schemes can support relatively higher data rates till the occurrence of the RCC effect. Further, the CSS-IDF scheme illustrates comparatively better performance than its CSS-IAF counterpart. Additionally, the performance of secondary network is significantly improved for the CSS-IDF scheme.

- Next, different from the above discussed works, we examined a SWIPT enabled IoT-based overlay CNOMA-CDRT system that improves spectrum utilization and EE . We evaluated the performance of the proposed system in terms of OP, system throughput and EE by deriving the analytical expressions, which are calculated over Nakagami-m fading for both the pSIC and the ipSIC cases. Moreover, we proposed an iterative algorithm to minimize a user's OP over an optimal TS factor to further improve the performance of the proposed system.

- Lastly, we explored the deep learning approach along with model- based approach to evaluate the performances of an EH-based CDRT-NOMA system. We evaluated the performance of the proposed system in terms of OP, EC/ESC, system throughput, and EE for both the pSIC and ipSIC cases. The proposed EH-based CDRT-NOMA system achieved notable performance improvement in terms of OP/ESC as compared to OMA equivalent. Asymptotic OP expressions are also examined to provide insights into the achievable diversity order.

6.2 Future Works

With emerging wireless communication, numerous open problems could be addressed in future research related to the topics of this thesis, which can be briefly outlined as follows:

- The sensors in CR-WBAN function round the clock, collecting body vitals and transferring these through appropriate communication protocols to the back end cloud. There are two major resource throttling points in this scenario: 1) the sensors are extremely resource constrained devices and a major part of their energy is expended in transmitted signals round the clock; 2) the back end cloud comprises mobile devices such as personal digital assistants (PDAs), smart-phones, smart-watches, etc. Such devices are not geared to handle streaming data that arrive continuously from various sensors. To address these issues, one can propose learning algorithms specialized to effectively function in the resource constrained environs of a body sensor. Specifically, one can plan to implement an anomaly detection algorithm that will, at the site of sensor nodes, assess a body parameter and identify it to be an anomaly or not. Only a parameter identified as an anomaly will be transmitted beyond the sensor to the back end cloud. Non-anomalous signals indicating a normal body parameter will be discarded. Such a system is expected to significantly reduce the transmission energy expended at each sensor node and positively complement the EH endeavours of the work.

- It would be intriguing to execute the EH-OCNOMA system performance analysis while deploying the PT with multiple antennas and considering the spatial correlation among the communication links. Further, considering various non-linear electronic devices in the energy harvester circuitry, one can study a non-linear EH model for OCNOMA system. Nevertheless, our presented results will serve as a benchmark of the EH-OCNOMA system performance and provide useful guidelines for the design of 5G and beyond wireless networks.

- Moreover, with the advancement of deep learning algorithms and open-source artificial intelligence (AI)/machine learning (ML) tools, the use of AI/ML in wireless networks with wireless caching, is gaining increased attention. Thus, the development of novel ML-assisted resource management algorithms can serve as the main focus of future research to handle the issues posed by multi-dimensional and expansive search spaces.

APPENDIX A
DERIVATION OF (2.29)

Using (2.7), the CDF $F_{\gamma_{psq}}(x) = \Pr[\gamma_{psq} < x]$ is evaluated, for $x < \frac{\zeta}{1-\zeta}$, as

$$F_{\gamma_{psq}}(x) = \Pr\left[\gamma_{ps} < \frac{x(1+\zeta\beta_2|h_{sq}|^2)}{\beta_1(\zeta-(1-\zeta)x)|h_{sq}|^2}\right] \triangleq \phi(x), \tag{A.1}$$

and otherwise, for $x \geq \frac{\zeta}{1-\zeta}$, it is unity. We can further evaluate

$$\phi(x) = \int_0^\infty F_{\gamma_{ps}}\left(\frac{x(1+\zeta\beta_2 y)}{\beta_1(\zeta-(1-\zeta)x)y}\right) f_{|h_{sq}|^2}(y)dy. \tag{A.2}$$

On inserting the CDF of γ_{ps} using (2.21) and the PDF of $|h_{sq}|^2$ from (2.20) into (A.2), we get the result as presented in (2.29).

APPENDIX B

DERIVATION OF (2.33)

The CDF $F_{\gamma_{psr}}(x)$ is expressed using (2.31) as

$$F_{\gamma_{psr}}(x) = \Pr\left[\gamma_{ps} < \frac{x(1+\zeta\beta_1|h_{sr}|^2)}{(1-\zeta)\beta_2|h_{sr}|^2}\right], \tag{B.1}$$

which can be evaluated as

$$F_{\gamma_{psr}}(x) = \int_0^\infty F_{\gamma_{ps}}\left(\frac{x(1+\zeta\beta_1 y)}{(1-\zeta)\beta_2 y}\right) f_{|h_{sr}|^2}(y)dy. \tag{B.2}$$

On invoking the CDF of γ_{ps} using (2.21) and the PDF of $|h_{sr}|^2$ from (2.20) into (B.2), we get the result as presented in (2.33).

APPENDIX C

DERIVATIONS OF (3.28)

Referring to (3.7), the CDF $F_{\gamma_{psq}^{\mathrm{AF}}}(x) = \Pr\left[\gamma_{psq}^{\mathrm{AF}} < x\right]$ can be expressed as

$$\begin{aligned} F_{\gamma_{psq}^{\mathrm{AF}}}(x) &= \Pr\left[\frac{\zeta\gamma_{ps}\beta|h_{sq}|^2}{(1-\zeta)\gamma_{ps}\beta|h_{sq}|^2 + \zeta\beta|h_{sq}|^2 + 1} < x\right] \\ &= \Pr\left[\gamma_{ps} < \frac{x(1+\zeta\beta|h_{sq}|^2)}{\theta_x\beta|h_{sq}|^2}\right], \end{aligned} \tag{C.1}$$

which can be further evaluated as

$$F_{\gamma_{psq}^{\mathrm{AF}}}(x) = \int_0^\infty F_{\gamma_{ps}}\left(\frac{x(1+\zeta\beta y)}{\theta_x\beta y}\right) f_{|h_{sq}|^2}(y)dy. \tag{C.2}$$

With $\theta_x > 0$, on substituting the PDF $f_{|h_{sq}|^2}(\cdot)$ and the CDF $F_{\gamma_{ps}}(\cdot)$ using (3.19) and (3.20), respectively, and then solving by using the binomial expansion [95, eq. 1.111], we get $F_{\gamma_{psq}^{\mathrm{AF}}}(x)$ as given in (3.27) with $\phi_1(x)$ as

$$\begin{aligned} \phi_1(x) = 1 - &\sum_{k=0}^{m_{ps}-1}\sum_{j=0}^{k} \frac{1}{k!}\left(\frac{T_0 x}{\theta_x}\right)^k \mathrm{e}^{-\left(\frac{T_0 x\zeta\beta}{\theta_x}\right)} \left(\frac{m_{sq}}{\Omega_{sq}}\right)^{m_{sq}} \binom{k}{j} \\ &\times \frac{1}{\Gamma(m_{sq})}(\zeta\beta)^j \int_0^\infty y^{(m_{sq}+j-k)-1} \mathrm{e}^{-\frac{T_0 x}{\theta_x y} - \frac{m_{sq}}{\Omega_{sq}} y}. \end{aligned} \tag{C.3}$$

Finally, by computing the involved integral using [95, eq. 3.471.9], one can reach the desired result as provided in (3.28).

APPENDIX D

DERIVATIONS OF (3.51)

The CDF $F_{\gamma_{psr}^{\text{AF}}}(\gamma_s) = \Pr\left[\gamma_{psr}^{\text{AF}} < \gamma_s\right]$ can be expressed using (3.9) as

$$\begin{aligned} F_{\gamma_{psr}^{\text{AF}}}(\gamma_s) &= \Pr\left[\frac{(1-\zeta)\gamma_{ps}\beta|h_{sr}|^2}{\zeta\beta|h_{sr}|^2 + \zeta\beta\gamma_{ps}|h_R|^2 + 1} < \gamma_s\right] \\ &= \Pr\left[\gamma_{ps} < \frac{\gamma_s(1+\zeta\beta|h_{sr}|^2)}{|h_{sr}|^2\beta T_1 - \zeta\beta\gamma_s|h_R|^2}\right], \end{aligned} \tag{D.1}$$

which can be further evaluated as

$$F_{\gamma_{psr}^{\text{AF}}}(\gamma_s) = \int_0^\infty \left(\int_{\frac{\zeta\gamma_s z}{T_1}}^\infty \left(\int_0^{\frac{\gamma_s(1+\zeta\beta y)}{T_1\beta y - \zeta\beta\gamma_s z}} f_{\gamma_{ps}}(x)dx\right) f_{|h_{sr}|^2}(y)dy\right) f_{|h_R|^2}(z)dz. \tag{D.2}$$

Now, by substituting the PDF $f_{\gamma_{ps}}(x)$ and then solving the associated integral, (D.2) can be simplified as

$$\begin{aligned} F_{\gamma_{psr}^{\text{AF}}}(\gamma_s) =& \int_0^\infty \left(\int_{\frac{\zeta\gamma_s z}{T_1}}^\infty \left(1 - \sum_{k=0}^{m_{ps}-1} \frac{(T_0\gamma_s)^k}{k!} e^{-\left(\frac{T_0\gamma_s(1+\zeta\beta y)}{T_1 y - \zeta\gamma_s z}\right)}\right.\right. \\ &\times \left.\left.\left(\frac{1+\zeta\beta y}{T_1 y - \zeta\gamma_s z}\right)^k\right) f_{|h_{sr}|^2}(y)dy\right) f_{|h_R|^2}(z)dz. \end{aligned} \tag{D.3}$$

Hereby, (D.3) can be represented as $F_{\gamma_{psr}^{\text{AF}}}(\gamma_s) = \Psi_1(\gamma_s) - \Psi_2(\gamma_s)$, with $\Psi_1(\gamma_s)$ given by

$$\Psi_1(\gamma_s) = \int_0^\infty \left(\int_{\frac{\zeta\gamma_s z}{T_1}}^\infty f_{|h_{sr}|^2}(y)dy\right) f_{|h_R|^2}(z)dz. \tag{D.4}$$

After inserting the associated PDF expressions of y and z into (D.4) and simplifying further, one can arrive at (3.50). Next, we focus on the evaluation of $\Psi_2(\gamma_s)$, which can be written while following (D.3) as

$$\Psi_2(\gamma_s)=\int_0^{\infty}\Bigg(\int_{\frac{\zeta\gamma_s z}{T_1}}^{\infty}\Bigg(\sum_{k=0}^{m_{ps}-1}\frac{(T_0\gamma_s)^k}{k!}e^{-\left(\frac{T_0\gamma_s(1+\zeta\beta y)}{T_1 y-\zeta\gamma_s z}\right)} \times\left(\frac{1+\zeta\beta y}{T_1 y-\zeta\gamma_s z}\right)^k\Bigg)f_{|h_{sr}|^2}(y)dy\Bigg)f_{|h_R|^2}(z)dz. \tag{D.5}$$

Now, invoking the PDF expression $f_{|h_{sr}|^2}(y)$ along with a substitution $T_1 y-\zeta\gamma_s z=t$, $\Psi_2(\gamma_s)$ can be re-expressed as

$$\Psi_2(\gamma_s)=\int_0^{\infty}\Bigg(\mathbb{M}\int_0^{\infty}t^{m-k}e^{-\frac{T_0\gamma_s(\zeta^2\beta\gamma_s z+T_1)}{T_1 t}-\frac{m_{sr}}{\Omega_{sr}T_1}t}dt\Bigg) z^{j+m_{sr}-1-m}e^{-T_2\zeta z}f_{|h_R|^2}(z)dz, \tag{D.6}$$

where

$$\mathbb{M}=\sum_{k=0}^{m_{ps}-1}\sum_{j=0}^{k}\sum_{m=0}^{j+m_{sr}-1}\frac{(T_0\gamma_s)^k}{k!}\frac{1}{\Gamma(m_{sr})}\left(\frac{m_{sr}}{\Omega_{sr}}\right)^{m_{sr}}\binom{k}{j}(\zeta\beta)^j \times\left(\frac{1}{T_1}\right)^{j+m_{sr}}\binom{j+m_{sr}-1}{m}(\zeta\gamma_s)^{j+m_{sr}-1-m}e^{\frac{-T_0\gamma_s\zeta\beta}{T_1}}. \tag{D.7}$$

On computing the inner integral in (D.6) using [95, eq. 3.471.9], and then simplifying while substituting the PDF expression $f_{|h_R|^2}(z)$, $\Psi_2(\gamma_s)$ can be obtained as

$$\Psi_2(\gamma_s)=\mathbb{M}\times\frac{1}{\Gamma(m_R)}\left(\frac{m_R}{\Omega_R}\right)^{m_R}\int_0^{\infty}z^{j+m_R+m_{sr}-2-m} \times e^{(-T_2\zeta z-\frac{m_R}{\Omega_R}z)}2\left(\frac{T_0\gamma_s\Omega_{sr}(T_1+\zeta^2\beta\gamma_s z)}{m_{sr}}\right)^{\frac{m-k+1}{2}} \times\mathcal{K}_{m-k+1}\left(2\sqrt{\frac{T_0\gamma_s m_{sr}(T_1+\zeta^2\beta\gamma_s z)}{\Omega_{sr}T_1^2}}\right)dz. \tag{D.8}$$

Finally, substituting $(T_1+\zeta^2\beta\gamma_s z)=\theta$ into (D.8), and simplifying further, one can get the required result as provided in (3.51).

APPENDIX E

DERIVATIONS OF (3.53)

Using (3.18), the CDF $F_{\gamma_{sr}^{\text{noc}}}(\gamma_s) = \Pr\left[\gamma_{sr}^{\text{noc}} < \gamma_s\right]$ can be expressed as

$$F_{\gamma_{sr}^{\text{noc}}}(\gamma_s) = \Pr\left[\beta\gamma_{ps}|h_{sr}|^2 < \gamma_s\right]$$
$$= \Pr\left[|h_{sr}|^2 < \frac{\gamma_s}{\beta\gamma_{ps}}\right], \tag{E.1}$$

which can be further evaluated as

$$F_{\gamma_{sr}^{\text{noc}}}(\gamma_s) = \int_0^\infty F_{|h_{sr}|^2}\left(\frac{\gamma_s}{\beta\gamma_{ps}}\right) f_{\gamma_{ps}}(y)dy. \tag{E.2}$$

On substituting the corresponding PDF, CDF in (E.2) and simplifying further with the aid of [95, eq. 3.351.3], one can get the required result as provided in (3.53).

APPENDIX F

DERIVATIONS OF (3.59)

From (3.57), the probability term P_{12} can be expressed as

$$P_{12} = \Pr\left[|h_{sr}|^2 < \frac{\gamma_s}{\beta\gamma_{ps}^{\mathrm{DL}}},\ |h_{sr}|^2 \geq \frac{\gamma_s}{\beta\gamma_p}\right], \tag{F.1}$$

which can be further evaluated as

$$\begin{aligned} P_{12} &= \int_0^\infty \left(\int_{\frac{\gamma_s}{\beta\gamma_p}}^{\frac{\gamma_s}{\beta\eta_p z}} f_{|h_{sr}|^2}(y)dy\right) f_{\gamma_{ps}^{\mathrm{DL}}}(z)dz \\ &= \int_0^\infty F_{|h_{sr}|^2}\left(\frac{\gamma_s}{\beta\eta_p z}\right) f_{\gamma_{ps}^{\mathrm{DL}}}(z)dz - \int_0^\infty F_{|h_{sr}|^2}\left(\frac{\gamma_s}{\beta\gamma_p}\right) f_{\gamma_{ps}^{\mathrm{DL}}}(z)dz. \end{aligned} \tag{F.2}$$

On substituting the corresponding PDF and CDF in (F.2) and simplifying further with the aid of [95, eq. 3.351.3], one can obtain the desired result as given in (3.59).

APPENDIX G

DERIVATIONS OF (4.18)

By substituting (4.6) and (4.7) in (4.15), $P^{t1}_{\text{out},UE1}$ can be expressed as

$$P^{t1}_{\text{out},UE1} = 1 - \Pr\left[\frac{\psi_2\eta_p|h_{p,1}|^2}{\psi_1\eta_p|h_{p,1}|^2+1} > \gamma_{R_2}, \frac{\psi_1\eta_p|h_{p,1}|^2}{\lambda\psi_2\eta_p|h_1|^2+1} > \gamma_{R_1}\right]. \tag{G.1}$$

After some algebraic manipulations, (G.1) can be written as

$$\begin{aligned}
P^{t1}_{\text{out},UE1} &= 1 - \Pr\left[|h_{p,1}|^2 > \mathcal{U}_2, |h_{p,1}|^2 > \bar{\mathcal{U}}_1|h_1|^2 + \mathcal{U}_1\right] \\
&= 1 - \Pr[|h_{p,1}|^2 > \max\left\{\mathcal{U}_2, \bar{\mathcal{U}}_1|h_1|^2 + \mathcal{U}_1\right\}] \\
&= 1 - \underbrace{\Pr[|h_{p,1}|^2 > \mathcal{U}_2, \mathcal{U}_2 > \bar{\mathcal{U}}_1|h_1|^2 + \mathcal{U}_1]}_{\mathcal{Z}_0} \\
&- \underbrace{\Pr[|h_{p,1}|^2 > \bar{\mathcal{U}}_1|h_1|^2 + \mathcal{U}_1, \mathcal{U}_2 \leq \bar{\mathcal{U}}_1|h_1|^2 + \mathcal{U}_1]}_{\mathcal{Z}_1}.
\end{aligned} \tag{G.2}$$

Letting $|h_{p,1}|^2 \triangleq X, |h_1|^2 \triangleq Y$, $\mathcal{Z}_0$ and $\mathcal{Z}_1$ can be further evaluated as

$$\mathcal{Z}_0 = (1 - F_X(\mathcal{U}_2))F_Y(\mathcal{U}_0), \tag{G.3}$$

$$\mathcal{Z}_1 = \int_{\mathcal{U}_0}^{\infty}\left(\int_{\bar{\mathcal{U}}_1 y + \mathcal{U}_1}^{\infty} f_X(x)dx\right) f_Y(y)dy. \tag{G.4}$$

We can readily evaluate $\mathcal{Z}_0$ in (G.3) using (4.2) and [95, eq. 8.352.1] to present the result in (4.17).

Now, by substituting the PDF $f_X(x)$ using (4.1) and then computing the linked integral in (G.4), $\mathcal{Z}_1$ can be given as

$$\mathcal{Z}_1 = \int_{\mathcal{U}_0}^{\infty} \sum_{k=0}^{m_{p1}-1} \frac{(\bar{U}_1 y + \mathcal{U}_1)^k}{k!} \left(\frac{m_{p1}}{\Omega_{p1}}\right)^k \mathrm{e}^{-\left(\frac{m_{p1}(\bar{\mathcal{U}}_1 y + \mathcal{U}_1)}{\Omega_{p1}}\right)} f_Y(y) dy. \tag{G.5}$$

By applying the binomial expansion [95, eq. 1.111] and solving the involved integral, one can get the result in (4.18).

APPENDIX H

DERIVATIONS OF (4.24)

Using (4.6) and (4.14) in (4.21), $P^{\mathrm{t}_2}_{\mathrm{out,UE1}}$ can be expressed as

$$P^{t_2}_{\mathrm{out},UE1} = 1 - \Pr\left[\frac{\psi_2\eta_p|h_{p,1}|^2}{\psi_1\eta_p|h_{p,1}|^2+1} > \gamma_{R_2}, \frac{\psi_3\eta_p|h_{p,1}|^2}{\psi_r\beta\eta_p|h_{p,s}|^2|h_{s,1}|^2+1} > \gamma_{R_1}\right]. \tag{H.1}$$

With some algebraic manipulations, one can re-write (H.1) as

$$\begin{aligned} P^{t2}_{\mathrm{out},UE1} &= 1 - \Pr\left[|h_{p,1}|^2 > \mathcal{U}_2, |h_{p,1}|^2 > \hat{\mathcal{U}}_{11}|h_{p,s}|^2|h_{s,1}|^2 + \hat{\mathcal{U}}_1)\right] \\ &= 1 - \Pr\left[|h_{p,1}|^2 > \max\left\{\mathcal{U}_2, \hat{\mathcal{U}}_{11}|h_{p,s}|^2|h_{s,1}|^2 + \hat{\mathcal{U}}_1)\right\}\right]. \end{aligned} \tag{H.2}$$

Denoting $|h_{p,1}|^2 \triangleq X$, $|h_{p,s}|^2 \triangleq W$, and $|h_{s,1}|^2 \triangleq Z$, we can evaluate (H.2) as

$$\begin{aligned} P^{t2}_{\mathrm{out},UE1} = 1 - &\underbrace{\Pr\left[X > \mathcal{U}_2, \mathcal{U}_2 > (\hat{\mathcal{U}}_{11}WZ + \hat{\mathcal{U}}_1)\right]}_{\mathcal{Z}_2} \\ &- \underbrace{\Pr\left[X > (\hat{\mathcal{U}}_{11}WZ + \hat{\mathcal{U}}_1), \mathcal{U}_2 \leq (\hat{\mathcal{U}}_{11}WZ + \hat{\mathcal{U}}_1)\right]}_{\mathcal{Z}_3}. \end{aligned} \tag{H.3}$$

Now, we can evaluate $\mathcal{Z}_2$ and $\mathcal{Z}_3$ in (H.3) as follows.

$$\mathcal{Z}_2 = \int_{\mathcal{U}_2}^{\infty} f_X(x)dx \int_0^{\infty} f_Z(z)F_W\left(\frac{\bar{\mathcal{U}}_0}{z}\right)dz. \tag{H.4}$$

By substituting respective PDFs and CDF in (H.4) and solving the integral with the aid of [95, eqs. 3.351.2, 3.471.9], one can reach at (4.23). While, $\mathcal{Z}_3$ in (H.3) can be re-written as

$$
\begin{aligned}
\mathcal{Z}_3 &= \Pr\left[W < \frac{X - \hat{\mathcal{U}}_1}{\mathcal{U}_{11} Z}, \quad W \geq \left(\frac{\bar{\mathcal{U}}_0}{Z}\right)\right] \\
&= \int_0^\infty \int_{\hat{\mathcal{U}}_1}^\infty F_W\left(\frac{x - \hat{\mathcal{U}}_1}{\hat{\mathcal{U}}_{11} z}\right) f_X(x) f_Z(z) dx dz \\
&\quad + \int_0^{\hat{\mathcal{U}}_1} f_X(x) dx - \int_0^\infty F_W\left(\frac{\bar{\mathcal{U}}_0}{z}\right) f_Z(z) dz.
\end{aligned} \tag{H.5}
$$

By inserting the corresponding PDFs and CDFs in (H.5), and solving the involved integrals with the help of [95, eqs. 3.351.1, 3.351.2, 3.471.9], one can arrive at the result in (4.24).

APPENDIX I

DERIVATIONS OF (4.36)

By invoking (4.34) in (4.32) and with some algebraic manipulations, $P_{\mathrm{out},sr}^{\mathrm{ipSIC}}$ can be expressed as

$$
\begin{aligned}
P_{\mathrm{out},sr}^{\mathrm{ipSIC}} &= \Pr[W \leq \mathcal{U}_2] \\
&\quad + \Pr\left[W > \mathcal{U}_2, Z_1 \leq \min\left\{\frac{\mathcal{U}_4}{W}, \frac{\mathcal{U}_5(\psi_2\beta\eta_p W Z_2 + 1)}{W}\right\}\right] \\
&= F_W\left(\mathcal{U}_2\right) + \underbrace{\Pr\left[W > \mathcal{U}_2, Z_1 \leq \frac{\mathcal{U}_4}{W}, Z_2 > \frac{\bar{\mathcal{U}_5}}{W}\right]}_{\mathcal{P}_I} \\
&\quad + \underbrace{\Pr\left[W > \mathcal{U}_2, Z_1 \leq \mathcal{U}_5\psi_2\beta\eta_p Z_2 + \frac{\mathcal{U}_5}{W}, Z_2 < \frac{\bar{\mathcal{U}_5}}{W}\right]}_{\mathcal{P}_{II}}. \qquad \text{(I.1)}
\end{aligned}
$$

Here, $F_W\left(\mathcal{U}_2\right)$ can be directly evaluated with the aid of (4.2). Further, $\mathcal{P}_I$ and $\mathcal{P}_{II}$ can be evaluated as follows.

$$
\mathcal{P}_I = \int_{\mathcal{U}_2}^{\infty} F_{Z_1}\left(\frac{\mathcal{U}_4}{w}\right)\left(1 - F_{Z_2}\left(\frac{\bar{\mathcal{U}_5}}{w}\right)\right) f_W(w)dw. \qquad \text{(I.2)}
$$

By invoking the respective CDFs and PDF in (I.2), and integrating the resultant with the aid of [95, eq. 3.351.2], one can get the required result.

$$
\begin{aligned}
\mathcal{P}_{II} &= \int_{\mathcal{U}_2}^{\infty}\left(\int_0^{\frac{\bar{\mathcal{U}_5}}{w}}\left(\int_0^{\mathcal{U}_5\psi_2\beta\eta_p z_2 + \frac{\mathcal{U}_5}{w}} f_{Z_1}(z_1)dz_1\right) f_{Z_2}(z_2)dz_2\right) f_W(w)dw, \\
&= \int_{\mathcal{U}_2}^{\infty}\left(\int_0^{\frac{\bar{\mathcal{U}_5}}{w}}\left[1 - \sum_{k=0}^{m_{sr}-1}\frac{1}{k!}\left(\frac{m_{sr}}{\Omega_{sr}}\right)^k\left(\mathcal{U}_5\psi_2\beta\eta_p z_2 + \frac{\mathcal{U}_5}{w}\right)^k e^{-\frac{m_{sr}}{\Omega_{sr}}\left(\mathcal{U}_5\psi_2\beta\eta_p z_2 + \frac{\mathcal{U}_5}{w}\right)}\right]\right. \\
&\quad \left.\times f_{Z_2}(z_2)dz_2\right) f_W(w)dw. \qquad \text{(I.3)}
\end{aligned}
$$

After inserting the associated PDFs and solving the resultant integral with the aid of binomial expansion [95, eq. 1.111] and [95, eq. 3.351.2], one can get the required result. On invoking the deduced results from (I.2) and (I.3) in (I.1), we obtain (4.36).

APPENDIX J

DERIVATION OF (5.20)

We can evaluate $P_{D_1}^{\text{out},t_2}$ in (5.19) as

$$P_{D_1}^{\text{out},t_2} = \int_0^\infty \left(\int_0^\infty F_W(\mathcal{B}_1 xv + \mathcal{B}_2) f_X(x) dx \right) f_V(v) dv. \tag{J.1}$$

By substituting the CDF of W in infinite series form utilizing [95, eq. 8.445] and [101, eq. 4.35], (J.1) can be expressed as

$$\begin{aligned} P_{D_1}^{\text{out},t_2} = \int_0^\infty \left(\int_0^\infty \left(1 - \sum_{l=0}^{\infty} \sum_{m=0}^{l} \frac{K^l \phi^m e^{-K} (\mathcal{B}_1 xv + \mathcal{B}_2)^m}{l!m!} \right.\right. \\ \left.\left. \times\, e^{-(\mathcal{B}_1 xv + \mathcal{B}_2)} \right) f_X(x) dx \right) f_V(v) dv. \end{aligned} \tag{J.2}$$

By substituting the respective PDFs and utilizing the binomial expansion [95, eq. 1.111] and [95, eq. 3.351.1] to solve (J.1) rigourously, one can obtain the result as given in (5.20).

APPENDIX K

DERIVATION OF (5.25)

By substituting (5.7) and (5.24) in (5.22) and with some mathematical re-arrangement, $P_{D_2}^{\text{out},t_2}$ can be evaluated as

$$\begin{aligned} P_{D_2}^{\text{out},t_2} &= \Pr\left[X < \frac{\mathcal{A}_5}{\rho_s}\right] + \Pr\left[X \geq \frac{\mathcal{A}_5}{\rho_s}, Y \leq \frac{\Delta_2}{X\rho_s}\right] \\ &= 1 - \frac{1}{\lambda_{SI}} \int_{\frac{\mathcal{A}_5}{\rho_s}}^{\infty} e^{-\frac{\Delta_2}{\lambda_{ID_2}\rho_s x}} e^{-\frac{x}{\lambda_{SI}}} dx. \end{aligned} \tag{K.1}$$

Since the integral in (K.1) is intractable, we utilize the Maclaurin series expansion for the term $e^{-\frac{\Delta_2}{\lambda_{ID_2}\rho_s x}}$ to simplify (K.1) as

$$P_{D_2}^{\text{out},t_2} = 1 - \sum_{l=0}^{\infty} \frac{(-1)^l}{l!} \left(\frac{\Delta_2}{\lambda_{ID_2}\rho_s}\right)^l \frac{1}{\lambda_{SI}} \int_{\frac{\mathcal{A}_5}{\rho_s}}^{\infty} \frac{e^{-\frac{x}{\lambda_{SI}}}}{x^l} dx. \tag{K.2}$$

By solving the integral term in (K.2), (5.25) can be obtained.

REFERENCES

[1] L. Atzori, A. Iera, and G. Morabito, "The internet of things: A survey," *Computer Networks*, vol. 54, no. 15 (2010), pp. 2787–2805.

[2] D. Reinsel, J. Gantz, and J. Rydning, "Data age 2025: the digitization of the world from edge to core," *IDC White Paper* Doc# US44413318 (2018), pp. 1–29.

[3] X. Li, *et al.*, "Smart community: an Internet of Things application," *IEEE Commun. Mag.*, vol. 49, no. 11, pp. 68-75, Nov. 2011.

[4] C. Bockelmann *et al.* "Towards massive connectivity support for scalable mMTC communications in 5G networks," *IEEE Access*, vol. 6, pp. 28969-28992, 2018.

[5] S. Singh, N. Saxena, A. Roy, and H. Kim "Energy efficiency in wireless networks– a composite review," *IETE Techn. Review* vol. 32, no. 2, pp. 84–93, 2015.

[6] Z. Ding, X. Lei, G. K. Karagiannidis, R. Schober, J. Yuan, and V. K. Bhargava, "A survey on non-orthogonal multiple access for 5G networks: Research challenges and future trends," *IEEE J. Sel. Areas Commun.*, vol. 35, no. 10, pp. 2181-2195, Oct. 2017.

[7] X. Lu, P. Wang, D. Niyato, D. I. Kim, and Z. Han, "Wireless networks with RF energy harvesting: A contemporary survey," *IEEE Commun. Surveys Tuts.*, vol. 17, no. 2, pp. 757-789, 2nd Quart., 2015.

[8] I. Krikidis, S. Timotheou, S. Nikolaou, G. Zheng, D. W. K. Ng, and R. Schober, "Simultaneous wireless information and power transfer in modern communication systems," *IEEE Commun. Mag.*, vol. 52, no. 11, pp. 104-110, Nov. 2014.

[9] S. Haykin, "Cognitive radio: Brain-empowered wireless communications," *IEEE J. Sel. Areas Commun.*, vol. 23, no. 2, pp. 201-220, Feb. 2005.

[10] H. A. Suraweera, P. J. Smith, and M. Shafi, "Capacity limits and performance analysis of cognitive radio with imperfect channel knowledge," *IEEE Trans. Veh. Technol.*, vol. 59, no. 4, pp. 1811-1822, May 2010.

[11] Y. Han, A. Pandharipande, and S. H. Ting, "Cooperative decode-and-forward relaying for secondary spectrum access," *IEEE Trans. Wireless Commun.*, vol. 8, no. 10, pp. 4945-4950, Oct. 2009.

[12] Z. Wei, L. Yang, D. W. K. Ng, J. Yuan, and L. Hanzo, "On the performance gain of NOMA over OMA in uplink communication systems," *IEEE Trans. Commun.*, vol. 68, no. 1, pp. 536-568, Jan. 2020.

[13] D. Tse and P. Viswanath, *Fundamentals of Wireless Communication*, UK: Cambridge Univ. Press, 2005.

[14] C. K. Singh, V. Singh, P. K. Upadhyay, and M. Lin, "Energy harvesting in overlay cognitive NOMA systems with hardware impairments," *IEEE Syst. J.*, vol. 16, no. 2, pp. 2648-2659, Jun. 2022.

[15] D. Bapatla and S. Prakriya, "Performance of a cooperative communication network with green self-sustaining nodes," *IEEE Trans. Green Commun. and Net.*, vol. 5, no. 1, pp. 426-441, Sep. 2020.

[16] A. Nasir, X. Zhou, S. Durrani, and R. Kennedy, "Relaying protocols for wireless energy harvesting and information processing, " *IEEE Trans. Wireless Commun.*, vol. 12, no. 7, pp. 3622-3636, Jul. 2013.

[17] P. Phunchongharn, E. Hossain, D. Niyato, and S. Camorlinga, "A cognitive radio system for e-health applications in a hospital environment," *IEEE Wireless Commun.*, vol. 17, no.1, pp. 20-28, Feb. 2010.

[18] Y. Xu *et al.*, "Joint beamforming and power-splitting control in downlink cooperative SWIPT NOMA systems," *IEEE Trans. Signal Process.*, vol. 65, no. 18, pp. 4874-4886, Sep. 2017.

[19] D. Wang and S. Men, "Secure energy efficiency for NOMA based cognitive radio networks with nonlinear energy harvesting," *IEEE Access*, vol. 6, pp. 62707-62716, Oct. 2018.

[20] F. Li, H. Jiang, R. Fan, and P. Tan, "Cognitive non-orthogonal multiple access with energy harvesting: An optimal resource allocation approach," *IEEE Trans. Veh. Technol.*, vol. 68, no. 7, pp. 7080-7095, Jul. 2019.

[21] X. Wang *et al.*, "Energy efficiency optimization for NOMA-based cognitive radio with energy harvesting," *IEEE Access*, vol. 7, pp. 139172-139180, Sep. 2019.

[22] Y. Yu *et al.*, "Outage performance of NOMA in cooperative cognitive radio networks with SWIPT," *IEEE Access*, vol. 7, pp. 117308-117317, Aug. 2019.

[23] L. Lv, Q. Ni, Z. Ding, and J. Chen, "Application of non-orthogonal multiple access in cooperative spectrum-sharing networks over Nakagami-m fading channels," *IEEE Trans. Veh. Technol.*, vol. 66, no. 6 , pp. 5510-5515, Jun. 2017.

[24] X. Yue *et al.*, "Secure communications in a unified non-orthogonal multiple access framework," *IEEE Trans. Commun.*, vol. 19, no. 3, pp. 2163-2178, Mar. 2020.

[25] N. S. Mouni, A. Kumar, and P. K. Upadhyay, "Adaptive user pairing for downlink NOMA system with imperfect SIC," *IEEE Wireless Commun. Lett.*, Apr. 2021, doi:10.1109/LWC.2021.3074036.

[26] L. Luo, Q. Li, and J Cheng, "Performance analysis of overlay cognitive NOMA systems with imperfect successive interference cancellation," *IEEE Tran. Commun.*, vol. 68, no. 8, pp. 4709-4722, Aug. 2020.

[27] S. Singh and M. Bansal, "Performance analysis of NOMA-based AF cooperative overlay system with imperfect CSI and SIC," *IEEE Access*, vol. 9, pp. 40263-40273, Mar. 2021.

[28] G. Im and J. H. Lee, "Outage probability for cooperative NOMA systems with imperfect SIC in cognitive radio networks," *IEEE Commun. Lett.*, vol. 23, no. 4, pp. 692–695, Apr. 2019.

[29] J. Kim and I. Lee, "Non-Orthogonal multiple access in coordinated direct and relay transmission," *IEEE Commun. Lett.*, vol. 19, no. 11, pp. 2037-2040, Nov. 2015.

[30] D. B. Smith, D. Miniutti, T. A. Lamahewa, and L. W. Hanlen, "Propagation models for body-area networks: A survey and new outlook," *IEEE Antennas Propag. Mag.*, vol. 55, no. 5, pp. 97-117, Oct. 2013.

[31] U. Varshney, "Pervasive healthcare: Applications, challenges and wireless solutions," *Commun. of the Assoc. for Inf. Systems,* vol. 16, no. 3, pp. 57-72, Jul. 2005.

[32] A. Soomro and D. Cavalcanti, "A truthful mechanism for scheduling delay-constrained wireless transmissions in IoT-based healthcare networks," *IEEE Trans. Wireless Commun.,* vol. 18, no. 2, pp. 912-925, Feb. 2019.

[33] M. T. I. ul Huque, K. S. Munasinghe, and A. Jamalipour, "Body node coordinator placement algorithms for wireless body area networks," *IEEE Internet Things J.,* vol. 2, no. 1, pp. 94-102, Feb. 2015.

[34] K. S. Kwak, S. Ullah, and N. Ullah, "An overview of IEEE 802.15.6 standard," *in Proc. Int. Symp. Applied Sc. in Biomedical Commun. Tech. (ISABEL),* Rome, Italy, Nov. 2010.

[35] Z. Liu, B. Liu, and C. W. Chen, "Transmission-rate-adaption assisted energy-efficient resource allocation with QoS support in WBANs," *IEEE Sensors J.*, vol. 17, no. 17, pp. 5767–5780, Jul. 2017.

[36] B. Braem, B. Latre, I. Moerman, C. Blondia, and P. Demeester, "The need for cooperation and relaying in short-range high path loss sensor networks," *in Proc. Int. Conf. Sensor Technol. Appl. (SENSORCOMM)*, Valencia, Spain, Oct. 2007, pp. 566-571.

[37] Y. Chen, J. Teo, J. C. Y. Lai, E. Gunawan, K. S. Low, C. B. Soh, and P. B. Rapajic, "Cooperative communications in ultra-wideband wireless body area networks: Channel modeling and system diversity analysis," *IEEE J. Sel. Areas Commun.*, vol. 27, no. 1, pp. 5-16, Jan. 2009.

[38] L. C. Tran, A. Mertins, X. Huang and F. Safaei, "Comprehensive performance analysis of fully cooperative communication in WBANs," *IEEE Access*, vol. 4, pp. 8737-8756, 2016.

[39] S. M. Demir, F. Al-Turjman, and A. Muhtaroğlu, "Energy scavenging methods for WBAN applications: A review," *IEEE Sensors J.*, vol. 18, no. 16, pp. 6477-6488, Aug. 2018.

[40] G. Smart, N. Deligiannis, R. Surace, V. Loscri, G. Fortino, and Y. Andreopoulos, "Decentralized time-synchronized channel swapping for ad hoc wireless networks," *IEEE Trans. Veh. Technol.*, vol. 65, no. 10, pp. 8538-8553, Oct. 2016.

[41] S. A. Sakin, M. A. Razzaque, M. M. Hassan, A. Alamri, N. H. Tran, and G. Fortino, "Self-coexistence among IEEE 802.22 networks: Distributed allocation of power and channel," *Sensors*, vol. 17, no.12: 2838, 2017.

[42] S. Feng, Z. Liang, and D. Zhao, "Providing telemedicine services in an infrastructure-based cognitive radio network," *IEEE Wireless Commun.*, vol. 17, no.1, pp. 96-103, Feb. 2010.

[43] F. Jingling, L. Wei, and L. Yang, "Performance enhancement of wireless body area network system combined with cognitive radio," *in Proc. Int. Conf. Commun. Mobile Comput. (CMC)*, Shenzhen, China, Apr. 2010.

[44] V. Marbukh and K. Sayrfian, "Regret minimization based adaptation of the energy detection threshold in body area networks," *Global Internet Things Summit (GIoTS)*, Geneva, Switzerland, Jun. 2017.

[45] A. R. Syed and K.-L. A. Yau, "On cognitive radio-based wireless body area networks for medical applications," *in Proc. IEEE Symp. on Comp. Intel. in Healthcare and e-health (CICARE)*, Singapore, Aug. 2013.

[46] T. Ahmed and Y. L. Moullec, "A QoS optimization approach in cognitive body area networks for healthcare applications," *Sensors (Basel)*, vol. 17, no. 4, Apr. 2017.

[47] S. Sodagari, B. Bozorgchami, and H. Aghvami, "Technologies and challenges for cognitive radio enabled medical wireless body area networks," *IEEE Access*, vol. 6, pp. 29567-29586, Jun. 2018.

[48] S. Kim, S. Kim, and D.-S. Eom, "RSSI/LQI-based transmission power control for body area networks in healthcare environment," *IEEE J. Biomed. Health Inform.*, vol. 17, no. 3, pp. 561-571, May 2013.

[49] R. Di Bari, Q. H. Abbasi, A. Alomainy, and Y. Hao, "An advanced UWB channel model for body-centric wireless networks," *Progress in Electromagnetics Research*, vol. 136, 79-99, 2013.

[50] D. Sui, F. Hu, W. Zhou, M. Shao, and M. Chen, "Relay selection for radio frequency energy-harvesting wireless body area network with buffer," *IEEE Internet Things J.*, vol. 5, no. 2, pp. 1100-1107, Apr. 2018.

[51] S. Xiao, A. Dhamdhere, V. Sivaraman, and A. Burdett, "Transmission power control in body area sensor networks for healthcare monitoring," *IEEE J. Sel. Areas Commun.*, vol. 27, no. 1, pp. 37-48, Jan. 2009.

[52] Y. Han, A. Pandharipande, and S. H. Ting, "Cooperative decode-and-forward relaying for secondary spectrum access," *IEEE Trans. Wireless Commun.*, vol. 8, no. 10, pp. 4945-4950, Oct. 2009.

[53] S. Solanki, V. Singh, and P. K. Upadhyay, "RF energy harvesting in hybrid two-way relaying systems with hardware impairments," *IEEE Trans. Veh. Technol.*, vol. 68, no. 12, pp. 11792-11805, Dec. 2019.

[54] H. M.-Jahromi, B. Maham, and T. A. Tsiftsis, "Maximizing spectral efficiency for energy harvesting-aware WBAN," *IEEE J. Bio. and Health Inform.*, vol. 21, no. 3, pp. 732-742, May 2017.

[55] S. van Roy, F. Quitin, L. Liu, C. Oestges, F. Horlin, J.-M. Dricot, and P. De Doncker, "Dynamic channel modeling for multi-sensor body area networks," *IEEE Trans. Antennas Propag.*, vol. 61, no. 4, pp. 2200–2208, Apr. 2013.

[56] L. Dai, B. Wang, Y. Yuan, S. Han, I. Chih-lin, and Z. Wang, "Non-orthogonal multiple access for 5G: Solutions, challenges, opportunities, and future research trends," *IEEE Commun. Mag.*, vol. 53, no. 9, pp. 74-81, Sep. 2015.

[57] S. M. R. Islam, N. Avazov, O. A. Dobre, and K-S. Kwak, "Power-domain non-orthogonal multiple access (NOMA) in 5G systems: Potentials and challenges," *IEEE Commun. Surveys Tuts.*, vol. 19, no. 2, pp. 721-742, Second Quart., 2017.

[58] Z. Ding *et al.*, "A survey on non-orthogonal multiple access for 5G networks: Research challenges and future trends," *IEEE J. Sel. Areas Commun.*, vol. 35, no. 10, pp. 2181-2195, Oct. 2017.

[59] L. Lv, J. Chen, Q. Ni, Z. Ding, and H. Jiang, "Cognitive non-orthogonal multiple access with cooperative relaying: A new wireless frontier for 5G spectrum sharing," *IEEE Commun. Mag.*, vol. 56, no. 4, pp. 188-195, Apr. 2018.

[60] Y. Liu, Z. Ding, M. Elkashlan, and J. Yuan, "Non-orthogonal multiple access in large-scale underlay cognitive radio networks," *IEEE Trans. Veh. Technol.*, vol. 65, no. 12, pp. 10152-10157, Dec. 2016.

[61] S. Arzykulov, G. Nauryzbayev, T. A. Tsiftsis, and B. Maham, "Performance analysis of underlay cognitive radio nonorthogonal multiple access networks," *IEEE Trans. Veh. Technol.*, vol. 68, no. 9, pp. 9318-9322, Sep. 2019.

[62] S. Arzykulov, G. Nauryzbayev, T. A. Tsiftsis, B. Maham, and M. Abdallah, "On the outage of underlay CR-NOMA networks with detect-and-forward relaying," *IEEE Trans. Cogn. Commun. Netw.*, vol. 5, no. 3, pp. 795-804, Sep. 2019.

[63] K. Sultan, "Best relay selection schemes for NOMA based cognitive relay networks in underlay spectrum sharing," *IEEE Access*, vol. 8, pp. 190160-190172, Oct. 2020.

[64] T. -T. Nguyen, T. -H. Vu, T. -V. Nguyen, D. B. da Costa, and C. D. Ho, "Underlay cognitive NOMA-based coordinated direct and relay transmission," *IEEE Wireless Commun. Lett.*, vol. 10, no. 4, pp. 854-858, Apr. 2021.

[65] S. Solanki, P. K. Upadhyay, D. B. da Costa, H. Ding, and J. M. Moualeau, "Performance analysis of piece-wise linear model of energy harvesting-based multiuser overlay spectrum sharing networks," *IEEE Open J. Commun. Society*, vol. 1, pp. 1820-1836, Nov. 2020.

[66] K. Nguyen, Q. Vu, L. Tran, and M. Juntti, "Energy efficiency fairness for multi-pair wireless-powered relaying systems," *IEEE J. Sel. Areas Commun.*, vol. 37, no. 2, pp. 357–373, Feb. 2019.

[67] P. Kumar and K. Dhaka, "Performance of wireless powered DF relay system under Nakagami-m fading: Relay assists energy-constrained source," *IEEE Syst. J.*, vol. 14, no. 2, pp. 2497-2507, Jun. 2020.

[68] E. Boshkovska, D. W. K. Ng, N. Zlatanov, and R. Schober, "Practical non-linear energy harvesting model and resource allocation for SWIPT systems," *IEEE Commun. Lett.*, vol. 19, no. 12, pp. 2082-2085, Dec. 2015.

[69] A. Kumar and K. Kumar, "Relay sharing with DF and AF techniques in NOMA assisted cognitive radio networks," *Phys. Commun.*, vol. 42, Oct. 2020.

[70] D. S. Gurjar, U. Singh, and P. K. Upadhyay, "Energy harvesting in hybrid two-way relaying with direct link under Nakagami-m fading," in *Proc. IEEE Wireless Commun. Netw. Conf. (WCNC)*, Barcelona, Spain, Apr. 2018, pp. 1-6.

[71] V. Aswathi and A. V. Babu, "Full/half duplex cooperative NOMA under imperfect successive interference cancellation and channel state estimation errors," *IEEE Access*, vol. 7, pp. 179961-179984, Dec. 2019.

[72] N. B. Mehta, V. Sharma, and G. Bansal, "Performance analysis of a cooperative system with rateless codes and buffered relays," *IEEE Trans. Wireless Commun.*, vol. 10, no. 4, pp. 1069-1081, Apr. 2011.

[73] I. Stanojev, O. Simeone, Y. B.-Ness, and C. You, "Performance of multirelay collaborative hybrid-ARQ protocols over fading channels," *IEEE Commun. Lett.*, vol. 10, no. 7, pp. 522-524, Jul. 2006.

[74] V. A. Aalo and J. Zhang, "Performance analysis of maximal ratio combining in the presence of multiple equal-power co-channel interferers in a Nakagami fading channel," *IEEE Trans. Veh. Technol.*, vol. 50, no. 2, pp. 497-503, Mar. 2001.

[75] T. M. Hoang, B. C. Nguyen, P. T. Tran, and L. T. Dung, "Outage analysis of RF energy harvesting cooperative communication systems over Nakagami-m fading channels with integer and non-integer m," *IEEE Trans. Veh. Technol.*, vol. 69, no. 3, pp. 2785-2801, Mar. 2020.

[76] C. Zhang, J. Ge, J. Li, Y. Rui, and M. Guizani, "A unified approach for calculating outage performance of two-way AF relaying over fading channels," *IEEE Trans. Veh. Technol.*, vol. 64, no. 3, pp. 1218-1229, Mar. 2015.

[77] Y. Liu, L. Wang, M. Elkashlan, T. Q. Duong, and A. Nallanathan, "Two-way relay networks with wireless power transfer: Design and performance analysis," *IET Commun.*, vol. 10, no. 14, pp. 1810-1819, Jun. 2016.

[78] L. Liu, R. Zhang, and K. C. Chua, "Wireless information and power transfer: A dynamic power splitting approach," *IEEE Trans. Commun.*, vol. 61, no. 9, pp. 3990-4001, Sep. 2013.

[79] D. Wang, F. Rezaei, and C. Tellambura, "Performance analysis and resource allocations for a WPCN with a new nonlinear energy harvester model," *IEEE Open J. Commun. Society*, vol. 1, pp. 1403-1424, Sep. 2020.

[80] A. Al-Fuqaha, M. Guizani, M. Mohammadi, M. Aledhari, and M. Ayyash, "Internet of Things: A survey on enabling technologies, protocols, and applications," *IEEE Commun. Surveys Tuts.*, vol. 17, no. 4, pp. 2347–2376, 4th Quart., 2015.

[81] A. K. Shukla, P. K. Upadhyay, A. Srivastava, and J. M. Moualeu, "Enabling Co-existence of cognitive sensor nodes with energy harvesting in body area networks," *IEEE Sensors J.*, vol. 21, no. 9, pp. 11213-11223, 1 May, 2021.

[82] Z. Kuang, G. Liu, G. Li, and X. Deng, "Energy efficient resource allocation algorithm in energy harvesting-based D2D heterogeneous networks," *IEEE Internet Things J.*, vol. 6, no. 1, pp. 557-567, Feb. 2019.

[83] S. Kumar, U. Dohare, K. Kumar, D. Prasad Dora, K. N. Qureshi, and R. Kharel, "Cybersecurity measures for geocasting in vehicular cyber physical system environments," *IEEE Internet Things J.*, vol. 6, no. 4, pp. 5916-5926, Aug. 2019.

[84] M. R. Palattella *et al.*, "Internet of things in the 5G era: Enablers, architecture, and business models," *IEEE J. Sel. Areas Commun.*, vol. 34, no. 3, pp. 510–527, Mar. 2016.

[85] A. Jee, K. Agrawal and S. Prakriya, "A coordinated direct AF/DF relay-aided NOMA framework for low outage," *IEEE Trans. Commun.*, vol. 70, no. 3, pp. 1559-1579, Mar. 2022.

[86] Y. Liu, Z. Ding, M. Elkashlan, and J. Yuan, "Non orthogonal multiple access in large-scale underlay cognitive radio networks," *IEEE Trans. Veh. Technol.*, vol. 65, no. 12, pp. 10152-10157, Dec. 2016.

[87] L. Zou, J. Chen, L. Lv, and B. He, "Capacity enhancement of D2D aided coordinated direct and relay transmission using NOMA," *IEEE Commun. Lett.*, vol. 24, no. 10, pp. 2128–2132, Oct. 2020.

[88] T.-T. Nguyen, T.-V. Nguyen, T.-H. Vu, D. B. da Costa, and C. D. Ho, "IoT-based coordinated direct and relay transmission with non-orthogonal multiple access," *IEEE Wireless Commun. Lett.*, vol. 10, no. 3, pp. 503–507, 2021.

[89] X. Li, Y. Chen, P. Xue, G. Lv, and M. Shu, "Outage performance for satellite-assisted cooperative NOMA systems with coordinated direct and relay transmission," *IEEE Commun. Lett.*, vol. 24, no. 10, pp. 2285– 2289, Oct. 2020.

[90] Z. Behdad, M. Mahdavi, and N. Razmi, "A new relay policy in RF energy harvesting for IoT networks—A cooperative network approach," *IEEE Internet Things J.*, vol. 5, no. 4, pp. 2715–2728, Aug. 2018.

[91] I. Krikidis, S. Timotheou, S. Nikolaou, G. Zheng, D. W. K. Ng, and R. Schober, "Simultaneous wireless information and power transfer in modern communication systems," *IEEE Commun. Magazine*, vol. 52, no. 11, pp. 104–110, 2014.

[92] X. Li, J. Li, and L. Li, "Performance analysis of impaired SWIPT NOMA relaying networks over imperfect Weibull channels," *IEEE Syst. J.*, vol. 14, no. 1, pp. 669-672, March 2020.

[93] Q. N. Le, N. -P. Nguyen, A. Yadav, and O. A. Dobre, "Outage performance of full-duplex overlay CR-NOMA networks with SWIPT," *2019 IEEE Global Communications Conference (GLOBECOM)*, 2019, pp. 1-6, Waikoloa, HI, USA.

[94] A. Rauniyar, P. E. Engelstad, and O. N. Østerbø, "Performance analysis of RF energy harvesting and information transmission based on NOMA with interfering signal for IoT relay systems," *IEEE Sensors J.*, vol. 19, no. 17, pp. 7668–7682, Sep. 2019.

[95] I. S. Gradshteyn and I. M. Ryzhik, *Tables of Integrals, Series and Products*, 6th ed. New York: Academic Press, 2000.

[96] N. T. Do, D. B. da Costa, T. Q. Duong, V. N. Q. Bao, and B. An, "Exploiting direct links in multiuser multirelay SWIPT cooperative networks with opportunistic scheduling," *IEEE Trans. Wireless Commun.*, vol. 16, no. 8, pp. 5410–5427, Aug. 2017.

[97] L. Pei *et al.*, "Energy-efficient D2D communications underlaying NOMA-based networks with energy harvesting," *IEEE Commun. Lett.*, vol. 22, no. 5, pp. 914–917, May 2018.

[98] T.-H. Vu and S. Kim, "Performance evaluation of power beacon-assisted wireless powered NOMA IoT-based systems," *IEEE Internet Things J.*, vol. 8, no. 14, pp. 11655–11665, Jul. 2021.

[99] T. H. Vu, T. V. Nguyen, D. B. da Costa, and S. Kim, "Performance analysis and deep learning design of underlay cognitive NOMA-based CDRT networks with imperfect SIC and co-channel interference," *IEEE Trans. Commun.*,vol. 69, no. 12, pp. 8159-8174, Dec. 2021.

[100] S. Solanki, P. K. Upadhyay, D. B. da Costa, P. S. Bithas, and A. G. Kanatas, "Performance analysis of cognitive relay networks with RF hardware impairments and CEEs in the presence of primary users' interference," *IEEE Trans. Cogn. Commun. Netw.*, vol. 4, no. 2, pp. 406-421, Jun. 2018.

[101] M. K. Simon and M.-S. Alouini, *Digital Communication over Fading Channels: A Unified Approach to Performance Analysis*, New York: Wiley, 2000.

[102] L. Liu, R. Zhang, and K. C. Chua, "Wireless information and power transfer: A dynamic power splitting approach," *IEEE Trans. Commun.*, vol. 61, no. 9, pp. 3990–4001, Sep. 2013.

[103] M. Abramowitz and I. A. Stegun, *Handbook of Mathematical Functions with Formulas, Graphs, and Mathematical Tables*, New York, 1972.

[104] D. Wan, M. Wen, F. Ji, Y. Liu, and Y. Huang, "Cooperative NOMA systems with partial channel state information over Nakagami- m fading channels," *IEEE Trans. Commun.*, vol. 66, no. 3, pp. 947-958, Mar. 2018.

List of Publications

A. Publications from PhD Thesis Work

A1. In Refereed Journals

1. **A. K. Shukla**, P. K. Upadhyay, A. Srivastava, and J. M. Moualeu,"Enabling co-existence of cognitive sensor nodes with energy harvesting in body area networks," ***IEEE Sensors Journal***, vol. 21, no. 9, pp. 11213-11223, May 2021, doi: 10.1109/JSEN.2021.3062368.

2. **A. K. Shukla**, V. Singh, P. K. Upadhyay, Abhinav Kumar, and J. M. Moualeu, "Performance analysis of energy harvesting-assisted overlay cognitive NOMA systems with incremental relaying," ***IEEE Open Journal of Communication Society***, vol. 2, pp. 1558-1576, 2021, doi: 10.1109/OJ-COMS.2021.3093671.

3. **A. K. Shukla**, J. Sharanya, K. Yadav and P. K. Upadhyay, "Exploiting SWIPT enabled IoT-based cognitive non-orthogonal multiple access with coordinated direct and relay transmission," ***IEEE Sensors Journal***, vol. 22, no. 19, pp. 18988-18999, Oct. 2022.

4. **A. K. Shukla**, K. Yadav, P. K. Upadhyay, and J. M. Moualeu,"Exploiting deep learning in the performance evaluation of EH-based coordinated direct and relay transmission system with cognitive NOMA", ***IEEE Communications Letters***, Mar. 2023, doi:10.1109/LCOMM.2023.325866 **Impact factor- 3.553**.

A2. In Refereed Conference Proceedings

1. **A. K. Shukla**, P. K. Upadhyay, A. Srivastava, and J. M. Moualeu,"Energy harvesting-assisted cognitive sensor nodes in wireless body area networks," in ***2021 IEEE 7th World Forum on Internet of Things (WF-IoT)***, Jul. 2021, New Orleans, LA, USA, pp. 488-493, doi: 10.1109/WF-IoT51360.2021.9595931.

B. Other Publications During PhD

B1. In Refereed Journals

1. **A. K. Shukla**, J. M. Moualeu, P. K. Upadhyay, and F. Takawira, "On the performance of cache- and energy harvesting–assisted NOMA in D2D communications with hardware impairments", communicated to ***IEEE Wireless Communications Letters***, Mar. 2023, **Impact factor- 5.281**.